UNIVERSITÀ DEGLI STUDI DI PADOVA

Dipartimento di Fisica e Astronomia "Galileo Galilei"

Master Degree in Physics

Final Dissertation

Study of Silicon Pixel detectors for the ALICE tracker upgrade

Thesis supervisor

Dr. Serena Mattiazzo

Candidate

Alessandra Zingaretti

Academic Year 2022/2023

Abstract

For vertex and tracker detectors, most High Energy Physics (HEP) experiments exploit hybrid pixel sensors, which are well known for their good energy, time, and spatial resolutions, together with the ability to cover a wide range of radiation and high fluxes. The *A Large Ion Collider Experiment* (ALICE) is the only experiment at the Large Hadron Collider (LHC) that has chosen to use instead Monolithic Active Pixel Sensors (MAPS) for the Inner Tracking System (ITS2).

In hybrid pixel sensors the sensing part and the readout electronics are placed on two different silicon pieces bump-bonded together; in MAPS the sensitive volume and the readout circuitry are both in one piece of silicon. This leads to an important reduction of the material budget, of the power consumption, as well as of the production costs.

For future upgrades, the ALICE collaboration will push forward the development of MAPS improving radiation hardness and high rate capabilities, increasing depletion depth, and further reducing power consumption and material budget. In particular, for the ITS3 upgrade, it is foreseen to replace the three innermost layers of the ITS2 with a first truly cylindrical tracker (ITS3) made of bent, wafer-scale, depleted monolithic pixel sensors based on 65 nm CMOS technology.

Many different small pixel matrix prototypes have already been designed and produced by the ALICE collaboration; many research centres are contributing to this R&D activity, which aim to characterise different versions of the sensors - i.e. pixels with different pitches and thicknesses, distinct process modifications etc. - at test beams at accelerator facilities or using table-top setups. As a result of all these efforts, unprecedented performances in terms of readout speed, material budget, signal-to-noise ratio and spatial resolution have been already reached.

In this thesis, Analogue Pixel Test Structures (APTS), designed for the ITS3 project and exposed to different radiation levels, are studied as the most important characteristics of the sensors - namely charge collection efficiency, speed, noise, etc. - are expected to be degraded with irradiation. This represents an important issue: for future high luminosity runs at colliders the requirements are not only good time and spatial resolution, but also high radiation hardness.

Contents

Executive Summary

The focus of my thesis work was the study of Monolithic Active Pixel sensors (MAPS) exposed to neutrons at the JSI TRIGA neutron irradiation facility. The goal was to verify the capability of these types of silicon sensors to tolerate Displacement Damage (DD) into the silicon lattice.

DD is characterized by the non-ionizing energy loss (NIEL), i.e. the portion of energy lost by a traversing particle which does not go into ionization and instead leads to displacement of lattice atoms. The defects generated by displacement damage are characterized by two types: point defects and cluster defects. The minimum energy to dislocate one Si atom and create a point defect is 25 eV. The recoil silicon atom, the Primary Knock-on Atom (PKA), becomes an interstitial and leaves behind a vacancy: the two are commonly referred to as a Frenkel pair. When sufficient energy is transferred to the PKA, it can generate a cluster: a localized region of damage with many dislocations (displacements) and vacancies.

DD will negatively affect the performance of any sensor. The main effects are: reduction of recombination lifetime and diffusion length, increase of majority and minority carrier trapping (which affects the charge collection efficiency); changes of majority-carrier concentration (due to carrier removal), and increase of thermal generation of electron-hole pairs under the effect of a sufficiently high electric field, which leads to an increase of the dark current [1].

The test structures which I studied were designed for the Inner Tracking System 3 (ITS3) project for the ALICE experiment at the Large Hadron Collider (LHC). At such High Energy Physics (HEP) experiments, the most important characteristics of sensors - namely charge collection efficiency, speed, noise, etc. - are expected to degrade in the hostile radiation environment. This is an important issue, especially for future high luminosity runs at colliders that require not only good time and spatial resolution, but also high radiation hardness. At the present moment, ALICE is the only experiment at the LHC that has chosen to use Monolithic Active Pixel Sensors (MAPS) for the Inner Tracking System (ITS2). However for the next upgrades at LHC, all the experiments will employ MAPS for their Inner Trackers [2, 3].

At present, for vertex and tracker detectors, most of HEP experiments exploit hybrid pixel sensors where the sensing part and the readout electronics - manufactured using standard CMOS process - are placed on two different silicon pieces: the active part and the electronics are connected using the flip chip bump-bonding techniques [4]. Hybrid pixel detectors are ideal to work in very hostile environments close to the interaction region of particle accelerators: they provide good spatial resolution ($\sim 15 \mu$m for 50μm pixel pitch [5]) and time resolution (~ 150ps [6]) for the measurement of short living particles, and are radiation hard (up to 2×10^{16} n_{eq}/cm^2). However, hybrid pixel sensors have several disadvantages. In fact, the assembly is a complex and expensive process for large area detectors; the pixel dimensions easily achieved are still too large; the power consumption is high and this requires an adequate cooling system, causing high material budget (for ATLAS and CMS it is of the order of 3% X_0), which worsens the vertex and momentum measurement.

On the contrary, in MAPS the sensitive volume and the readout circuitry are both in the same piece of silicon. This leads to an important reduction of the material budget, of the power consumption, as well as of the production costs. To enhance the performance of the detector, the Active Sensor Volume (ASV) of the device should be fully depleted to collect charge by drift and not by diffusion: this improves radiation hardness and features a fast time response. In addition, n-type and p-type

transistors are necessary in the pixel area to develop efficient processing blocks, required to increase the spatial resolution in vertexing and tracking [7].

The ALICE collaboration is pushing forward the development of MAPS improving radiation hardness and high rate capabilities, increasing depletion depth, and further reducing power consumption and material budget. In particular, for the ITS3 upgrade, it is foreseen to replace the three innermost layers of the ITS2 with a first truly cylindrical tracker (ITS3) made of bent, wafer-scale, depleted monolithic pixel sensors based on 65 nm CMOS technology.

Many different small pixel matrix prototypes have already been designed and produced by the ALICE collaboration with the MLR-1 (multi-reticle-layer run 1) submission. The Analogue Pixel Test Structure (APTS), a 4×4 pixel array, with parallel analogue readout for the whole matrix, comes in 4 variants of pixel pitches (10, 15, 20, 25 μm), two output buffer versions (source follower SF and OPAMP), three design variations (standard, modified, and modified with gap) [8].

For my thesis, I tested several APTS-SF. One chip with 15 μm pixel pitch (not irradiated) and other chips with 10 μm pixel pitch exposed to different irradiation levels: 1×10^{14} n_{eq}/cm^2, 1×10^{15} n_{eq}/cm^2, 2×10^{15} n_{eq}/cm^2 and 5×10^{15} n_{eq}/cm^2, values that are from one to two orders of magnitude higher than the expected fluences for the ITS3 upgrade, but in view of the future HL-LHC upgrade. During the irradiation process, due to the gamma background, the chips were exposed to a TID of approximately 1 kGy at 10^{14} n_{eq}/cm^2, linearly scaling with fluence, which is lower than the radiation load for the ITS3 of 10kGy.

To test irradiated sensors, the temperature needs to be below room temperature in order to reduce the leakage current. For this reason a chiller was used to keep the temperature at 14°C inside a cold box, where the chip carrier board is placed during the tests, together with two more boards: the proximity and the DAQ ones. The DAQ controls input parameters - current and voltage values that pass through the proximity - that bring the sensor to the working point, and manages the data measured by the sensor - after it passed through the proximity board - and allows data transfer to a computer via a USB cable. The proximity transfers the power supply to the chip, converts the analogue values measured by the chip to digital signals and passes them to the DAQ board.

The characterisation process consists of the following steps, repeated for different reverse bias voltages V_{bb} (0.0 V, -1.2 V, -2.4 V, -3.6 V and -4.8 V):

- *test pulse*: to check if all the pixels are working;

- *threshold scan*: to choose a proper acquisition threshold in order to select signals above the noise level;

- *gain*: to check baseline and working point conditions;

- *source measurement*: to acquire data with a source (^{55}Fe and ^{90}Sr);

- *leakage current measurement*: to measure the leakage current in each pixel.

The thesis work is organised as follows. In Chapter 1, an overview of the ALICE experiment is given. Chapter 2 is dedicated to silicon pixel detectors, with particular attention to MAPS. In Chapter 3, radiation damage effects are discussed. Chapter 4 is devoted to the experimental setup. In Chapter 5, the measurement procedure is explained. In Chapter 6, the results from the data analysis are presented and discussed.

Chapter 1

The ALICE experiment

In this chapter, an overview of the ALICE experiment is given, together with some details about the ALICE detector, in particular the current Inner Tracking System and its future upgrades.

1.1 ALICE experiment overview

ALICE (A Large Ion Collider Experiment) is an experiment at the CERN LHC (Large Hadron Collider) focused on quantum chromodynamics (QCD), the theory behind strong interactions between quarks mediated by gluons. Its purpose is the study of strongly interacting matter and the quark-gluon plasma in nucleus-nucleus collisions at extreme values of temperature and energy density. The experiment includes heavy nuclei collisions (Pb-Pb), but also collisions with lighter ions and at lower energy - to vary the interaction volume and the energy density - and proton-nucleus runs. The ALICE heavy-ion detector, described below in Section 1.2, is used to study these collisions. [9]

The main goal of ultra-relativistic heavy-ion collisions is to study the properties of quark-gluon plasma (QGP), which is a state of matter expected to exist at high energy densities and at high temperature by QCD. In this state of matter quarks and gluons are no longer confined in hadrons.
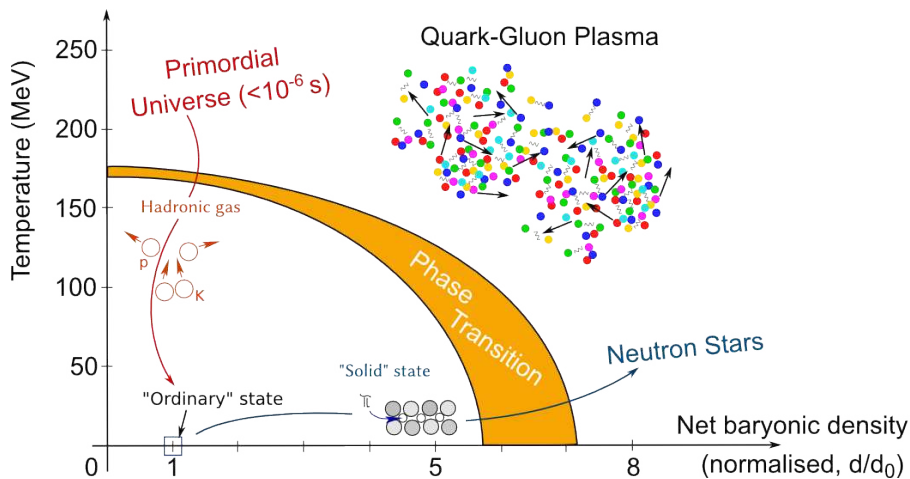
Figure 1.1: Phase diagram (temperature vs net baryon density) of QCD matter, ranging from normal quark-confined nuclear matter to unconfined QGP.

The transition between confined matter and the QGP happens when the temperature reaches the critical value estimated to be $\sim 2 \times 10^{12}$ K ($\sim$160 MeV) [1]. It is believed that around a few millionths of a second after the Big Bang the temperature in the Universe was above this critical value, and everything was in a quark-gluon plasma state.

---

[1]The Boltzmann constant is $k_B = 8.6173... \times 10^{-5}$eV K^{-1} so 1 eV corresponds to $\sim$1.1604$\times 10^4$ K

The ALICE collaboration studies how quark-gluon plasma affects different bound states of a charm quark and its antimatter counterpart, also produced in Pb-Pb collisions. One method used to observe QGP properties consists in studying in-medium behaviour of heavy quark bound states (i.e. charmonium).

Charmonia (or hidden-charm particles) are bound states of a charm quark and a charm antiquark; they are held together by the strong interaction and are exceptional probes of QGP. In the plasma state, their production is suppressed due to the presence of a large number of quarks and gluons. This suppression increases with the temperature of the plasma and is predicted to affect different charmonia to varying degrees. For instance, the production of the state $\psi(2S)$ - which is ten times more weakly bound and 20% more massive than the state J/ψ - is expected to be more suppressed than the production of the state J/ψ [2].
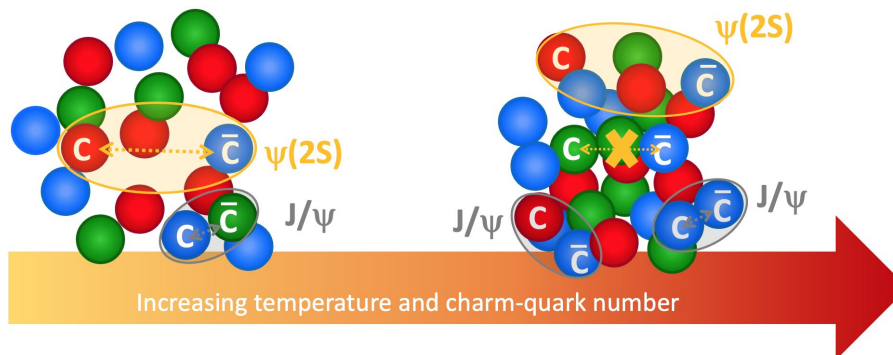

Figure 1.2: Illustration of the effect of QGP on the formation of charmonia in lead-nuclei collisions. As the plasma temperature increases, the $\psi(2S)$ (weakly bound) is more likely to be "screened" and therefore not form, because of the larger number of quarks and gluons in the plasma. The formation of additional $c\bar{c}$ mesons is enhanced by the increase in the number of charm quarks and antiquarks.

The abundance of charm quarks and antiquarks in the QGP gives rise to a recombination mechanism that forms new charmonia states and counters the suppression mentioned before. The whole process should depend on the momentum and the type of the charmonia: more weakly bound states are expected to be produced through recombination later in the evolution of the plasma, and charmonia with lowest transverse momentum p_T are expected to have the highest recombination rate.

Interesting results have been obtained in previous runs already: the $\psi(2S)$ suppression is seen to be reduced towards lower momentum, meaning that the recombination process is taking place.

Future ALICE upgrades might lead to an ultimate understanding of the modification of hidden-charm particles and of the strong interaction that holds them together in the extreme environment of the QGP [10, 11].

1.2 Detector layout

The ALICE detector setup is composed of a central barrel, which detects photons, electrons and hadrons, a forward muon spectrometer, and other detectors for different purposes. The central part - placed in a large solenoid magnet - covers polar angles from 45° to 135°.

In the following sections, all the detectors grouped by a specific function are briefly presented (for further information see [9]).

---

[2] J/ψ and $\psi(2S)$ are both $c\bar{c}$ mesons, they have different characteristics which can be found here:
https://pdglive.lbl.gov/Particle.action?init=0&node=M070&home=MXXX025
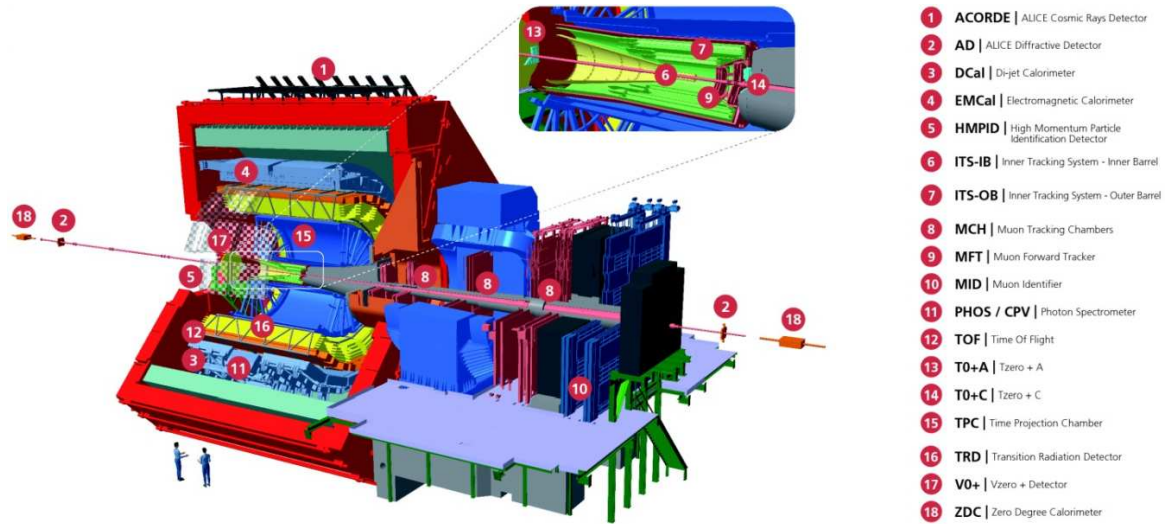https://pdglive.lbl.gov/DataBlock.action?node=M071W&home=MXXX025

Figure 1.3: Schematic layout of the ALICE detector as during RUN3 (after upgrade).

Tracking detectors

- Inner Tracking System (ITS) for the reconstruction of primary and secondary vertices, tracking and identification of charged particles with a low p_T cutoff and improvement of the momentum resolution at high p_T;

- Time Projection Chamber (TPC) for tracking and identification of charged particles.

Particle identification

- Transition Radiation Detector (TRD) for the identification of electrons among other charged particles;

- Time Of Flight (TOF) for the identification of charged particles in the intermediate momentum range;

- High Momentum Particle Identification Detector (HMPID) for the identification of charged particles having large momentum.

Electromagnetic calorimeters

- ElectroMagnetic Calorimeter (EMCal) to measure highly energetic photons, electrons, neutral pions, and jets of particles;

- Di-jet Calorimeter (DCal) for the measurements of back-to-back jets, which originate in the interactions of ultra-high-energy quarks and gluons;

- PHOton Spectrometer (PHOS) to measure the photons coming out of the extremely hot plasma created in the lead-lead collisions at the LHC;

Muon tracker and spectrometer

- Muon Spectrometer (MS) for the detection of heavy quark resonances (such as J/ψ) via their decay to $\mu^+\mu^-$, which provides an essential tool to study the early and hot stage of heavy-ion collisions;

- Muon Forward Tracker (MFT) to enhance the vertexing capability of the ALICE Muon Spectrometer.

Forward and trigger detectors

- Zero Degree Calorimeter (ZDC) to measure the forward energy carried by the noninteracting nucleons;

- Fast Interaction Trigger (FIT) to measure the primary forward trigger, luminosity, and collision time, and to determine multiplicity, centrality, and reaction plane of heavy ion collisions.

1.3 The Inner Tracking System (ITS)

The Inner Tracking System (ITS) is the central most detector surrounding the beampipe located in the central barrel of ALICE.

The main tasks of the ITS are to localise primary and secondary vertices necessary for decay reconstructions, to track and identify low-momentum particles, and to improve the momentum and angle resolution for particles reconstructed by the TPC.

The ITS was initially designed for rates up to 100 particles/cm^2 for Pb-Pb collisions for center of mass energy $\sqrt{s_{NN}} = 5.5$ TeV.

The ITS for LHC Run 1 and Run 2 consisted of six cylindrical layers built using three different technologies: Silicon Pixel Detectors (SPD) for the two innermost layers, Silicon Drift Detectors (SDD) for the following two layers, and double-sided Silicon micro-Strip Detectors (SSD) for the two outer layers [12]. The outer radius was determined by the necessity to match tracks with those from the TPC (430 mm), and the inner radius was the minimum allowed by the radius of the beam pipe (39 mm) [9]. The four outer layers had analogue read-out and therefore were used for particle identification (PID) via dE/dx measurement in the non-relativistic region (dE/dx $\propto 1/\beta^2$). All detector elements were carefully designed to minimise their radiation length, achieving 1.1% X$_0$ per layer.

The precision of the first version of the ITS in the determination of the track distance of closest approach was adequate to study only certain decay channels at value of transverse momentum above 1 GeV/c, but at lower p_T values it was inefficient. Another limitation was given by the limited read-out rate capabilities [13]. These motivations lead to the ITS2 upgrade, which is the current tracker (see subsection 1.3.1).

1.3.1 ITS2

The upgraded Inner Tracking System 2 (ITS2) was installed during the Long Shutdown 2 of the LHC during 2019–2021. It consists of seven cylindrical layers of silicon pixel sensor chips, situated directly around the Interaction Point (IP) and beam pipe. The key features of the ITS upgrade can be summarised as follows.

- **First detection layer closer to the beam line:** the diameter of the beampipe has been reduced (from 6 cm to 3.8 cm) which improved the measurement of the impact parameter by a factor of 3 and 5 in the rϕ and z coordinate, respectively, at a p_T of 500 MeV/c [14].

- **Reduction of material budget:** the overall material budget has been reduced to 0.35% X$_0$ (compared to 1.14% X$_0$ of its predecessor). In particular, the use of Monolithic Active Pixel Sensors (MAPS) allowed the silicon material budget per layer to be reduced by a factor of seven in comparison to the old ITS (50 μm instead of 350 μm). Moreover, the pixel size has been noticeably reduced from 50μm $\times$ 425μm to 29.24μm $\times$ 26.88μm.

- **Geometry:** seven concentric cylindrical layers covering a radial extension from 23 mm to 400 mm with respect to the beamline.

- **Read-out rate:** increased from 1 kHz up to 100 kHz in Pb–Pb and 200 kHz in pp collisions [14].
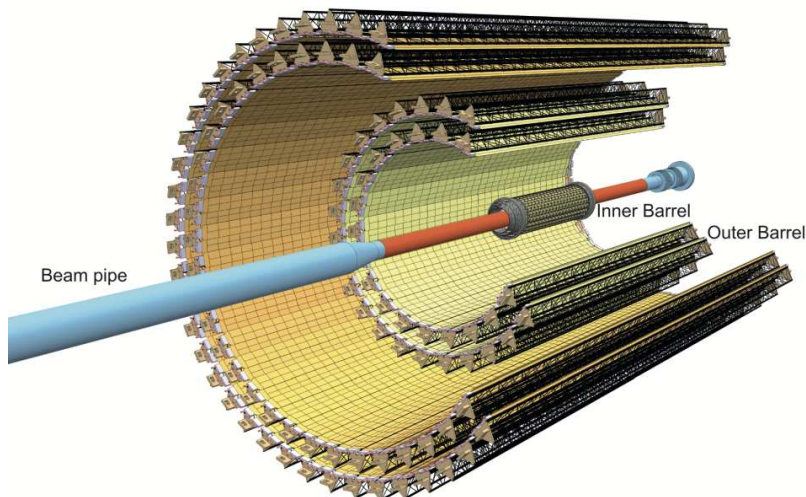
Figure 1.4: Schematic layout of the ITS2.

The key component of the ITS2 is a novel pixel sensor chip, the ALPIDE, which was developed at CERN specifically for the ALICE ITS upgrade. The seven layers of the ITS2 are assembled from sub-assemblies of sensor chips referred to as staves, and the entire detector consists of 24 120 chips (192 staves) in total. The layout of the detector is depicted in Figure 1.4.

The ALPIDE chip is a Monolithic Active Pixel Sensor (MAPS) fabricated in the TowerJazz 180 nm CMOS Imaging Process. It has a pixel matrix of 1024×512 pixels which covers a total area of 29.94 mm $\times$ 13.76 mm. The size of an individual pixel is 29.24 μm $\times$ 26.88 μm; each pixel includes a charge collection diode, an amplification chain, a discriminator and multiple-event buffer. As can be seen in Figure 1.5 a deep p-well makes it possible to employ complex logic inside the pixel matrix, without having the n-well PMOS transistors compete with the collection electrodes.
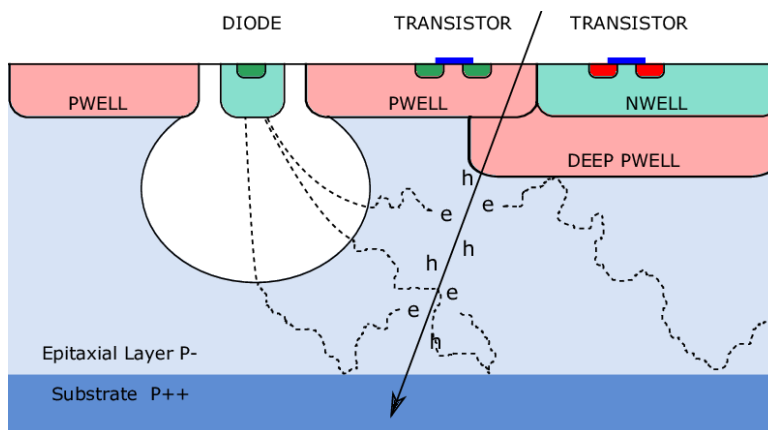

Figure 1.5: Main parts of a monolithic active pixel sensor in a section view of one pixel [13].

1.3.2 ITS3

ALICE is currently planning to install a new vertex detector (ITS3) during the LHC Long Shutdown 3 (LS3) to replace the three inner layers of the current ITS2. The proposal for the novel vertex detector consists of curved wafer-scale ultra-thin silicon sensors arranged in cylindrical layers (see Figure 1.6), with an extraordinary low material budget of 0.05% X_0 per layer; the innermost layer is placed at only 18 mm radial distance from the interaction point.

Achieving such a challenging objective on the material budget, essentially requires having in the active area only the thin MAPS silicon sensor (<50 μm), while removing mechanical structures, cooling lines and any printed circuits for the interconnection of adjacent sensors.

ALICE has demonstrated that the ALPIDE thin silicon chips are flexible enough to be bent onto truly cylindrical surfaces of radii well below 18mm. Their performance was validated and compared to unbent sensors.

In parallel, ALICE chip designers are dealing with stitching technology [3] to overlap sensors' images on a large silicon wafer, such to cover the surface of an entire ITS half layer (280 mm × 93 mm); this removes the need of printed circuit boards for interconnection in the active area, with signals and power feeding the sensors only at its edge.

These developments show the feasibility of a large silicon layer, bent to cylindrical shape, that will not only reduce the achievable distance from the beam pipe (no staggering of staves will be needed), but that will also give the layers an intrinsic stability, minimizing the requirement on supporting structures.

In the new detector, each half-cylinder will consist of curved wafer-scale MAPS, with bending radii of 18, 24 and 30 mm; the length of the sensor will be 27 cm along the beam direction. Carbon foam, with large radiation length, has been identified as the design choice for the mechanics of the new vertex detector to achieve the requirement on minimum material budget.

The single hit position resolution required is of the order of 5 μm: for this reason a pixel pitch of the order of 20 μm is demanded [4].
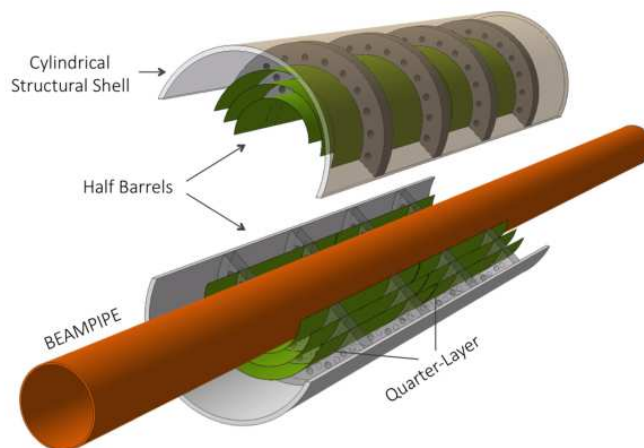

Figure 1.6: Layout of the ITS3 Inner Barrel. The figure shows the beam pipe and the two half-barrels mounted around it.

The current ALPIDE chip dissipation is close to 40 mW/cm^2. The change of technology node from 180 nm node to 65 nm (together with the related voltage scaling) is expected to bring a reduction of power by at least a factor 2 for similar sensor features [16]. With such a reduced power consumption, low speed air flow can be therefore adopted as cooling solution, thus removing liquid cooling and pipes from the active area. The carbon foam used as sensor support will also act as a radiator for the air cooling.

---

[3]The stitching technique [15] allows to manufacture devices much larger than the dimensions of the design reticle (normally with area 3 cm × 2 cm). The design reticle gets subdivided in sub-frames that correspond to sub-frames of the photomasks. During the photolithographic patterning of wafers, these are exposed onto neighbouring locations according to a pre-established pattern. This requires very precise alignment and translation of the wafers between each exposure. [16]

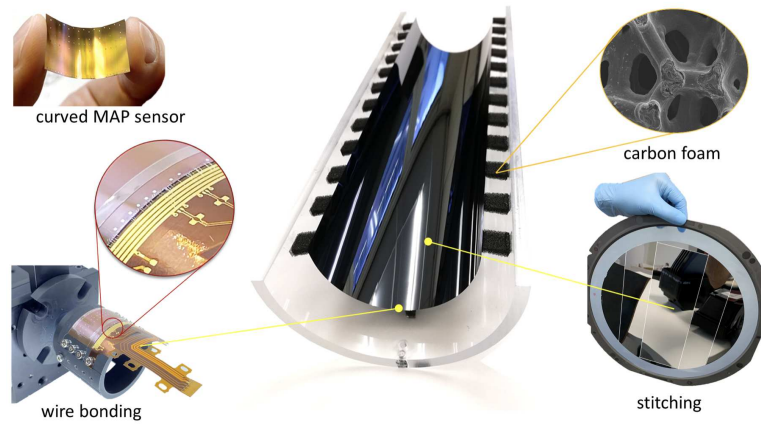[4]It is often assumed that the binary resolution is pitch/$\sqrt{12}$, which is generally a worst case upper limit [17].

Figure 1.7: 50 μm thin silicon sensor, 280 mm in length, bent to 30 mm radius. Large area MAPS obtained using stitching technique. Electrical connectivity at one edge of the sensor by wire bonding. Carbon foam provides mechanical and thermal functions.

With this kind of modifications, a large reduction of material budget and a large improvement of the efficiency at low p_T and of the tracking precision are predicted. [18]

Chapter 2

Silicon pixel detectors

This chapter aims to provide basic information about the working principle of silicon detectors, the state of the art of silicon pixel sensors and an insight on Monolithic Active Pixel Sensors (MAPS) which are exploited for the ITS of the ALICE experiment.

2.1 Interaction of Radiation in Detectors

2.1.1 Introduction

The interaction of high energy particles with a silicon pixel detector can produce three types of effects:

- Transient ionisation effects are due to the production of electron-hole pairs, the signal charge, by the passage of an ionising particle.

- Long-term ionisation effects. Insulator materials (always present in a pixel detector) do not return to their original state but retain relatively immobilised charge. The electrical properties of the device can be affected when charges are trapped in insulation layers.

- Long-term displacement effects. These effects arise because of the displacements of atoms from their normal sites in a crystal lattice, producing a less ordered structure and relatively long-lived changes of some properties of the semiconductor material, that affect the device behaviour.

The transient production of electron-hole pairs is the fundamental phenomenon, at the very basis of how a particle detector works, as discussed in this Chapter. Long term ionisation and displacement effects lead instead to the degradation of detector performances in radiation environments, such as loss of signal charge and increased noise, and will be discussed in Chapter 3.

The evaluation of the degradation of the detectors studied in this thesis was carried out using two radioactive sources:

- ^{55}Fe, a source of X-ray photons used for calibration purposes;

- ^{90}Sr, a source of electrons that mimic minimum ionising particles.

In the following, a few words to describe the pertinent interactions of charged particles, in particular electrons, and photons with matter are given.

2.1.2 Charged particles in matter

A fast charged particle moving through matter undergoes many inelastic collisions with atomic electrons (coulomb interaction) exciting or ionising them; by losing energy, the particle slows down. The
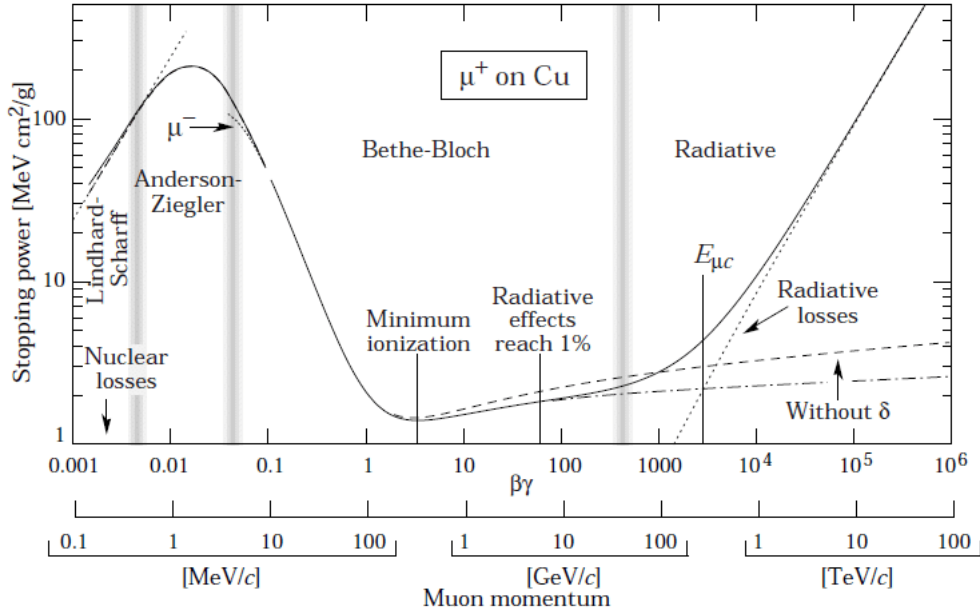
Figure 2.1: Mean energy loss of a μ^+ in copper.

stopping power of the material, $-dE/dx$, is the rate of energy loss in thickness due to ionization. A charged particle will also interact with atomic nuclei via the Coulomb interaction. Each interaction will change the direction of motion of the particle and this will result in an angular spreading of the beam of particles.

The following Bethe-Bloch formula provides an analytical description of the stopping power of swift heavy charged particles (muons, protons, α particles, atomic ions, but not of the light electrons):

$$-\frac{dE}{dx} = 4\pi N_A r_e^2 m_e c^2 z^2 \rho \frac{Z}{A} \frac{1}{\beta^2} \left[\ln \left(\frac{2m_e c^2 \gamma^2 \beta^2}{I} \right) - \beta^2 - \frac{\delta}{2} \right], \qquad (2.1)$$

where:

- N_A, r_e and m_e are Avogadro's number, electron classical radius[1] and electron mass respectively;

- z is the electric charge of the incident particle;

- ρ, Z and A are the density, atomic number and atomic mass of the material;

- β is the particle velocity in units of c and $\gamma = \frac{1}{\sqrt{1-\beta^2}}$;

- I is the absorber mean excitation energy;

- δ describes the electric field reduction due to medium polarisation.

At $\beta\gamma \approx 4$ there is the so called minimum ionising condition (MIP), at which the particle energy loss is almost constant. A representation of the trend of the Bethe-Bloch formula is given in Fig. 2.1. The total path length traversed by a charged particle before it loses all its energy and stops is called its *range*.

---

[1]$r_e = \frac{1}{4\pi\varepsilon_0} \frac{e^2}{m_e c^2} = 2.817\ 940\ 3227(19)$ fm
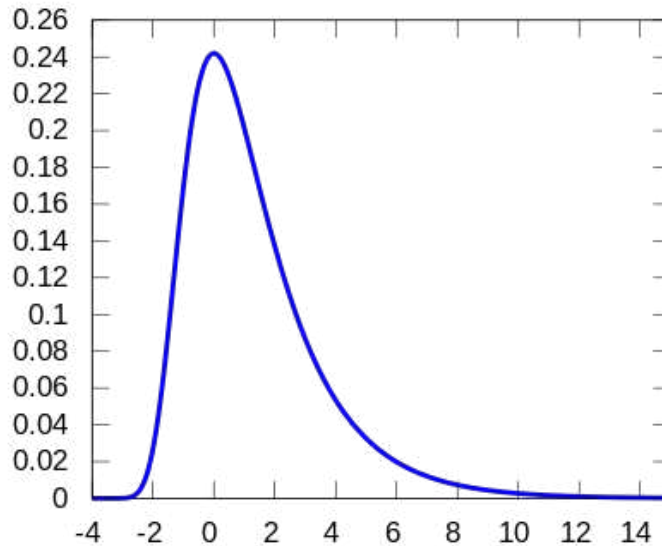
Figure 2.2: Landau distribution for MPV $= 0$ and $\sigma = 1$

For electrons the energy loss is slightly different, as it is more sensitive to relativistic corrections due to their small mass and quantum effects due to them being indistinguishable from the atomic electrons with which they interact. The Bethe-Bloch formula for electrons is:

$$-\frac{dE}{dx} = 4\pi r_0^2 \frac{m_e c^2}{\beta^2} NZ \left[\ln\left(\frac{\beta\gamma\sqrt{\gamma-1}mc^2}{I} \right) + \frac{1}{2\gamma^2}\left(\frac{(\gamma-1)^2}{8} + 1 - (2\gamma^2 + 2\gamma - 1)\ln2 \right) \right], \quad (2.2)$$

where N is the number of atoms/m^3. At high energies, way beyond those of the ^{90}Sr source used in this thesis, electrons can suffer much larger radiative losses (Bremsstrahlung), and further terms must be added to account for this.

The statistical nature of the collisions of a particle with the atoms of a medium is not only manifest in the angular spread of the passing beam, but also in both the spread of the total range and in the ionisation losses in a given layer of the medium. If the thickness Δx of a material is sufficiently large, a particle traversing it will experience a large number of collisions and the spread of the energy loss around the mean value $\langle\Delta E\rangle$ will be distributed normally:

$$P(\Delta E, \sigma) = \frac{1}{\sqrt{2\pi}\sigma}\exp\left(-\frac{(\Delta E - \langle\Delta E\rangle)^2}{2\sigma^2} \right) \quad (2.3)$$

If, instead, the material is thin, i.e. Δx is small compared to the case considered above, the relatively small number of collisions experienced by the particle leads to a Landau distribution that is not symmetric, like the normal one for thick layers, but skewed with a high energy loss tail. The Landau energy loss distribution, shown in Eq. 2.4, is parametrized by two parameters: the Most Probable Value (MPV), which is the most probable value of energy loss, and a scale parameter σ, which is related to the width of the distribution [2].

$$p(\Delta E; MPV, \sigma) = \frac{1}{\pi\sigma} \int_0^\infty e^{-t}\cos\left[t\left(\frac{\Delta E - MPV}{\sigma} \right) + \frac{2t}{\pi}\log\left(\frac{t}{\sigma} \right) \right] dt \quad (2.4)$$

Fig. 2.2 shows the landau shape for MPV $= 0$ and $\sigma = 1$.

2.1.3   Photons in matter

The interaction of photons in matter is completely different from that of charged particles. The photon does not have an electric charge and hence it doesn't make the many inelastic collision with

---

[2]For the distribution described by Eq. 2.4, it is not possible to define a mean value, nor higher moments.
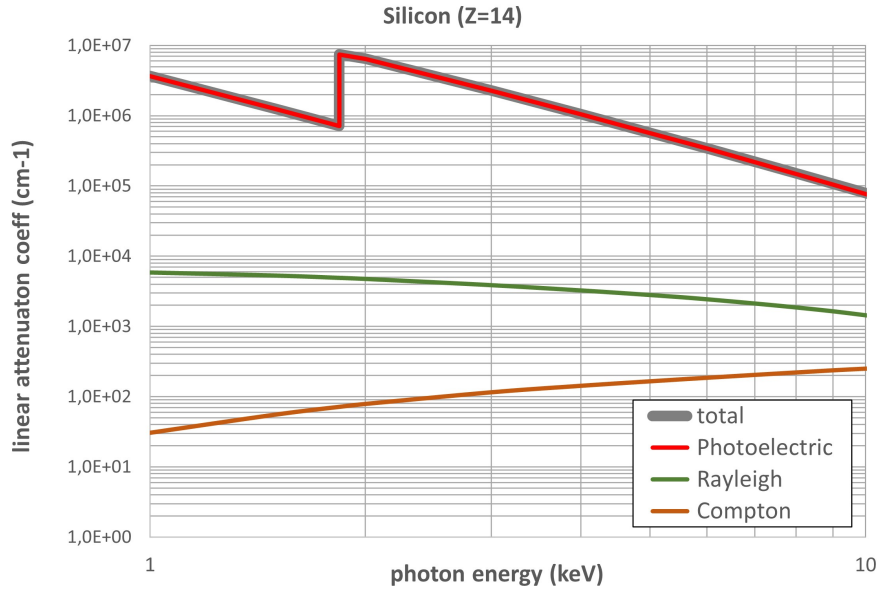
Figure 2.3: Photon linear attenuation coefficient in Silicon in the 1-10 keV energy range

atomic electrons so characteristic of charged particles. For photons the most important mechanisms of interaction are:

- Photoelectric effect

- Compton and Rayleigh scattering

- Pair production

As a consequence of such kinds of interactions, a photon that interacts with matter is completely removed from an incident beam: a beam of photons that interacts with a slab of matter is attenuated in intensity, not degraded in energy. The attenuation of the incident beam intensity is exponential with the thickness of the absorbing medium and can be expressed by the following relation:

$$I(x) = I_0 \cdot e^{-\mu \cdot x} \tag{2.5}$$

where x is the path travelled in the material and μ is the linear attenuation coefficient, usually expressed in cm^{-1}. It depends on three factors: the photon energy, the atomic number and the density of the material. It has contributions from each of the four interaction mechanisms:

$$\mu_{tot} = \mu_{rayleigh} + \mu_{compton} + \mu_{photoelectric} + \mu_{pairproduction} \tag{2.6}$$

The first two are scattering events, so at the end of the process a photon is emitted, while the last two are absorption events, so the incoming photon is destroyed and a single electron and an electron/positron pair are produced, respectively.

When using X-rays sources to test the response of silicon detectors, only two of these need to be considered: the dominant photoelectric effect and the Compton scattering. Figure 2.3 shows the linear absorption coefficient in silicon in the pertinent 1-10 keV energy range [3].

In the photoelectric effect the incident photon is completely absorbed and an electron is ejected from the atom. Compton scattering involves the electromagnetic transfer of momentum and energy to an atomic electron. It is a purely quantum effect, described as a relativistic elastic collision of a photon

---

[3]Mass attenuation values from the NIST (National Institute of Standard and Technology) are multiplied by the silicon density (2.33 g·cm^{-3}) to obtain the linear attenuation coefficient expressed in cm^{-1}, https://physics.nist.gov/PhysRefData/Xcom/html/xcom1.html

with an electron. It results in a scattered photon, with an energy lower than the initial incoming one, and the ejection of the electron from the atom.

The pair production process and the Rayleigh process are mentioned only for completeness. Pair production requires a minimum energy of $2m_e c^2 = 1.02$ MeV, which is much higher than the energy of the X-rays from the ^{55}Fe source used. In classical terms, the Rayleigh process can be understood as an electromagnetic plane wave transferring energy to an atomic cloud, which starts to oscillate and hence emit dipole radiation with the same frequency. The Rayleigh scattering process is a non-ionising process: it does remove photons from the beam, but there is no ejection of electrons from the atom and hence leaves no signal in a detector.

2.2 Silicon detector working principle

To better understand the working principle of a silicon pixel detector, it is useful to revise the p-n junction (see Figure 2.4). Consider a piece of silicon with an n-doped and a p-doped part[4]. The doping level must be high enough to overcome the intrinsic carrier densities (in silicon, at room temperature, this value is $\sim 10^{-10}$ cm^{-3}) so that an abundance of majority carriers is formed (electron in the n-zone, hole in the p-zone). The interface between n-doped and p-doped regions will be emptied of free charges because the majority carriers in each region diffuse through the junction and recombine with the opposite sign charge carriers. This process generates an electric field, caused by the excess charge of doping atoms at rest, which outweighs the diffusion and a "built-in potential difference" V_0 is established across the junction:

$$V_0 = V_T \ln \frac{N_D N_A}{n_i^2} \tag{2.7}$$

where

- V_T is the thermal voltage of 26 mV at room temperature;

- N_D and N_A are the impurity concentration of donors and acceptors, respectively;

- n_i is the intrinsic concentration.

Typically, at room temperature, the built-in potential for silicon is about $0.6 - 0.7$ V. This potential barrier will always exist, even if the device is not connected to any external power source.
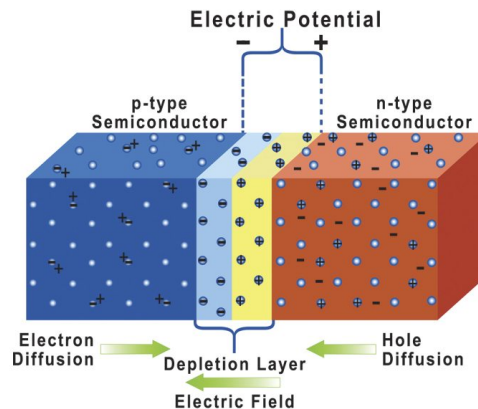

Figure 2.4: Isolated PN junction (not connected to a powered circuit) [19].

---

[4]Doped silicon is obtained through the introduction of impurities in the semiconductor crystal; p-doping is obtained using as dopants elements of the III group that have 3 valence electrons (such as boron), whereas n-doping is obtained using as dopants elements of the V group that have 5 valence electrons (such as phosphorus). In p-doped semiconductors, the charge carrier is the hole left in the silicon valence band, after the dopant combines with silicon; in n-doped semiconductors, the charge carrier is the free electron.
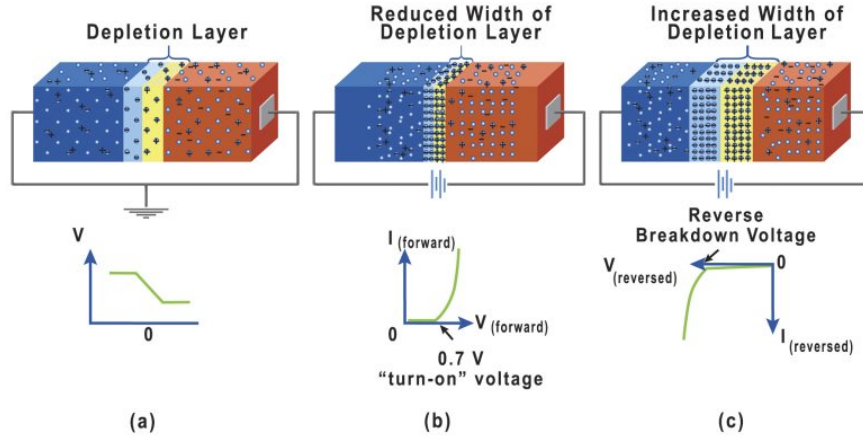
Figure 2.5: Current flow characteristics of a PN junction diode: (a) zero bias applied, therefore no current flows; (b) forward biased junction, the external voltage is oriented in the opposite direction of the electric field due to the depletion region, therefore the depletion region shrinks; (c) reverse biased junction, the depletion region gets wider, producing a high resistance to current flow in the diode [19].

A state of equilibrium is therefore established (electrically neutral situation). This regions on either sides of the junction, now completely depleted of free carriers, is called *depletion zone* and extends for a total thickness W which can be expressed as follows:

$$W = x_P + x_N = \sqrt{\frac{2\epsilon_0 \epsilon_{Si}}{e} \left(\frac{N_A + N_D}{N_A N_D} \right) V_0} \tag{2.8}$$

where x_P and x_N are depletion region extensions in the P type and N type silicon respectively, ϵ_{Si} = 11.7 (at 300K) is the dielectric constant of silicon relative to the vacuum one ϵ_0, V_0 is the built-in voltage, e is the electric charge, N_A and N_D are the dopant densities[5]. If a suitable positive voltage (forward bias)[6] is applied between the two ends of the PN junction, it can supply free electrons and holes with the extra energy they require to cross the junction, as the width of the depletion layer around the PN junction is decreased. By applying a negative voltage (reverse bias)[7], the free charges are pulled away from the junction, thus resulting in the depletion layer width being increased. This has the effect of increasing or decreasing the effective resistance of the junction itself, allowing or blocking the flow of current through the PN junction.

PN junctions are usually highly asymmetrical in doping concentration (either $N_D \ll N_A$ or $N_A \ll N_D$). A highly asymmetrical junction is called a one-sided junction (either an N^+P junction or a P^+N junction), where N^+ and P^+ denote the heavily doped sides. The depletion layer penetrates primarily into the lighter doping side, and the width of the depletion layer in the heavily doped material can often be neglected. For a reverse biased asymmetric junction the depletion width W has the following expression:

$$W \approx x_P \approx \sqrt{\frac{2\epsilon_0 \epsilon_{Si}}{e} \left(\frac{V_0 - V}{N} \right)} = \sqrt{2\epsilon_0 \epsilon_{Si}(V_0 - V)\mu\rho} \tag{2.9}$$

where V is the reverse bias applied by an external source, N is the lighter doping concentration, μ is the majority carrier mobility and ρ is the resistivity.

To maximise the depletion depth it is useful to choose the silicon resistivity and the carrier mobility as high as possible[8], as well as a high value of reverse bias.

---

[5]ϵ_0 = 8.854...×10^{-12} F/m, and e =1.602...× 10^{-12} coulomb

[6]Applying the positive voltage to the p-side and connecting the n-side to ground.

[7]Applying the positive voltage to the n-side and connecting the p-side to ground.

[8]The value of the electron mobility is $\mu_e \sim 1350$ cm^2/(V·s), whereas the value the hole mobility is $\mu_h \sim 450$ cm^2/(V·s): for this reason electrons are preferred to holes.

Considering that fixed charges build up on both sides of the junction, the depletion zone can be seen as a charged capacitor with value C per unit of area:

$$C = \epsilon_0 \epsilon_{Si}/W = \sqrt{e\epsilon_0\epsilon_{Si}(N/2V)} \qquad (2.10)$$

Taking into account all these considerations, it is easier to understand how silicon pixel detectors work. When ionizing particles cross the silicon detector, they generate charge carriers (electron-hole pairs). On average, every 3.6 eV of energy deposited one electron-hole (e^-/h^+) pair is generated. For example, when a relativistic particle crosses a 300 μm thick silicon detector, it looses energy in collision with the electrons of the crystal and generates ~ 80 e^-/h^+ pairs per micron of path. The generated charges drift under the action of the external electric field with a speed - that depends on the electric field - that saturates at values $\sim 10^7$ cm/s for fields near to 10^4 V/cm [9]. The collection time is about 10 ns, which means that the current is about 0.5 μA [20]. If the carriers are created in the depletion region, they might induce a current, which is instantaneously much larger than the thermal background current and thus can be detected. This means that the depletion region is the active volume of the detector, whereas the undepleted regions are not appropriate for the collection, because too many majority carriers facilitate charge recombination and the electric field is too low to collect charges in a short time [20].

If the reverse bias V is increased, the thickness W of the depletion region increases, while the capacitance decreases: this leads to an improvement of the signal over noise ratio (S/N). For this reason, fully depleted detectors[10] have the best S/N.

2.3 Hybrid Pixel Detectors

Nearly all vertex detectors in high energy physics experiments are made using *hybrid pixel* detectors, a type of sensors where the active part and the pixel readout chip - manufactured using standard CMOS process - are implemented on separate silicon pieces as can be see in Figure 2.6: the active part and the electronics are connected using the flip chip [11] bump-bonding technique [12] [4].
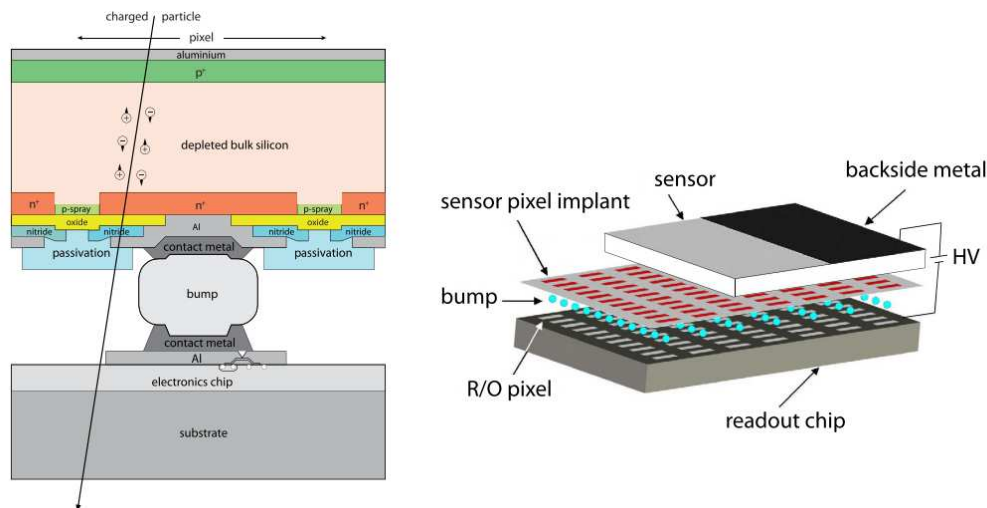

Figure 2.6: On the left, the schematic of signal production in the sensor, on the right the general architecture of a hybrid pixel detector [6].

---

[9]Suppose a silicon resistivity of 2.5 kΩcm for a 300 μm thick silicon detector, fully depleted at 200 V bias voltage [20]

[10]Detectors where the depletion zone extends to the whole thickness of the silicon layer.

[11]One of the two chips (sensor and readout chips) is flipped and then bonded to the other using solder bumps

[12]This method exploits a bump to connect the sensor and the readout chip (instead of a wire): the bump can be formed in many different ways (for more details, refer to [21]).

Hybrid pixel detectors are ideal to work in very hostile environments, i.e. close to the interaction region of particle accelerators. In fact, they provide good spatial resolution ($\sim$ 15 μm for 50 μm pixel pitch [5]) and time resolution ($\sim$ 150 ps [6]) for the measurement of short living particles. They are also radiation hard, meaning they survive high fluxes of particles. At the LHC luminosity of 10^{34} cm^{-2}s^{-1}, for instance, the expected fluence is 2×10^{15} n$_{eq}$/cm^2 per lifetime; for the next upgrade (High Luminosity LHC, HL-LHC) the luminosity is expected to increase by a factor 10 (10^{35} cm^{-2}s^{-1}), so that also the expected fluence will be one order of magnitude larger (2×10^{16} n$_{eq}$/cm^2 per lifetime).

However, hybrid pixel sensors have several disadvantages. In fact, the assembly is a complex and expensive process for large area detectors; the pixel dimensions easily achieved are still too large; the power consumption is high and this requires an adequate cooling system, causing high material budget (for ATLAS and CMS it is of the order of 3% X$_0$), which worsens the vertex and momentum measurement.

A valid alternative to hybrid pixel sensors is presented in the following section.

2.4 Monolithic Active Pixel Sensors

The Monolithic Active Pixel Sensors (MAPS) technology combines the sensitive volume and the front-end readout logic in the same silicon die, using standard CMOS processes. MAPS have shown many advantages with respect to hybrid pixel sensors, because the production process is less expensive, they can be built in large array sizes, their thickness can be reduced depending on the needs; each pixel has individual readout, they are quite radiation hard and their power consumption can be reduced noticeably. Moreover, the absence of external interconnection between the active volume and the readout circuit reduces the input capacitance, which leads to very low noise and high S/N ratio.

Efficiency and speed of MAPS depends on the substrate used in the CMOS process, i.e. how thick the Active Sensor Volume (ASV) can be and whether the sensor can be depleted. Older-generation MAPS were built using low-resistivity (about 10 Ωcm) epitaxial wafers: signals of the order of 1k e^- were collected by thermal diffusion in times of the order of 100 ns [22]. Another important limitation of this type of MAPS was the use of only one type of transistor in the pixel circuitry, since no deep well implantation was possible. In addition,they could survive only up to irradiation levels $\leq 10^{13}$ n$_{eq}$/cm^2, given the charge collection mechanism mainly by diffusion.
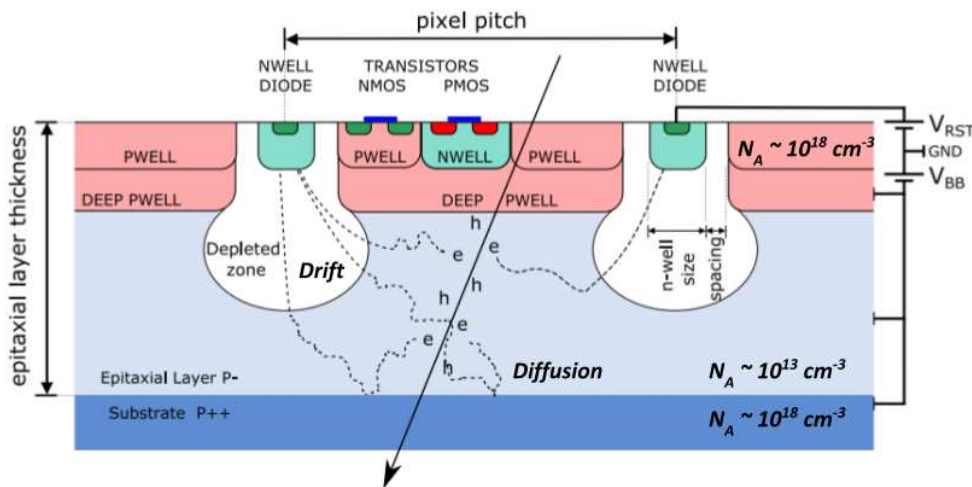

Figure 2.7: Scheme of the cross section of a MAPS pixel (TowerJazz 180 nm imaging CMOS with the deep p-well feature) [13].

To enhance the performance of the detector, the ASV of the device should be fully depleted to collect charge by drift and not by diffusion: this improves radiation hardness and ensures a fast time response. In addition, both n-type and p-type transistors are necessary in the pixel area to develop efficient processing blocks, required to increase spatial resolution in vertexing and tracking [7].

In Figure 2.8 the cross section of the ALPIDE (ALice PIxel DEtector) sensor is shown. The ALPIDE sensor is the final version of the family of sensors developed by the ALICE collaboration for the upgrade of the ITS. The ALPIDE chip has a pixel matrix of 1024 × 512 pixels, with 28 μm of pitch and is thinned down to a total thickness of 50 μm and is bui8lt in the TowerJazz 180 nm process. In the ALPIDE a deep p-well is implemented, which prevents the n-wells (which host circuitry, i.e. PMOS transistors) from collecting signal charge from the epitaxial layer: this allows the use of full CMOS and complex readout circuitry in the pixel. ALPIDE has high resistivity, 25 μm thick epitaxial layer, which has been shown to improve radiation tolerance since charge is collected by drift. Applying a reverse bias (few V) to the substrate, increases the tolerance to non-ionizing energy loss (NIEL) beyond 10^{13} n_{eq}/cm^2. However, the depletion region is limited to the area around the collection electrode and the charges generated outside this part are collected mainly by diffusion.

NIEL tolerance better than 10^{13} n_{eq}/cm^2 is one of the requirements for the ITS3 upgrade: for this reason some modifications to the standard MAPS process are being tested. The goal is to achieve depletion over the full sensitive layer, to push the charges generated to the collection electrode and reduce noticeably their collection time and the probability of capture by radiation-induced defects or traps (for more details, refer to chapter 3), which would lead to signal loss [23].
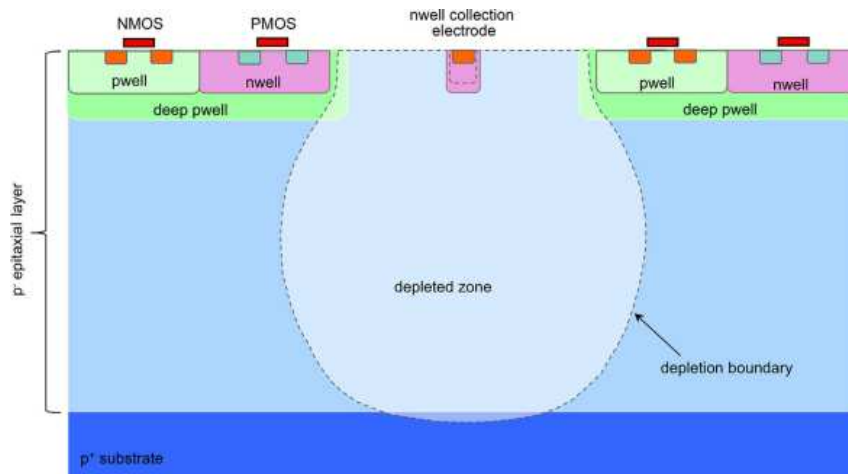

Figure 2.8: Cross section of MAPS standard process: the deep p-well shields the n-wells with the circuitry from the sensor; in the standard process the epitaxial layer is not fully depleted [23]

The size of the depleted region increases with increasing reverse bias applied (see Equation 2.9), but it is still difficult to expand it far in the epitaxial layer. Building a larger collection electrode, thus increasing the size of the junction, would make it easier to deplete over the full pixel volume, but it would affect negatively the power consumption and the input capacitance [24].

In Figure 2.9, the cross-sections of MAPS, in TowerJazz 180 nm, modified processes are shown with the corresponding electric field distribution. [7].

The modified process version of MAPS (see left side in Figure 2.9) is obtained adding a low dose n-type implant for homogeneous growth of the depletion zone with the applied bias voltage. This implant generates a junction able to deplete the 25 μm thick epitaxial layer; it separates the deep p-well of the circuit from the p-type substrate, which is reverse biased to fully deplete the region [25].

But several studies have shown a drop in hit detection efficiency after irradiation [26, 27].

Two modifications are possible to further improve the charge collection mechanism: adding a p-type implant in pixel corners (see central part in Figure 2.9) or adding a gap in the n-type blanket (see right

side in Figure 2.9) can help shape the electric field towards the collection electrode. These designs have been optimized in TCAD simulations[13], which suggest that these modification improve the charge collection at the corners of the pixel. As can be seen from the TCAD simulations in Figure 2.9, the minimum of the electric field (represented by the black star) in the modified processes (with p-implant and with gap) is deeper into the silicon compared to the simple modified process: the electric field bends towards the collection electrodes already deeper in the silicon, thus reducing the drift path and consequently the charge collection time [28].
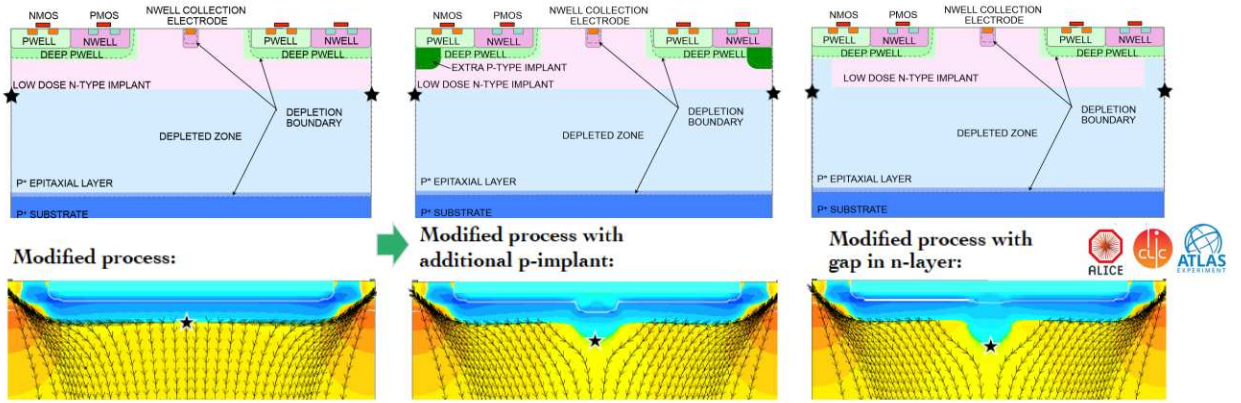
Figure 2.9: Cross-sections of MAPS structures (upper part) and the electric field lines (lower part) in modified versions. In the lower part, the black arrows mark the electric field stream lines, the star symbol indicates the electric field minimum, the white lines mark the edges of the depleted regions [7].

These approaches are at the basis of new generation MAPS, thinner and with increased-resistivity substrate, which will be built for the developments for the ITS3 if the ALICE experiment at CERN LHC.

2.5 Properties

In this section some silicon pixel properties are discussed.

2.5.1 Charge motion and signal formation

The electrical signal used to detect a particle is produced on the collecting electrodes by charges drifting in the electric field, i.e. a signal is detectable as soon as the charge starts to move. According to the Shockley–Ramo theorem [14] [29, 30], the instantaneous current induced on a a nearby electrode is given by:

$$i = eE_W \cdot v \tag{2.11}$$

where v is the drift velocity and E_W is the the so called weighting field. The weighting field is not the actual electric field inside the sensor, but it is the calculated component of the electric field in the direction of v at the instantaneous position of the charge, under the following conditions: the charge is removed, the potential of readout electrode is set to 1 volt, and all other conductors grounded [31].

In pixel detectors, since the size of the collecting electrode is comparable or even smaller than the wafer thickness, there is a larger area inside the pixel where the weighting field approaches zero: this means that a very small signal is induced on the collecting electrode during the drift of the charge in this region. Therefore in pixel sensors most of the signal is induced in the last portion of the drift

---

[13]Technology Computer Aided Design simulations https://www.synopsys.com/manufacturing/tcad.html
[14]The proof is based on the idea that the current induced on an electrode is due to the instantaneous change of the quasi-static electric flux through it, and not on the amount of charge that is collected per second.

path. This effect becomes important in the case of irradiated sensors, when an important part of the signal charge can be trapped due to defects caused by irradiation.

2.5.2 Spatial resolution

The spatial resolution is mostly determined by the pixel pitch, and it can be calculated using the following formula[15], for a binary readout:

$$\sigma = \frac{pixel\,pitch}{\sqrt{12}} \tag{2.12}$$

For an analog readout, the spatial resolution is given by:

$$\sigma = \frac{pixel\,pitch}{SNR} \tag{2.13}$$

where SNR is the Signal to Noise Ratio.

2.5.3 Pixel capacitance

The total capacitance of each pixel affects the noise of the detector. The total pixel capacitance has two main contributions:

- capacitance to the back side, determined by the pixel area A, the sensor thickness d and the relative dielectric constant ϵ_r of the sensor material, in this case, silicon:

$$C = \epsilon_0 \epsilon_{Si} \frac{A}{d} \tag{2.14}$$

- interpixel capacitance, it is the contribution given by the neighbour pixels, it causes cross talk (i.e. the induction of a signal on neighbours pixels by a signal charge deposited on one pixel).

2.5.4 Leakage current

The leakage current (or dark current) is the current induced by thermally created e^-/h^+ pairs: this current flows even if no particles or photons cross the detector when a bias is applied. After a particle crosses the detector, its signal adds to the leakage current background: thus it is essential to keep it as low as possible.

The leakage current strongly depends on the temperature and can be expressed as follows:

$$I_{leak} \propto T^2 \exp\left(-\frac{E_g}{2k_B T}\right) \tag{2.15}$$

where T is the absolute temperature in Kelvin, E_g is the silicon band gap energy and k_B is the Boltzmann constant[16].

Different sources may contribute to the total noise of a pixel sensor. Noise sources in the pixel include the photon shot noise, reset (kT/C) noise, dark current shot noise and the input MOS device noise. Other noise sources are the readout circuitry outside the pixel itself. Normally the total electronic noise in a sensor is higher than the contribution due to the leakage current. But after irradiation, the leakage current increases and it becomes an important noise source, as it is explained in detail in chapter 3.

---

[15]For the uniform distribution $F(x) = 1/(b-a)$, the mean is $\mu = \int xF(x)dx = (a+b)/2$ and the variance is $\sigma^2 = \int (x-\mu)^2 F(x)dx = (b-a)^2/12$.
[16]$k_B = 1.380649$ J K^{-1} (exact) $= 8.617\,333\,262...\times 10^{-5}$eV K^{-1}.

2.5.5 Charge sharing

Charge sharing consists in the lateral spread among several pixels of charge carriers, before reaching the collection electrode. It is clearly influenced by the presence (or not) of an electrical field and for this reason the effect is higher when the charge collection mechanism by diffusion is dominant. In fact, if the charges created by a particle in the sensing volume are collected by diffusion, they can move freely inside it and finally reach a collection electrode, which is not necessarily the one corresponding to the pixel where the particle crossed the detector. To suppress this effect, the electric field should be optimized to accelerate the charge from the pixel edge to the proper collection electrode.

2.5.6 Radiation hardness

Silicon pixel sensors used in HEP experiments are exposed to high levels of radiation, which leads to the steady degradation of the properties of the detector; in particular signal collection in not as efficient as it should be.

There are two strategies to improve radiation hardness: the first one is to study the material properties after irradiation and optimise the design of the device consequently, the second one is to modify the material properties adding specific impurities to reduce the effects of radiation (for example, enrichment of silicon with oxygen) [20].

A detailed discussion of radiation induced effects on silicon is given in chapter 3.

Chapter 3

Radiation induced effects on silicon

In this chapter, a general explanation of the radiation damage on silicon is given. For the scope of this thesis, only radiation damage by non-ionizing radiation is relevant.

3.1 Radiation damage: from HEP experiments to other applications

Radiation affects silicon sensors and all devices built with semiconductor junctions (FPGA, RAMs, controllers, processors). For this reason radiation effects in electronics are a serious concern for the performance and survival of sensors and devices operating in any radiation environment, from accelerator environments, to nuclear power plants, outer space, high altitude aircraft, as well as high-reliability equipment at sea-level. Radiation tolerant devices are required not only for High Energy Physics experiments (such as ALICE), but are also necessary for accelerator based oncology and industrial facilities, satellites in space and scientific activities in deep space, on the moon and planets, avionics, even mundane commercial, automotive, industrial safety control and Information Technology systems.

The devices used in satellite, for example, experience radiation generated by several sources: protons and heavy ions emitted by the sun, particles trapped in the magnetic field of the Earth and galactic cosmic rays. In HEP experiments, the radiation environment depends strongly on location within the experiment (the closer to the collision point, the stronger the levels of radiation). For this reason, inner detectors must tolerate very high radiation fluxes. On Earth, instead, radiation sources can be cosmic or terrestrial. Cosmic radiation derives from sources outside the solar system and interacts with the atoms present in the atmosphere. Terrestrial radiation derives from soil, rocks, water and air [32].

A distinction to make is whether the radiation-induced effect is the result of cumulative damage from the passage of many energetic particles, or it is the result of the passage of a single particle. For this reason, the effects of radiation in silicon devices can be divided in the following different categories:

- *Single Event Effects* (SEEs), caused by single heavily ionizing particles;

- *Total Ionizing Dose Effects* (TID), caused by ionizing radiation that can transfer energy to atomic electrons (photons such as X-rays and γ-rays, and any charged particle);

- *Bulk damage*, due to Non-Ionizing Energy Loss (NIEL), quantified by the cumulative Displacement Damage Dose (DDD), caused by particles capable of transferring energy to atomic nuclei (neutrons, pions, protons, ions).

3.2 Single Event Effects

If a charged particle strikes a sensitive node of an electronic circuit, it may cause a disruption or a permanent damage: this is a Single Event Effect (SEE). Single Event Effects can be divided in two

categories: non-destructive and destructive effects.

Non-destructive SEEs do not damage or destroy the actual circuit component, but they cause a corruption in output or data state. Therefore, the circuit functionality is restored once the excess charge stuck in the junction, left after the particle crossed the detector, has been removed by carrier recombination or carrier transport. In this case, only the data is corrupted, and for this reason non-destructive SEEs are also called "soft errors". An example of non-destructive SEEs are Single Event Upsets (SEUs), which appear as bitflips in memory cells or registers, or Single Event Transients (SETs), which appear as transient pulses in logic circuitry. These effects may affect digital, analogue and optical components.

Destructive SEEs cause a corruption in output or data state and permanently damage or destroy the actual circuit component. For this reason, destructive SEEs are called "hard errors". An example of a destructive SEE is the Single Event Latch-up (SEL), which results as high operative current (different from the specifications of the device), and a power reset is needed to restore the normal operation conditions.

A detailed description of nondestructive and destructive effects can be found in [33] and in [34], respectively.

3.3   Surface Damage, Total Ionizing Dose effects

Total Ionizing Dose (TID) is defined as the energy absorbed by a unit mass of material when it is exposed to ionizing radiation. In the International System of Units, TID is measured in Grays (Gy) (1 Gy = 1J/kg). Another unit often used is the rad (1 Gy = 100 krad). TID effects consist of the generation, transport and trapping of holes in the isolation oxides in metal-oxide semiconductor (MOS), in the insulation used as gate and near the silicon-oxide interface.

When ionizing radiation crosses a piece of conductor or semiconductor material (like metals and silicon, respectively), the excess of charges generated is compensated by recombination, and/or dissipated by diffusion and drift (under the effect of an electric field): the charges are removed from the area in a short time interval, hence no charge is accumulated or stored.

For insulating material the effects are totally different. The energy absorbed by radiation exposure in insulators creates a number of effects in the oxide that can degrade the performance and the functionality of the device. Insulators are widely used in MOS transistors. Silicon dioxide (SiO_2) is the most commonly used dielectric material for the gates of MOS transistors; oxide spacers are used to insulate the drain and source metal contacts from the gate of the transistors; Shallow Trench Isolation (STI) oxide is used to avoid contacts between adjacent devices. The electrical isolation is achieved using trenches created in the Si substrate around the active elements and filling it with an insulating dielectric, such as silicon dioxide.

Therefore, it is mandatory to know the effects of radiation on insulators and find solutions to mitigate these effects.

There are four physical process [35], that contribute to the radiation response of a MOS device (see Figure 3.1):

(1) electron/hole pair generation and recombination;

(2) hole transport to the interface between Si an SiO_2;

(3) deep hole trapping and annealing;

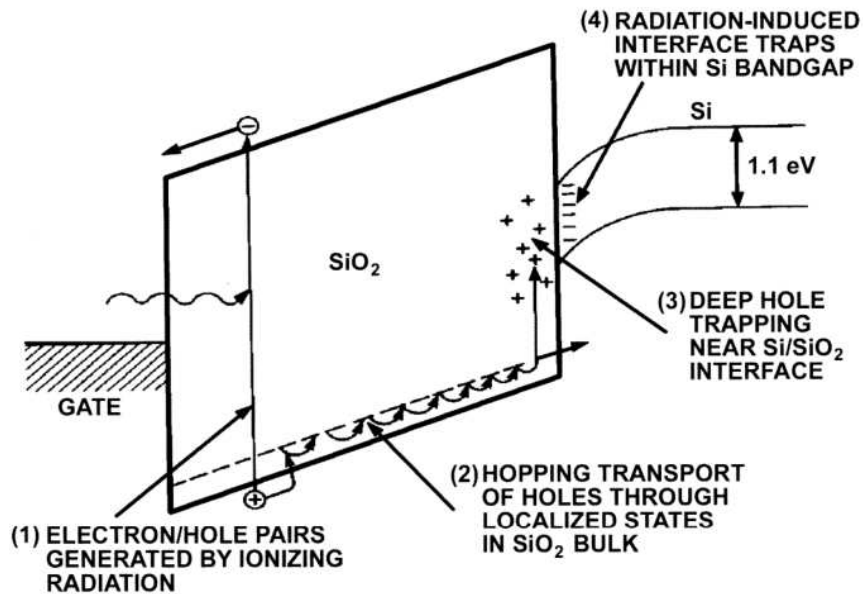(4) radiation-induced buildup of interface traps at the Si/SiO_2 interface.

Figure 3.1: Scheme of the physical processes happening when ionizing radiation crosses a MOS structure [35].

Electron/hole pair generation and recombination

When a particle crosses the device, electron/hole pairs are generated. In SiO_2, electrons are much more mobile than holes and they are removed from the oxide in short times (of the order of ps) under the effect of the electric field. In spite of this, some electrons will recombine with holes. The fraction of recombined electrons depends on the type and energy of the incident particle. The holes which escape initial recombination are relatively immobile, and remain near their point of generation. The fraction of holes that do not recombine (*charge yield*) is influenced by two factors: the magnitude of the electric field (which separates the pairs), and the initial line density of pairs created when radiation crosses the device. The latter factor is regulated by the Linear Energy Transfer (LET), hence it depends on the type and the energy of the incident particle; the initial line density is also inversely proportional to the average distance between electron/hole pairs: the smaller the distance between the pairs, the higher is the number of recombinations and the less the hole yield [35].

Hole transport to the interface between Si an SiO_2

The hole transport process depends on the electric field, the temperature and the oxide thickness. The best description of this process is given by the continuous-time-random-walk (CTRW) hopping transport model, in which the holes "hop" through the oxide as small polarons[1].

As already mentioned before, the holes that do not recombine are relatively immobile. Then, under the influence of the applied bias voltage, they begin to move towards the gate or the Si/SiO_2 interface by a slow polaron-hopping process [37].

The hopping process breaks chemical bonds, releasing trapped protons (H^+), which diffuse or "drift" following the same direction of the holes. As holes move towards the SiO_2/Si interface, they get trapped in mid-band-gap traps near the interface - causing a positive charge accumulation at first - or are captured at the interface.

---

[1]A conduction electron (or hole) together with its self-induced polarization in a polar semiconductor or an ionic crystal forms a quasiparticle, which is called a polaron [36].

Deep hole trapping and annealing

Deep hole traps come up near the Si/SiO_2 interface. In this region the oxidation is not complete and there is an excess of Si, or oxygen vacancies. These vacancies form energetically deep hole traps, and at room temperature the thermal energy is not large enough to allow hole release from the traps. The positive charge associated with trapped holes causes a negative voltage shift in both N and P-channel MOS transistors. The trapped holes cause an accumulation of positive charge in MOS and bipolar devices during irradiation. This positive charge can be neutralized by tunneling or thermalized electrons injected from the silicon: the normal bonding structure is restored, and the defect is "annealed out" [37].

Radiation-induced buildup of interface traps at the Si/SiO_2 interface

Radiation-induced interface traps at the Si/SiO_2 interface cause voltage-dependent threshold shift (positive or negative according to the applied bias). These shifts decrease carrier mobility and increase the rate of surface recombination. Interface traps are localised states with energy levels in the silicon band-gap. These traps are highly dependent on oxide processing, temperature and applied field [35].

3.4 Displacement Damage Dose Effects (bulk damage)

Displacement damage dose describes the physical damage to a semiconductor crystal structure caused by NIEL (non-ionizing energy loss).

NIEL is the part of the energy lost by a traversing particle that does not go into ionization and can lead to displacement damage (DD); it strongly depends on the particle energy and is usually expressed in units of MeV·cm^2/g or as a cross section in units of MeV-mb. Only a fraction of NIEL leads to DD, because part of the impinging particle energy is dissipated in phonons. Figure 3.5 shows calculated values of NIEL cross sections for different particles [31].

According to the NIEL hypothesis, the radiation damage effects scale linearly with the NIEL, in spite of the energy and space distribution of the primary displacements. Therefore, NIEL scaling is useful to make predictions of displacement damage in complex radiation fields.

The DD is caused by an incident particle with sufficient energy to knock a silicon nucleus off its initial location in the crystal lattice, which is referred to as *primary knock-on atom* (PKA). After the nucleus is released, a localised vacancy is left in its place, and the interstitial defect, which is the displaced silicon nucleus, is free to move in non-lattice positions. Together, the vacancy and the nearby interstitial form a Frenkel pair; the energy required to create a vacancy by displacement ($\sim$ 15 eV in Si) is higher than that required to create electron/hole pairs ($\sim$ 3.6 eV in Si). After its production, the PKA can induce further displacement damage by Rutherford or nuclear scattering: thus lattice defects are produced by PKAs and any energetic recoils that they create afterwards.
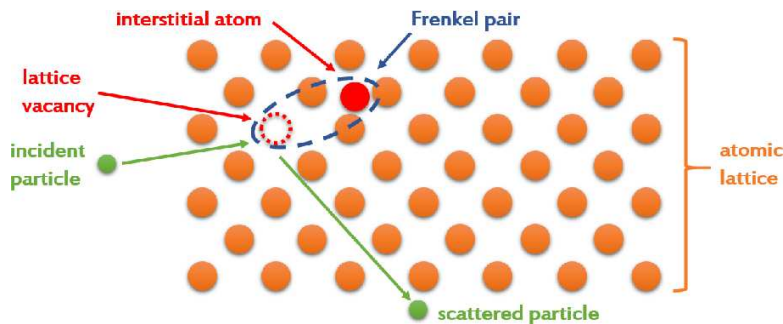

Figure 3.2: Scheme of creation of a Frenkel pair (vacancy and interstitial) in silicon crystal lattice by an incident energetic particle [38].

If the defects produced are far apart, they are called *point defects*; if they are produced closely together, they form a local region of disorder called a *cluster* [1].
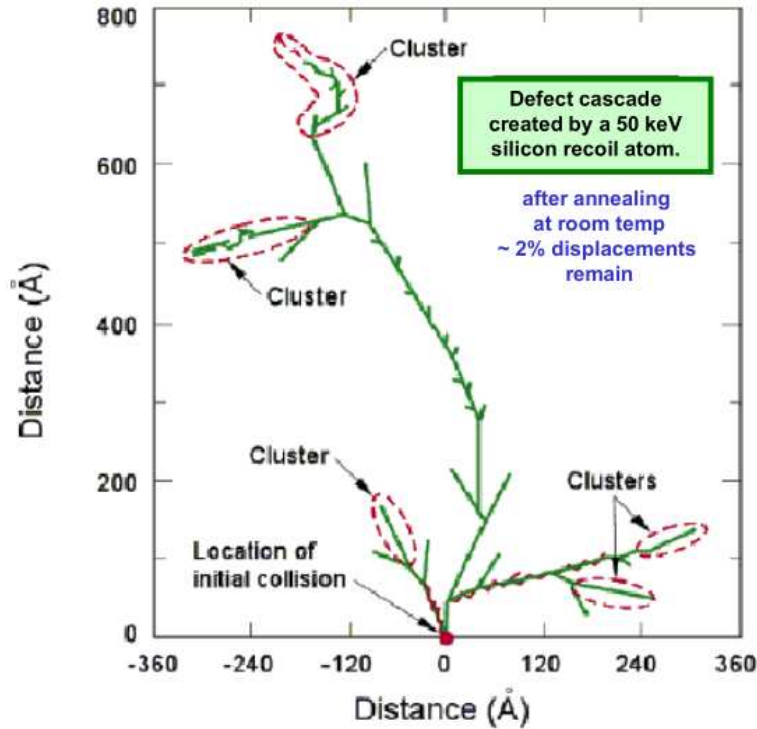

Figure 3.3: Illustration of damage caused by an incident energetic particle (at zero on the x-axis and aimed upward): multiple individual displacements and larger defect clusters are created [1].
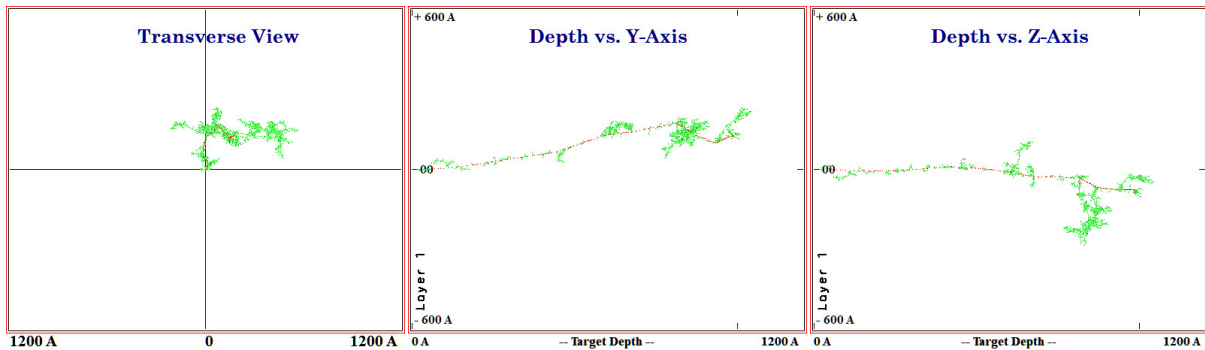

Figure 3.4: Calculation of damage caused by a 50 keV Si ion in silicon using SRIM software[2]. Left: transverse view of an area of 1200Å × 1200Å of silicon. Centre: view of the defect clusters along the y-axis. Right: view of the defect clusters along the z-axis.

DD is a volumetric effect, i.e. the entire silicon volume accumulates damage, which results in changes to the optical and electrical properties of the bulk, whereas TID, as already said in the previous section, consists in the accumulation on the surface of trapped charge and interface states.

Heavy particles such as protons, neutrons, ions, charged pions, and energetic electrons are all responsible for DD damage; very-high-energy X-rays and γ-rays can produce secondary electrons with the sufficient kinetic energy to cause DD too. However, according to the so-called NIEL hypothesis, bulk damage caused by irradiation depends only on the KERMA (Kinetic Energy Release in MAtter), an

---

[2]SRIM (Stopping and Range of Ions in Matter) http://www.srim.org/

energy dependent quantity that accounts for the kinetic energy deposited by particles in the lattice [39] . This quantity can be calculated as:

$$\text{KERMA[MeV]} = \Phi[\#/\text{cm}^2] \cdot wt[\text{g}] \cdot \text{NIEL[MeV cm}^2\,\text{g}^{-1}] \tag{3.1}$$

or:

$$\text{KERMA[MeV]} = \Phi[\#/\text{cm}^2] \cdot N_{\text{atoms}} \cdot 10^{-27}[\text{cm mb}^{-2}] \cdot \text{D[MeV mb]} \tag{3.2}$$

where Φ is the flux of incident particles per cm^2, wt is the weight of the target, and D is the damage function, which is defined as:

$$D(E) = \frac{W_A}{N_A}\text{NIEL(E)} \tag{3.3}$$

where W_A is the atomic weight and N_A is the Avogadro's number.

The NIEL hypothesis is based on the assumption that the generation of bulk damage is only due to non-ionizing energy transfers to the lattice, that the concentration of the defects is independent of the properties of the incident particle, and that the amount of the defects is proportional to the NIEL. This implies a scaling hypothesis: any particle fluence can be scaled and reduced to that of an equivalent 1 MeV neutron fluence that produces the same bulk damage in a specific semiconductor. The bulk damage can be compared and scaled if the particle energy E and the corresponding NIEL, or its damage factor D, are known. The damage factor of 1 MeV neutrons is defined to be 95 MeV-mb. Hence, it is possible to compare damage induced by high energy neutrons, that make large clusters, with the damage induced by low energy neutrons, that displace just one atom, or with the damage due to charged pions. In Figure 3.5, the damage function D(E) for different particles is shown.
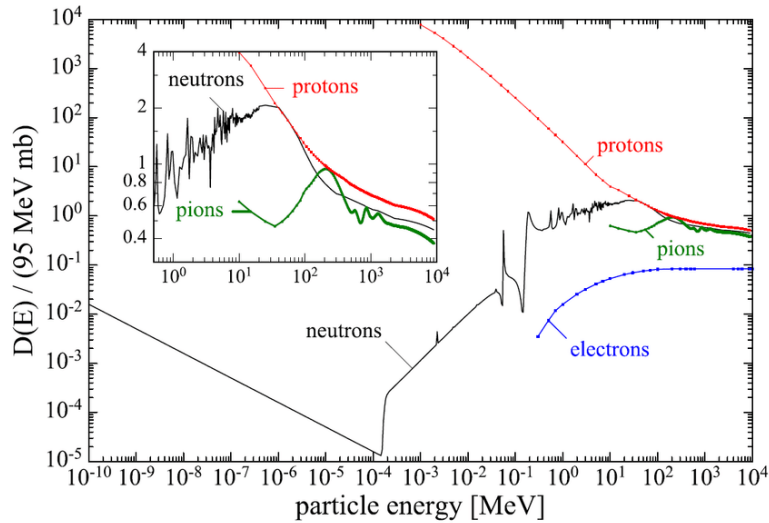
Figure 3.5: Damage function normalized to that of 1 MeV neutrons (95 MeV-mb) [3], as a function of energy, for protons, neutrons, pions, and electrons [31].

Displacement Damage effects

The main effects due to displacement damage are [1]:

- reduction of recombination lifetime and diffusion length;

- decrease of generation lifetime;

- increase of majority and minority carrier trapping, which affects charge collection efficiency;

  - changes of majority-carrier concentration, due to carrier removal[4], which affects the overall performance of the device;

  - increase of thermal generation of electron-hole pairs under the effect of a sufficiently high electric field, which leads to an increase of the dark current;

  - reduction of carrier mobility.

The impact of radiation-induced defects on silicon sensors performance can be described using the Shockley-Read-Hall (SRH) statistics and the impact of each defects can be calculated, knowing the capture cross section for holes and electrons, the position in the bandgap, the type of defect (donor or acceptor) and the defect concentration [40].

In the SRH framework, three main effects on the detector performance level can be identified [31]: *leakage current*, *effective space charge*, and *trapping*.

Leakage current

Defect levels close to the middle of the bandgap increase leakage current, because these levels are very efficient charge carrier generation centers. The leakage current comes from the detector bulk.

An increase of leakage current causes an increase of power consumption and an increase of noise in the amplifiers. The leakage current is proportional to the temperature [41] according to the following expression:

$$I_{leak} \propto T^2 \exp\left(-\frac{E_g}{2k_B T}\right) \tag{3.4}$$

where T is the temperature, E_g is the silicon bandgap energy and k_B is the Boltzmann constant.

This means that, in order to mitigate the detrimental effects, cooling the device is helpful.

The radiation-induced increase of the leakage current is independent of the type, resistivity, and impurity content of the silicon material, but only depends on the particle fluence. The *current related damage factor* α is defined as:

$$\alpha = \frac{\Delta I}{V \phi_{eq}} \tag{3.5}$$

where ΔI is the radiation-induced current increase, V is the volume contributing to the current and ϕ_{eq} is the particle fluence. The α value decreases with increasing annealing time.
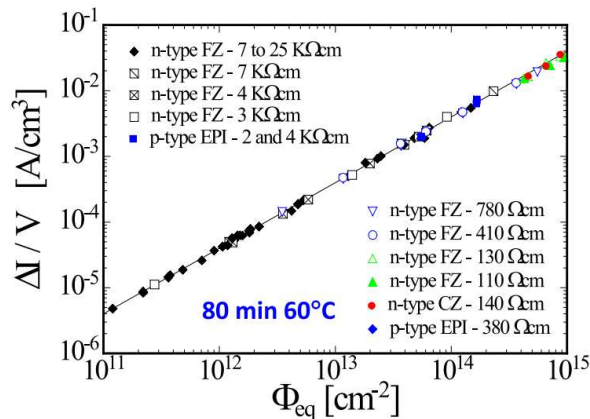
Figure 3.6: Leakage current increase induced by radiation as a function of particle fluence for various silicon detectors: the current was measured after a heat treatment of 80 min at 60 °C [31].

---

[4]Carrier removal consists in the introduction of centres that compensate for donors.

Effective Space Charge

The effective space charge N_{eff} is used to refer to the bulk doping. A change in the effective space charge is induced in irradiated sensors, and this leads to a change of the electric field distribution inside the device and a shift of the depletion voltage V_{dep} to higher or lower values. In the former case, higher voltages are needed to deplete the active area, to avoid signal loss (which is not always possible, for example if breakdown of sensor is at risk). Assuming that the space charge is homogeneous, which is not always the case, the depletion voltage is given as:

$$V_{dep} = \frac{q|N_{eff}|d^2}{2\epsilon\epsilon_0} \tag{3.6}$$

where q is the elementary charge, d is the thickness of the device, ϵ is the relative permittivity of silicon and ϵ_0 is the vacuum permittivity. It has been demonstrated that space charge changes in silicon strongly depend on the material (e.g. the amount of oxygen present in the device volume) and on the type of particle used for the irradiation (for example, neutrons or protons). The change of impurity content can reduce some of these effects.

Irradiation causes the formation of negative space charge, compensating the initial positive space charge in n-type sensors; in p-type sensors the initial space charge is already negative. Increasing particle fluence causes the net space charge to decrease and reach very low values, that correspond to almost intrinsic silicon. The point where this happens is called *type inversion* or *Space Charge Sign Inversion* (SCSI). The more the fluence is increased beyond the SCSI point, the more the net space charge becomes negative, and the depletion voltage increases, until it reaches values that could cause the breakdown. Therefore, the detector is operated in underdepleted mode, and the signal measured is lower than it could be.
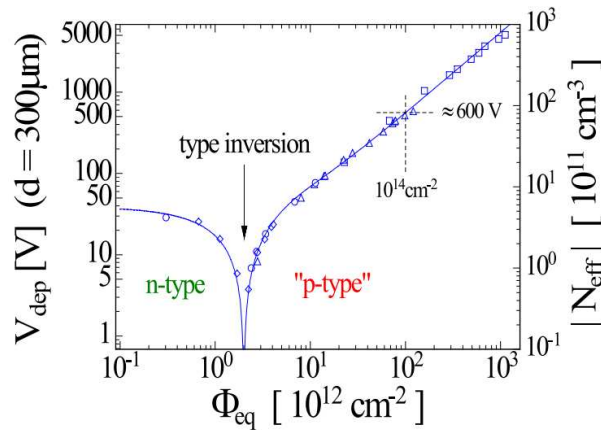
Figure 3.7: Depletion voltage as a function of the particle fluence [31].

Trapping

Defect levels can trap charge carriers, and if the release time of the charge carriers is long with respect to the collection time or if the concentration of the trapping centres is high, the total signal is reduced.

As particle fluence increases, more and more charge carriers get trapped, causing a decrease of the charge collection efficiency (CCE). This effect can be described using the effective trapping time τ_{eff}[5], assuming that the charge loss depends only on transport time of charge carriers inside the sensor: $Q(t) = Q_0 \exp(-t/\tau_{eff})$. The inverse effective trapping time linearly depends on the particle fluence, and is given by:

$$1/\tau_{eff} = 1/\tau_{(eff,0)} + \beta\phi_{eq} \tag{3.7}$$

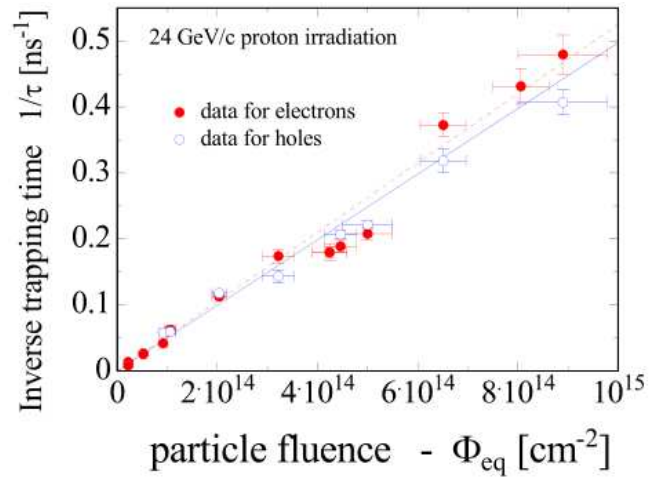[5]The effective trapping time can be measured for electrons and holes separately.

Figure 3.8: Inverse trapping time as function of particle fluence, measured at 0 °C after an annealing of 30 to 60 min at 60 °C [31].

where $\tau_{(eff,0)}$ is the effective carrier lifetime before irradiation, and β is the proportionality factor (effective trapping damage constant). This constant depends on the annealing status of the sensor after irradiation.

Table 3.1: Summary of radiation damage processes and effects caused by different particles in silicon.

Particle	Process	Micro-effect	Macro-effect	Type of effect
heavy charged particles (protons, ions)	direct ionization	sudden localized large ΔE_{ioniz} deposition	Single Event Effects (**SEEs**)	stochastic
energetic heavy particles (protons, neutrons, energetic ions)	secondary ionization by recoil atoms and nuclear fragments	sudden high large ΔE transfer to a single nucleus	Single Event Effects (**SEEs**)	stochastic
neutrons, low energy ions (near end of range)	non-ionizing energy loss	creation of primary knock-on atoms (PKA)	Displacement Damage Dose (**DDD**) effects	cumulative
charged particles, photons	direct ionization or by conversion	small ΔE_{ioniz} deposited uniformly, delivered over time by many particles	Total Ionizing Dose (**TID**) effects	cumulative

Chapter 4

Experimental setup

This chapter aims to explain the experimental setup used to test irradiated silicon pixel detectors. These tests represent a crucial part in the upgrading process of the ITS, because they allow a better understanding of which level of irradiation these detectors can withstand, i.e. if the main properties of the detectors, such as charge collection efficiency, are significantly degraded or not.

Before going into details of the experimental setup, a brief overview of the different sensors flavors and processes is given.

4.1   MLR-1

Generally, the reticle size used in CMOS manufacturing restricts the size of the chip to a few cm^2. For the ITS3 upgrade, however, the target is to build 300 mm wafer-scale chips using the stitching technique, which allows the fabrication of sensors larger than the field of view of the lithographic equipment used in the production process. This is done exposing parts of the mask in a periodic, aligned fashion to create a circuit that continues across several exposures.

Moreover, for the new ITS, 65 nm Imaging Sensor Chip process will be used (the currently working ALPIDE chips are implemented in Tower Semiconductor 180 nm Imaging Sensor Chip process). Moving from the 180 nm to the 65 nm technology node will allow a lower power consumption and a more dense circuitry.

Several technology qualification structures have been produced and tested, to prove the 65 nm process to be fully compatible with the ITS3 needs in terms of charge collection behaviour under the ITS3 radiation environment.

Test structures with several levels of pixel technology optimisation, transistor test structures and building blocks have been designed and submitted in a first multi-reticle-layer run (MLR-1) in 2021, containing 55 different structures.

The pixel test structures contain matrices of pixels and allow the qualification of the pixel cell in terms of charge collection efficiency depending on radiation, pixel size, reverse bias and process optimisation. Three different structures have been fabricated:

- Analogue Pixel Test Structures (APTS): a 4×4 pixel array, with parallel analogue readout for the whole matrix, comes in 4 variants of pixel pitches (10, 15, 20, 25 μm), two output buffer versions (source follower SF and OPAMP), three design variations (for more details, see section 4.2);

- Digital Pixel Test Structures (DPTS): a 32×32 pixel array with a 15 μm pixel pitch and asynchronous digital readout;

- Circuit Exploratoire 65 (CE65): a pixel matrix with a rolling shutter readout, single analogue output, comes in two different sizes (64×32 and 48×32, with pixel pitch 15 and 25 μm, respec-

tively); it is divided in 3 sub-matrices, each with different in-pixel electronics (AC OPAMP, DC OPAMP, source follower).
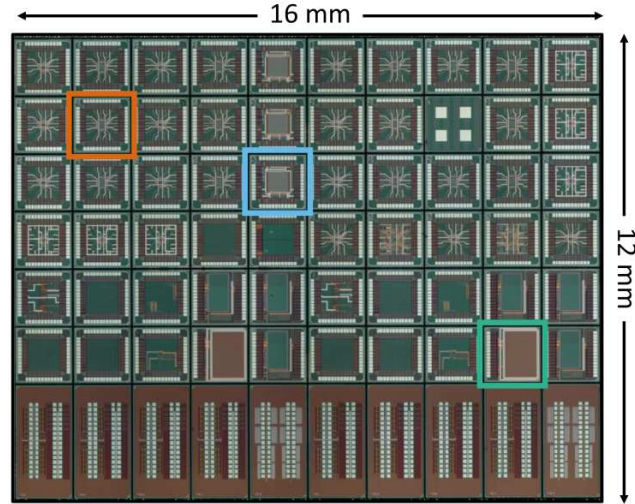
Figure 4.1: The MLR-1 reticle floor plan highlighting the APTS (orange), CE65 (green) and DPTS (blue) chips [8]. The bottom part is an array of transistors test structures (TTS) used for radiation damage studies on electronics.

Three process options are being tested to study the charge collection properties of the CMOS process: the standard, the modified and the modified-with-gap (see Figure 4.2).

In the standard process, the depletion layer is balloon-shaped. It extends from the junction at the collection electrode, and does not reach the pixel edges. Charge is collected from outside the depletion layer primarily by diffusion, but this collection is relatively slow and subject to charge trapping in defects generated by exposure to non-ionizing radiation.

The modified process and the modified-with-gap version (already described in section 2.4) are designed to fully deplete the epitaxial layer, reducing charge sharing and improving the radiation tolerance to non-ionizing radiation.

The three process modifications implemented in the MLR-1 (shown in Figure 4.2), have been manufactured in four different process variations (referred to as *splits*) with different doping profiles (more details can be found in [42]). The *split 1* chip, is the one built with the standard process without modifications; the *split 2* chip, is the one built with the modified process with the deep p-well to improve isolation between circuitry and sensor. The *split 3* chip, adds to split 2 a deep n-well adjustment in the pixel to allow full depletion, and the *split 4* chip, adds to split 3 a deep p-well modification to prevent potential well created by the additional in-pixel circuitry. Split 3 and split 4 have a smaller input capacitance, which results in a larger signal at the input node of the in-pixel front end, and leads to lower power consumption, because a lower amplification is required. Split 4 has been chosen as baseline for further studies.
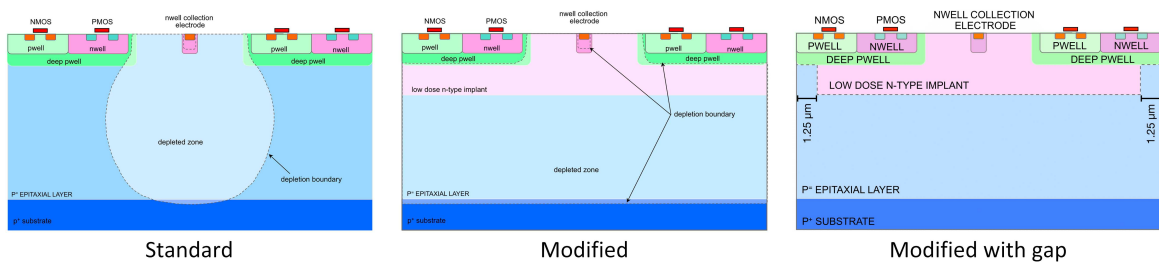
Figure 4.2: The three process options implemented in the MLR1 chips [8].

4.2   Analogue Pixel Test Structures

The Analogue Pixel Test Structures (APTS) are the tools used to study the properties of the sensors designed for the next ITS3 upgrade. Each APTS chip measures 1.5 mm × 1.5 mm. The pixel matrix is composed of 4×4 active pixels, surrounded by a ring of dummy pixels (for a total of 6×6 pixels). All the 16 pixel outputs are buffered and routed individually to their dedicated pads.

The output buffer has been implemented in two versions: a source-follower (APTS-SF, see schematic in Figure 4.3) and a fast operational amplifier (APTS-OA).

The sensors were produced with 4 different pixel pitches (10, 15, 20, 25 μm) and with 3 processes (standard process, modified process with additional deep implant and modified process with gap in the additional deep implant, see Figure 4.2).

The overall sensor thickness is of 50 μm; the p-type epitaxial layer is $\approx$ 10 μm thick; its resistivity is such that it is fully depleted with few Volt of reverse bias ($\lesssim$ 4.8 V).

APTS tested in laboratory

Some APTS versions were studied in our laboratory using radioactive sources, before and after irradiation. All the sensors tested feature a source follower front-end (APTS-SF), come from split 4 and implements the process variant modified with gap. The pixel pitch was 10 μm (AF10P_W22B57, AF10P_W22B58, AF10P_W22B61, AF10P_W22B63) and 15 μm (AF15P_W22B23). The chip with 15 μm pixel pitch has not been irradiated, whereas all the others have been irradiated at the JSI TRIGA neutron irradiation facility: in these cases we expect only bulk damage.

The JSI TRIGA neutron irradiation facility is a global reference centre for silicon detector irradiation; it has a dedicated irradiation channel for radiation damage studies of large size Si detectors along with the associated electronics, that can vary the temperature using a heating/cooling module installed inside the channel [43]. The irradiation levels start from 1×10^{14} n_{eq}/cm^2 and go up to 5×10^{15} n_{eq}/cm^2. During the irradiation process, due to the gamma background, the chips were exposed to a TID of approximately 1 kGy at 10^{14} n_{eq}/cm^2, linearly scaling with fluence, which is lower than the radiation load for the ITS3 of 10kGy.
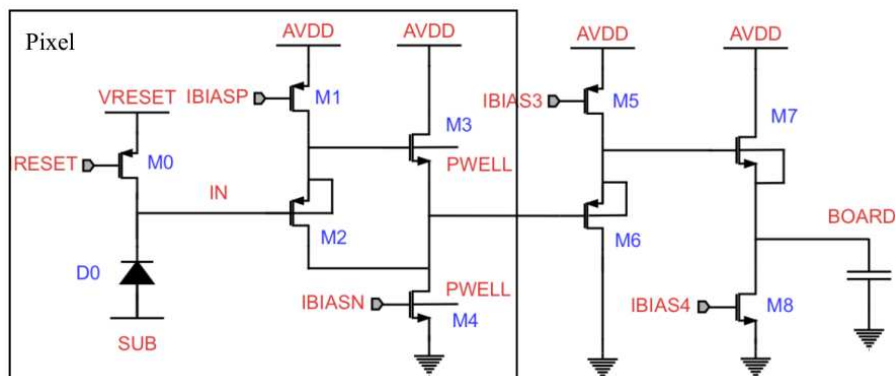
Figure 4.3: Schematic of APTS source follower (SF) version: the SF gain is $\lesssim$ 1 and the output voltage is proportional to the input voltage.

Table 4.1: Summary of information about the tested APTS: pixel pitch, irradiation level (neutron fluence), split, thickness, wafer and location where the measurements were taken.

CHIP	Pixel pitch	neutron fluence	Split	Thickness	Wafer
AF15P_W22B23	15 μm	not irradiated	4	50μm	22
AF10P_W22B25	10 μm	not irradiated	4	50μm	22
AF10P_W22B57	10 μm	1×10^{14} n_{eq}/cm^2	4	50μm	22
AF10P_W22B58	10 μm	1×10^{15} n_{eq}/cm^2	4	50μm	22
AF10P_W22B61	10 μm	2×10^{15} n_{eq}/cm^2	4	50μm	22
AF10P_W22B63	10 μm	5×10^{15} n_{eq}/cm^2	4	50μm	22

To greatly reduce annealing, the chips are stored in a freezer at temperature $T \sim -20$ °C. To perform measurements, the chips are transferred into a cold box set at $T \leq 14$ °C; once the chips are in thermal equilibrium (less than an hour), they are measured. The cold box is used in order to keep under control the radiation induced leakage current, as described in section 4.4.

Figure 4.4: From left to right, carrier boards with chips AF10P_W22B57, AF10P_W22B58 and AF10P_W22B61.

4.3 DAQ, Proximity and Carrier boards

A dedicated DAQ system has been developed within the ALICE ITS3 project, that it is compatible with the existing ALPIDE (ITS2 sensor) DAQ. It controls the bias parameters (currents and voltages) that bring the sensor to the proper working point, manages the data provided by the sensor and allows data transfer to a computer for processing and storage. The system consists of:

- a carrier board, on which the APTS is bonded.

- a proximity board, connected to the carrier board. It hosts 16 ADC converters, required to readout the analogue signal for each channel of the sensor, and provides the proper voltage levels and current biasing to the chip.

- a custom DAQ board, connected to the proxity board and equipped with a programmable FPGA. It is used to control the DUT and to read and process the digital signals coming from the proximity board; it communicates to a computer via a USB cable.

A Keysight E36313A power supply is remotely controlled and used to provide the bias to the DAQ board and the sensor. A voltage of 5 V and 900 mA current limit are set for the DAQ board. Different voltage values (in negative polarity) and 1 mA current limit are sent to the proximity to reverse bias the sensor.
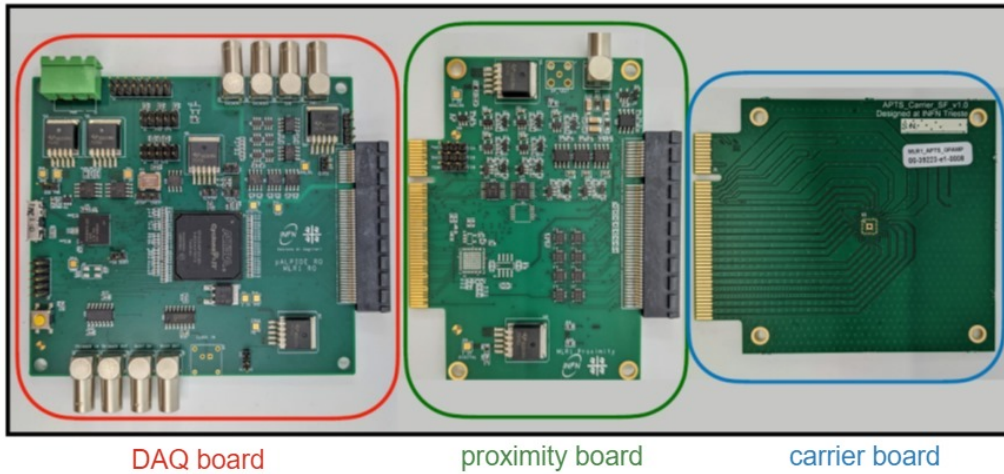
Figure 4.5: DAQ, proximity and carrier boards.

4.4   Cold box and chiller

Irradiated APTS must be operated at a temperature $T \leq 14$ °C. For this reason the RTE-4DD Refrigerated Bath Circulator was used to keep the temperature at the desired value inside the cold box (see Figure 4.6 and Figure 4.8). For the scope of this thesis only the refrigerated bath circulator was used to lower the temperature, but it is also possible to use Peltier cells.

Table 4.2: Specifications for the RTE-4 Constant Temperature Bath

Specifications	RTE-4
Temperature Range	-30 °C to +100 °C
Temperature Stability	± 0.01°C
Bath Work Area (L×W×D)	2.5 cm × 12.1 cm × 22.9 cm
Bath Volume	5.0 L
Unit Dimensions (H×W×D)	44.5 cm × 40.6 cm × 43.2 cm

To prevent condensation, which could threaten the performance of the chips, dry air is fluxed inside the cold box and a fan makes it circulate.

To check the temperature and the humidity inside the cold box, the Temperature Sensor Probe TSP01 has been used.
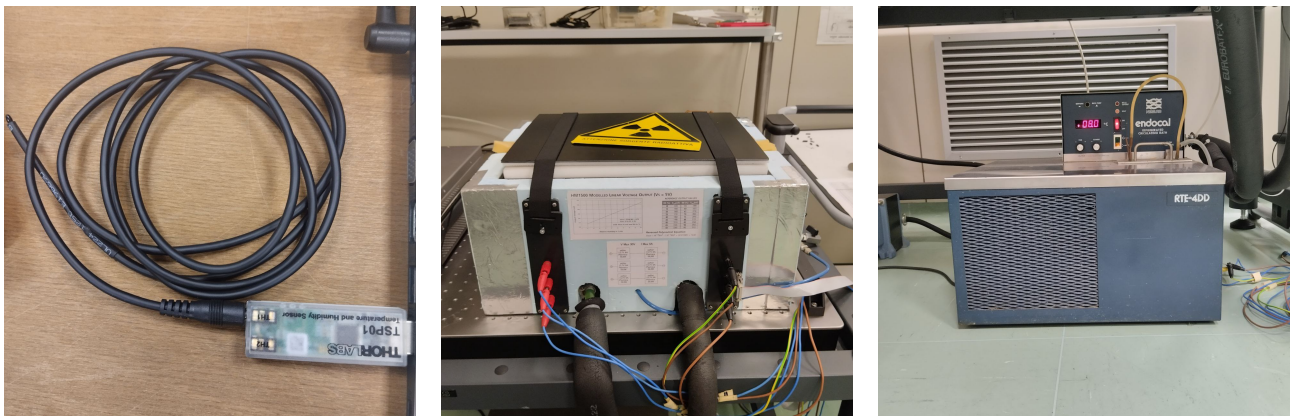
Figure 4.6: Left: Temperature and Humidity Sensor Probe TSP01. Centre: cold box. Right: RTE-4DD Refrigerated Bath Circulator.

In Figure 4.7, the trends of temperature and humidity inside the cold box, over a period of 90 minutes: this check was performed to be sure that the temperature and the humidity levels would be quite stable when doing acquisitions with irradiated chips.
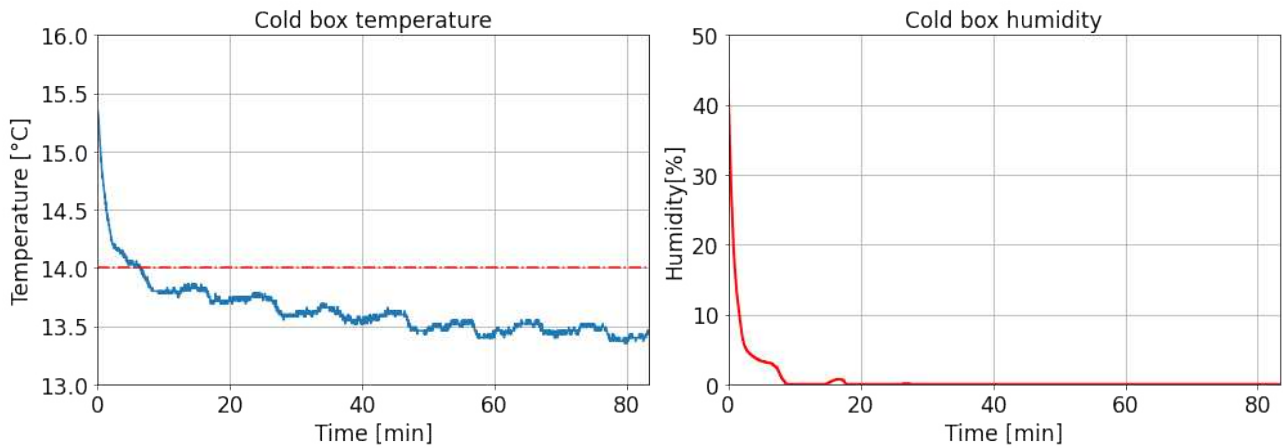
Figure 4.7: Temperature and humidity measurement during data acquisition.
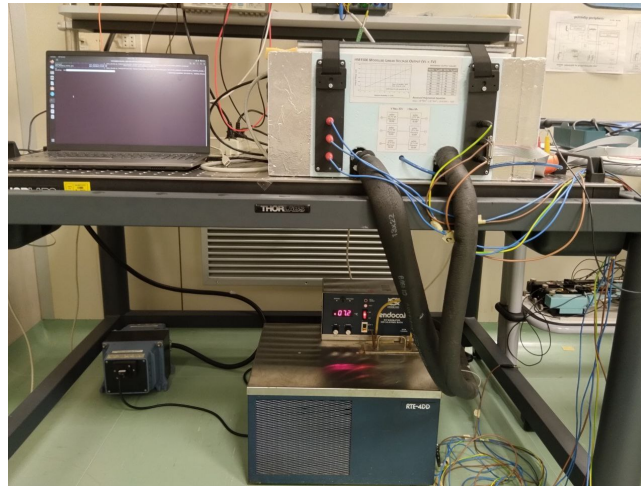
Figure 4.8: Setup: cold-box and chiller.

Chapter 5

Measurement Procedure

The characterisation process of the APTS consists in the following steps, repeated for different reverse bias voltages V_{bb} (0.0 V, -1.2 V, -2.4 V, -3.6 V and -4.8 V):

1. *test pulse (TP)*: to check if all the pixels are working;

2. *threshold scan*: to set the hardware threshold in order to be able to detect the right signals;

3. *gain*: check baseline and working point conditions;

4. *source measurements*: data acquisition with radioactive sources (^{55}Fe, ^{90}Sr);

5. *leakage current tests (LT)*: tests to measure the leakage current.

Not all chips were available at the time of writing. All the tests performed at Padova are reported in Table 5.1. Unfortunately for the sequence of tests with ^{90}Sr, the chip that received the highest fluence was never sent to Padova. Similarly one of the non-irradiated chips was measured at CERN with the ^{55}Fe source, but it too was never sent to Padova and couldn't be pulse tested nor could the leakage current be measured. We hope to receive the chips soon so that they too can be included in an upcoming article.

Table 5.1: Summary of tests performed with the chips.

Chip	Neutron fluence	Test	Location
AF15P_W22B23	not irradiated	TP, ^{55}Fe, ^{90}Sr, LT	Padova
AF10P_W22B25	not irradiated	^{55}Fe	CERN
AF10P_W22B57	1×10^{14} n_{eq}/cm^2	TP, ^{55}Fe, ^{90}Sr, LT	Padova
AF10P_W22B58	1×10^{15} n_{eq}/cm^2	TP, ^{55}Fe, ^{90}Sr, LT	Padova
AF10P_W22B61	2×10^{15} n_{eq}/cm^2	TP, ^{55}Fe, ^{90}Sr, LT	Padova
AF10P_W22B63	5×10^{15} n_{eq}/cm^2	^{55}Fe	CERN

5.1   Test pulse

In order to check the proper functioning of every pixel in each APTS, it is possible to use a test pulse procedure. The test pulse procedure consists in applying a step voltage of 1200 mV to an injection capacitor, put in parallel with the pixel input. This mimics a voltage signal at the input of the front-end circuitry and therefore allows to test the electrical functionality of the pixel cell. The test pulse can be enabled for the whole matrix, for the 4 central pixels, or for the 4 corner pixels. We pulsed all the pixels in the matrix, and repeated the procedure for all bias voltage values V_{bb}.

Figure 5.1 shows the 16 pixel outputs for the matrix irradiated to 1×10^{14} n_{eq}/cm^2, when the test pulse is applied, in a time window of 25 μs before the test pulse and 25 μs after it, for all V_{bb} values.

Figure 5.2 and Figure 5.3 show the same results for the chips irradiated to 1×10^{15} n_{eq}/cm^2 and 2×10^{15} n_{eq}/cm^2, respectively. No test pulse data are available for the chip irradiated to 5×10^{15} n_{eq}/cm^2.

Comparing the three irradiation levels available, it is possible to see that all the pixels are properly working after irradiation. For $V_{bb} = 0.0V$ the pixel signal amplitude gets smaller with increasing levels of irradiation, compatible with an increase of the pixel input capacitance after irradiation. This difference is however compensated for at $V_{bb} = -4.8V$, i.e. when the detector is depleted. What is changing with the fluence is the time response of the pixel signal, which gets slower at higher irradiation levels, with a wider spread among pixels.

(a) $V_{bb} = 0.0V$.

(b) $V_{bb} = -1.2V$.

(c) $V_{bb} = -2.4V$.

(d) $V_{bb} = -3.6V$.

(e) $V_{bb} = -4.8V$.
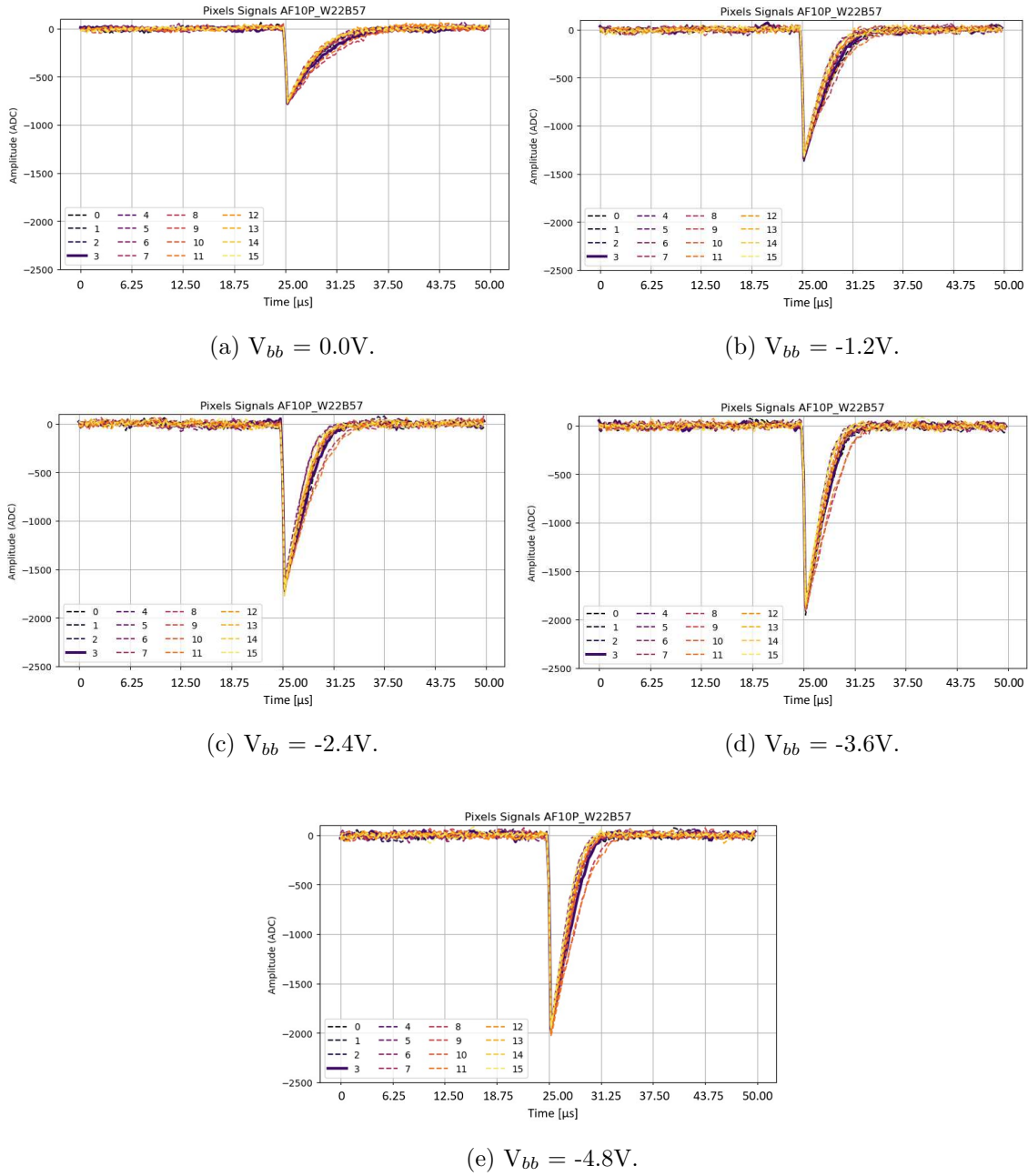
Figure 5.1: Test pulse AF10P_W22B57 (1×10^{14} n_{eq}/cm^2).

(a) $V_{bb} = 0.0V$.   (b) $V_{bb} = -4.8V$.
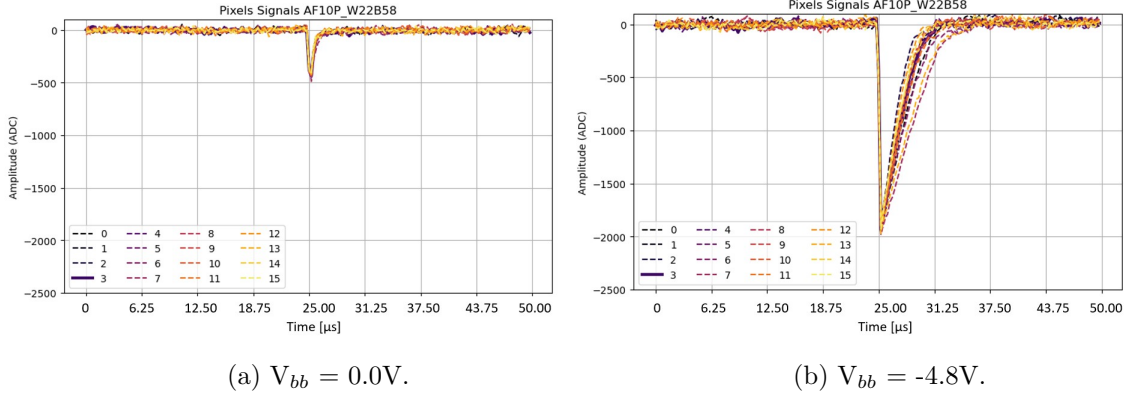
Figure 5.2: Test pulse AF10P_W22B58 (1×10^{15} n_{eq}/cm^2).

(a) $V_{bb} = 0.0V$.   (b) $V_{bb} = -4.8V$.
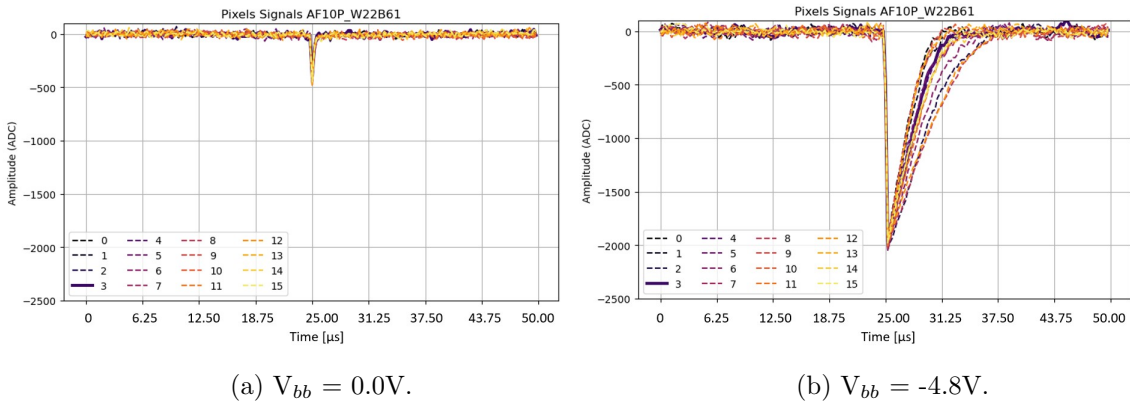
Figure 5.3: Test pulse AF10P_W22B61 (2×10^{15} n_{eq}/cm^2).

5.2 Threshold scan

Before any measurements with any kind of source, a threshold scan has to be performed in order to find a proper value for the hardware threshold (in ADC counts) to be used for the data acquisition. If the hardware threshold is too low, even noise will trigger the acquisition; if, instead, the threshold is too high, the pixel signals will not be acquired and will be lost. A global hardware threshold value that corresponds to a count rate of ≤ 1 Hz is found and properly set. The rate is calculated as the number of counts measured in 10 s. This procedure is repeated for every V_{bb} value, for every chip. In Figure 5.4, an example of the threshold scan graph is shown, with the threshold value (in ADC counts) in the x axis and the trigger rate (in Hz) in the y axis. A threshold at 170 ADC counts ($\sim$6.5mV) corresponds to a trigger rate ≤ 1 Hz as requested, as can be seen in the plot on the right, which is a zooming in the interesting portion of the plot.
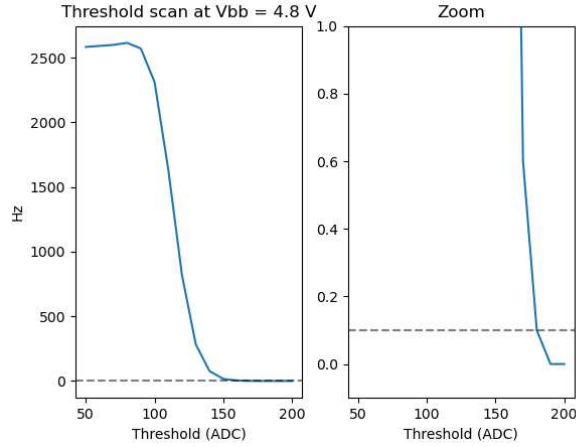
Figure 5.4: Threshold scan graph for the chip AF10P_W22B58 (1×10^{15} n_{eq}/cm^2) at V_{bb}=-4.8V to check what hardware threshold value in ADC (1 ADC = $38\mu V$) corresponds to a count rate $\leq$ 1 Hz: in this particular case the value of 170 ADC ($\sim$ 6.5 mV) was chosen.

5.3   Gain

To ensure a good signal detection and amplification, the input of front-end circuitry in the pixel has to be set to a proper voltage. This is done by applying an appropriate voltage value at the reset transistor M0 (see Figure 4.3), so that the working point of the pixel will lie within its linear range. Before the data acquisition, the gain must be checked, to ensure that the conditions at the working point are well known for each pixel. In general, in the source follower (SF) configuration, the gain g is expected to be $\lesssim 1$ and the output voltage is expected to be proportional to the input voltage ($V_{out} = gV_{in}$). For the tested chips, the gain is checked by measuring the baseline value $V_{baseline}$ (i.e. the output voltage), changing the reset voltage V_{reset} (i.e. the input voltage) from 20 mV to 900 mV, with a step of 10 mV: the result should be $V_{baseline} = gV_{reset}$. An example of this measurement is shown in Figure 5.5: on the left, the baseline value grows linearly with the reset voltage, and on the right, the gain (calculated as the derivative of $V_{baseline} = gV_{reset}$ with respect to V_{reset}) is $\sim$ 0.6-0.7. Hence, it is safe to say that operating with $V_{reset} = 500$ mV, the output signal of each pixel is linearly proportional to the signal measured as a particle crosses the detector.
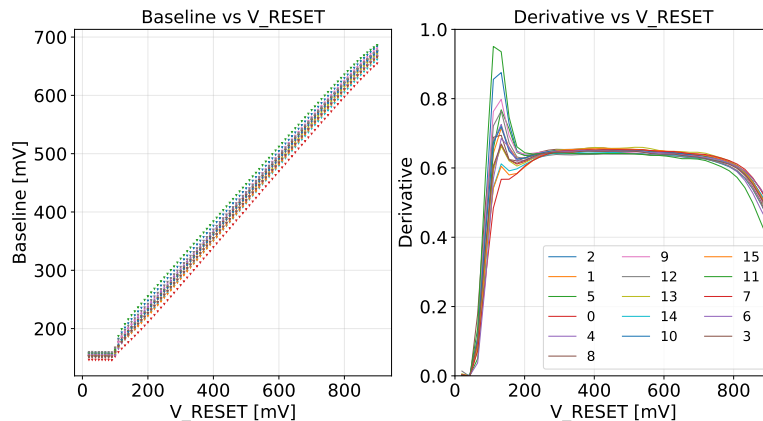
Figure 5.5: Gain control plot for each pixel for AF10P_W22B57 (1×10^{14} n_{eq}/cm^2) at V_{bb} = -4.8 V.

5.4   Radioactive source measurements

Measurements with radioactive sources, ^{55}Fe and ^{90}Sr, have been performed to characterise the available APTS test structures:

- The ^{55}Fe is essentially a source of monochromatic X-rays; it emits X-rays when it decays via K-electron capture to the ground state of ^{55}Mn[1]. An electron from an higher shell fills the vacancy in the K shell and the energy difference is released through the emission of Auger electrons or X-rays (respectively 60% and 28% of all decays). The energies of the $K_{\alpha1}$ and $K_{\alpha2}$ X-rays are so close that usually they are detected as monoenergetic (5.9 keV photons). There are also K_{β} X-rays with energy of 6.5 keV [44]. This source is typically used for calibration purposes, i.e. it allow the conversion of voltage measurements into number of electrons created. The conversion factor can be calculated knowing that on average it takes 3.6 eV to produce an electron/hole pair in Si.

- The ^{90}Sr source is used as a source of electrons; it decays by β^- emission to the ground state of ^{90}Y with a decay energy of 0.546 MeV. The beta spectrum (the distribution of energy values of the beta particles), is continuous as the decay energy is divided into three bodies: electron, antineutrino, and the recoiling ^{90}Y nuclide. The highest energy electrons are energetic enough to produce signals in the devices under test that are a good approximation to those of minimum ionising particles (MIP); these are typically selected by requiring a trigger signal in a scintillator placed behind the device under test. The study of the response of the sensor to electrons emitted by a ^{90}Sr source provides information about the charge collection performance of the device.

The results of the analysis performed on the data acquired with these sources are shown in chapter 6.

5.4.1   Source acquisition

After the gain acquisition, a radioactive source is put on the chip and the acquisition is started. The data is saved in raw files, which must be calibrated and analysed in order to get the signal distributions and other results (see chapter 6 for analysed data).

In the data analysis, only the 4 central pixels of the 4×4 matrix are possible *seed pixels*, i.e. pixels that measure a signal above the noise threshold and collect more charge with respect to nearby pixels that make up the cluster. The rest of the pixels are not considered as possible *seed pixels* because of their position: if the position of a *seed* is at the edges of the matrix, then the cluster reconstruction would be incomplete and part of the signal would be lost.

An example of the hit map of the 4×4 matrix is shown in Figure 5.6. The hit map on the left represents the number of hits registered by each pixel, each hit corresponding to a measured signal above a threshold value of 10 mV. The seed hit map on the right represents the number of hits registered by each pixel that measured a signal with a value equal to the maximum value measured in the matrix.

---

[1]Electron capture is a process wherein a proton-rich nucleus of an atom absorbs an inner atomic electron, usually from the K or L electron shells whereby a proton changes to a neutron with the simultaneous emission of an electron neutrino.
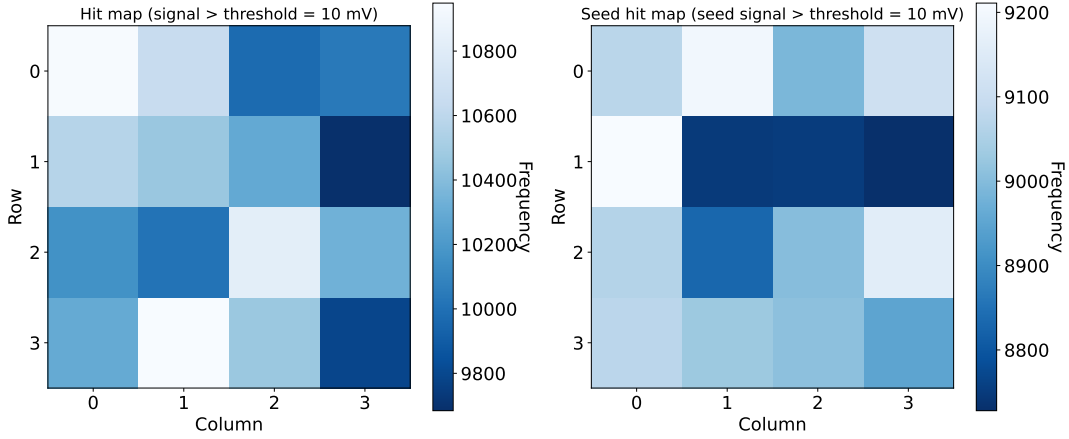
Figure 5.6: Hit map of the AF10P_W22B63 (5×10^{15} n_{eq}/cm^2) chip at $V_{bb} = 0.0V$.

5.5 Leakage current

Similarly to the test pulse (see section 5.1), for the leakage current test a pulse is injected in the capacitor put in parallel with the pixel input, changing the reset current I_{reset} from 20 pA to 140 pA, with a step of 20 pA, for all reverse bias voltage values. The I_{reset} is one of the bias currents provided to the pixel in order to set its working point; the lower the current, the lower the power consumption but the slower the pixel response. The total I_{reset} current is set by software and is supplied to the carrier board by the proximity; it is divided between all the pixels through circuitry, so that each of them receives a current value of the order of nA.

A preliminary measurement (Figure 5.7) of the I_{reset} was performed to ensure that the current supplied in μA corresponded to the current value set by software in μA. This current (and all the other bias currents and voltages) can be accessed and measured through a breakout board, inserted between the carrier and the proximity board.
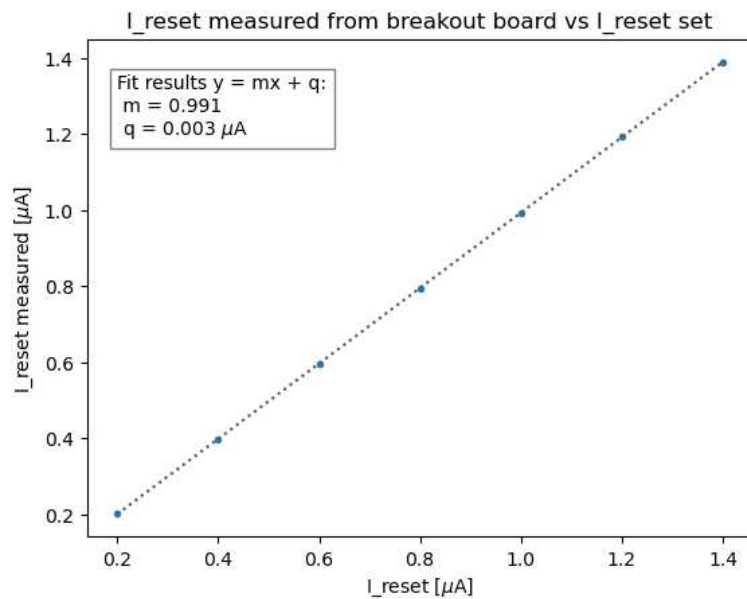
Figure 5.7: I_{reset} measured using the breakout board as a function of the I_{reset} value set by software: it is evident that the two values are almost the same. Therefore, the reset current set by software is supplied to the chip without any current loss.

The leakage current I_{leak} is obtained from the fit of the effective current I_{eff}, which in turn is obtained from the fit of the output voltage $V(t)$ of each pixel. To begin with, the current can be expressed as follows:

$$I = I_{eff} \cdot (1 - e^{-V(t)/V_{th}}) \tag{5.1}$$

where $V(t)$ is the output voltage measured from each pixel, $V_{th} = nk_BT/q$, n=1.4, k_B is the Boltzmann constant, T is the temperature in K, q is the elementary charge, and I_{eff} is obtained from the fit of $V(t)$, using the following function (obtained solving $dV = \frac{I}{C}dt$):

$$V(t) = -V_{th} \cdot \ln\left[\exp\left(\frac{I_{eff} \cdot (t - t_0)}{V_{th} \cdot C}\right) + 1\right] \tag{5.2}$$

where t_0 is the initial time, C is the chip capacitance, and t and I_{eff} are the parameters obtained from the fit.

The fit performed for the chip AF10P_W22B57 (1×10^{14} n_{eq}/cm^2), at V_{bb}=-4.8V, is shown in Figure 5.8: the three curves in each plot correspond to the pixels that measured the minimum, the average and the maximum effective current, in a time window of 20 μs ($\sim$5μs before and $\sim$15μs after the pulse). It is possible to see that for I_{reset}=20 pA, the response of the pixel is slower (see Figure 5.8a) than for I_{reset}=140 pA (see Figure 5.8b). The fit is performed in a time interval that goes from 6 μs to 17.5 μs. For both reset current values, the fit is successful; however it was observed for all chips that for $|V_{bb}| < 4.8$V and $I_{reset} < 60$ pA, the fit is not always good, therefore some data points are not considered to extrapolate the I_{leak} with the procedure shown below.

(a) I_{reset}=20 pA   (b) I_{reset}=140 pA
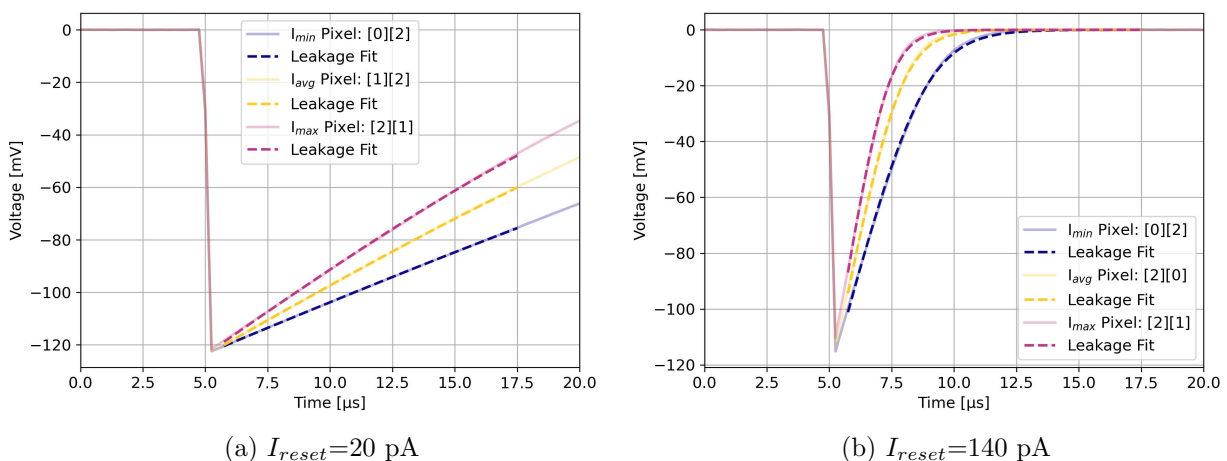
Figure 5.8: Waveform and fit for chip AF10P_W22B57 (1×10^{14} n_{eq}/cm^2), with V_{bb}=-4.8V.

From the effective current measured in each pixel changing the reset current (the values obtained from the fit presented above), it is possible to extrapolate the leakage current I_{leak}, using the following fit function on data points showed in Figure 5.9:

$$I_{eff} = m \cdot I_{reset} - I_{leak} \tag{5.3}$$
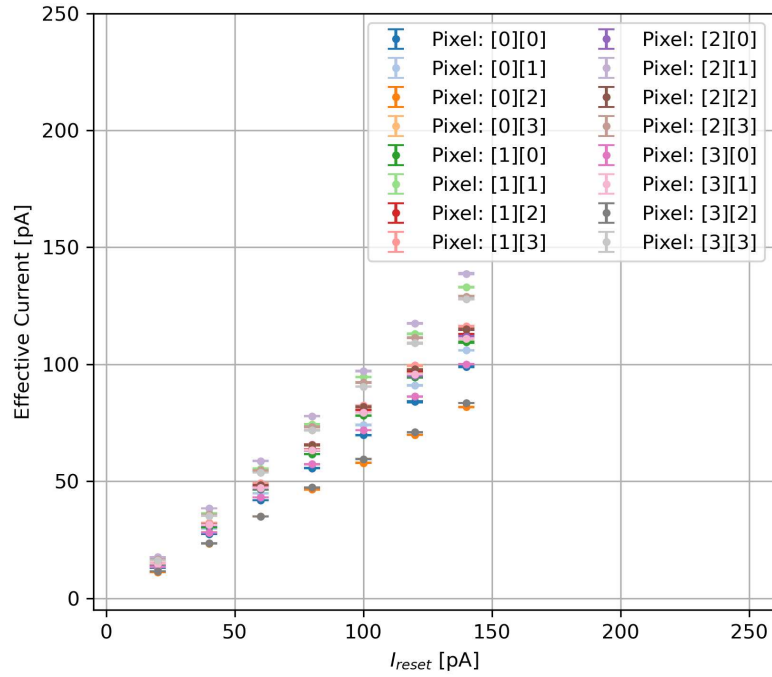
Figure 5.9: Effective current I_{eff} of all 16 pixels as a function of the reset current for chip AF10P_W22B57 (1×10^{14} n_{eq}/cm^2): the data points are obtained from the fit of the output signal of each pixel with the Equation 5.2.

The results obtained from the fits are presented and discussed in chapter 6.

Chapter 6

Results

The results of measurements using the ^{55}Fe and ^{90}Sr sources and leakage current tests are here shown and discussed.

6.1 ^{55}Fe results

6.1.1 Signal distribution

In this section, the X-ray spectra obtained with different chips and different reverse bias values are shown. The fit performed uses a bimodal function from two normal Gaussian distributions. The parameters obtained from the fit of the data acquired with the ^{55}Fe source - i.e. the centroids and the standard deviations of the two gaussians - are used for the calibration in all the following analysis. The mean of the main Gaussian population coincides with the 5.9 keV peak (the *charge collection peak*) and corresponds to ~1640 electron/hole pairs released inside the active volume of the sensor; the mean of the smaller gaussian coincides with the 6.4 keV peak and corresponds to ~1800 electron/hole pairs. A clear separation between the two characteristic peaks shows low pixel noise and good energy resolution. In Figure 6.1 the distributions of the seed values for the the AF10P_W22B25 (not irradiated) and AF10P_W22B57 (1×10^{14} n_{eq}/cm^2) at V_{bb} = -4.8 V are shown.
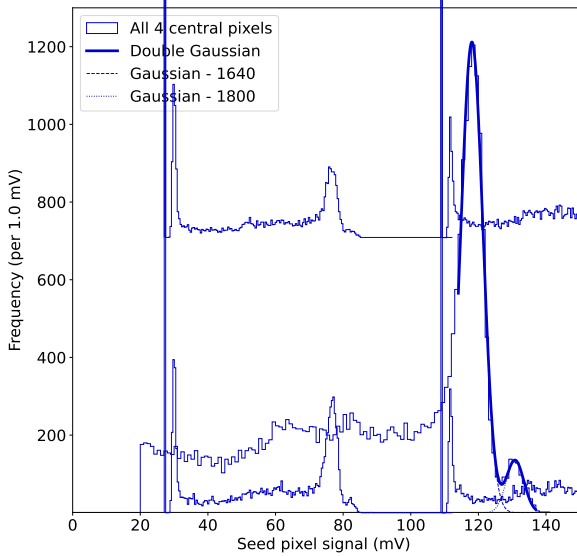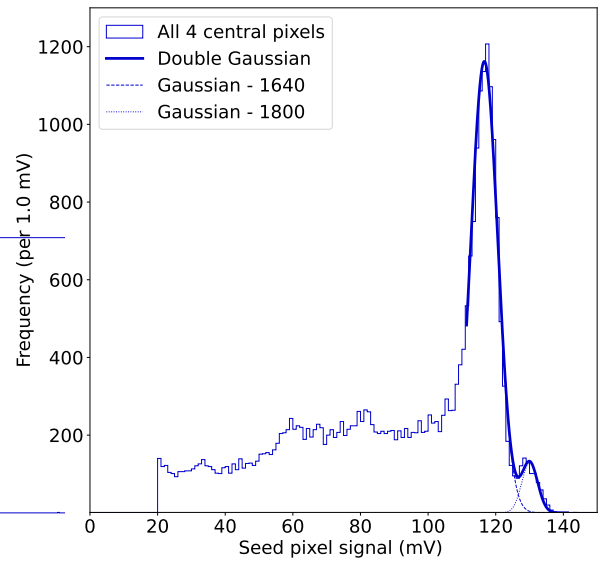
(a) AF10P_W22B25 (not irradiated)   (b) AF10P_W22B57 (1×10^{14} n_{eq}/cm^2)

Figure 6.1: Distribution of the seed signal amplitude from 4 central pixels (2×2 matrix) at V_{bb} =-4.8V.

6.1.2 Calibration

The output signal of each pixel is measured in ADC (1 ADC = 38 μV). However, it is useful to convert the pixel signal in collected charge (electrons) because the signal measured in this way is decoupled from the input capacitance, which changes with the reverse bias voltage applied and with the collection diode geometry [45]. Hence, this calibration allows the direct comparison of the charge collection properties for different reverse bias voltages. The means of the two Gaussian peaks (5.9 keV and 6.4 keV) obtained from the fit of the data acquired with the ^{55}Fe source (see subsection 6.1.1) are used to convert the signal measured in mV to numbers of electrons. The conversion is obtained as follows:

$$\text{signal } [e^-] = \text{signal } [mV] \times 1640[e^-]/\text{mean main Gaussian } [mV] \tag{6.1}$$

This charge calibration is used in the analysis of data obtained with the ^{55}Fe source and the ^{90}Sr source (see section 6.2) for the conversion of the signal from mV to electrons.

The calibration plot for the non-irradiated chip with a 15 μm pixel pitch is shown in Figure 6.2a; the calibration plot for the non-irradiated chip with a 10 μm pixel pitch is shown in Figure 6.2b; the calibration plot for the AF10P_W22B57 chip is shown in Figure 6.2c (1×10^{14} n_{eq}/cm^2). For a given V_{bb} value, the calibration curves do not depend appreciably on neutron fluence, nor on pixel pitch (see Table 6.1). All the plots show a good linearity between the input charge and the output voltage signal.

(a) AF15P_W22B23 (not irradiated)   (b) AF10P_W22B25 (not irradiated)

(c) AF10P_W22B57 (1×10^{14} n_{eq}/cm^2)
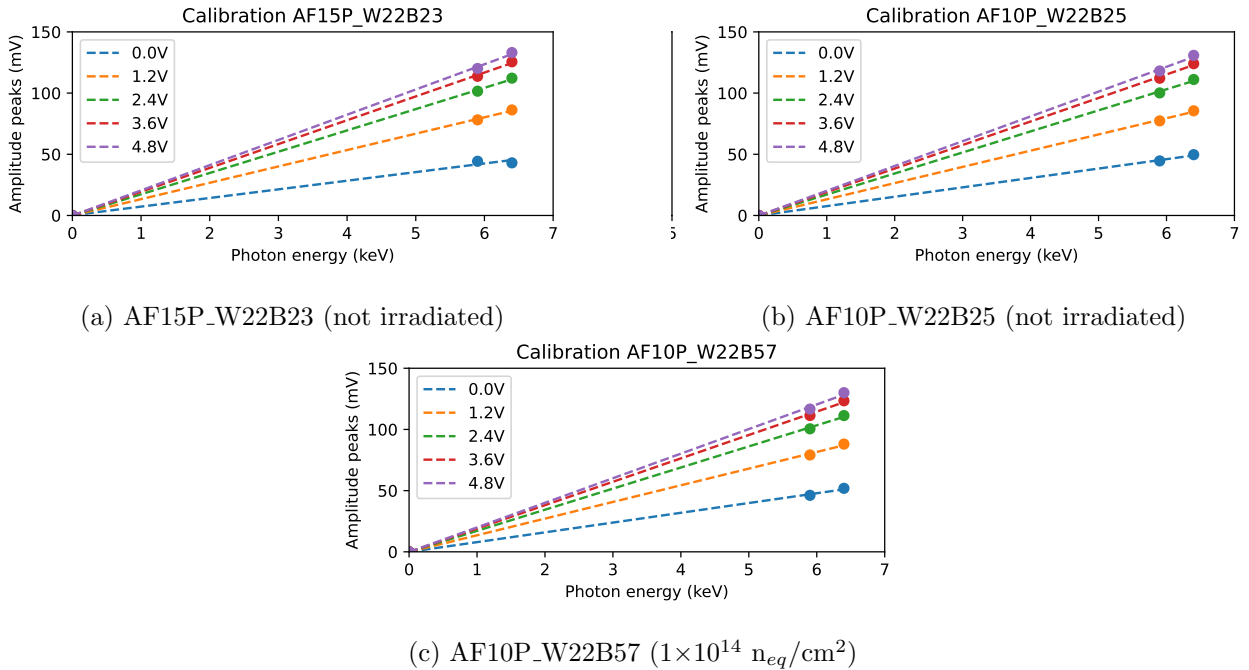
Figure 6.2: Calibration using the data points obtained from the fit performed for the spectra acquired during the measurements with the ^{55}Fe source.

Table 6.1: Fit parameters from the calibration plot showed in Figure 6.2.

V_{bb} [V]	AF15P_W22B23 slope [mV/keV]	AF10P_W22B25 slope [mV/keV]	AF10P_W22B57 slope [mV/keV]
0.0	7.05	7.68	7.99
-1.2	13.38	13.25	13.61
-2.4	17.40	17.20	17.24
-3.6	19.47	19.22	19.11
-4.8	20.62	20.26	20.09

6.1.3 Cluster size

Another parameter of interest is the cluster size, i.e. the number of pixels on which the charge generated by each event is collected. The cluster size might depend both on the X-ray conversion position (in the middle of a pixel, in between two pixels, on the corner among four pixels, etc) and on the charge collection mechanism (either by drift or by diffusion). Also radiation-induced damage might affect the cluster size. Taking into account the trapping effect caused by non-ionizing irradiation, a cluster size decrease is expected: less charge is collected because some charges get trapped, so that the pixel signal might fall below threshold. For all the chips tested (regardless of the neutron fluence and of the pixel pitch) and in most (>90%) of events, the cluster size is 1, which means that the charge is collected in a short period of time by the seed pixel[1], which carries almost the whole cluster energy. In Figure 6.3 the cluster size distributions are shown for the non irradiated chip and all the four irradiated chips. Comparing Figure 6.3b and Figure 6.3e, it is possible to see a lower relative frequency of the cluster size of 2 for the chip exposed to the highest irradiation level. However, the cluster size distribution does not change noticeably increasing the irradiation level.

(a) AF10P_W22B25 (not irradiated)

(b) AF10P_W22B57 (1×10^{14} n_{eq}/cm^2)

(c) AF10P_W22B58 (1×10^{15} n_{eq}/cm^2)

(d) AF10P_W22B61 (2×10^{15} n_{eq}/cm^2)

(e) AF10P_W22B63 (5×10^{15} n_{eq}/cm^2)
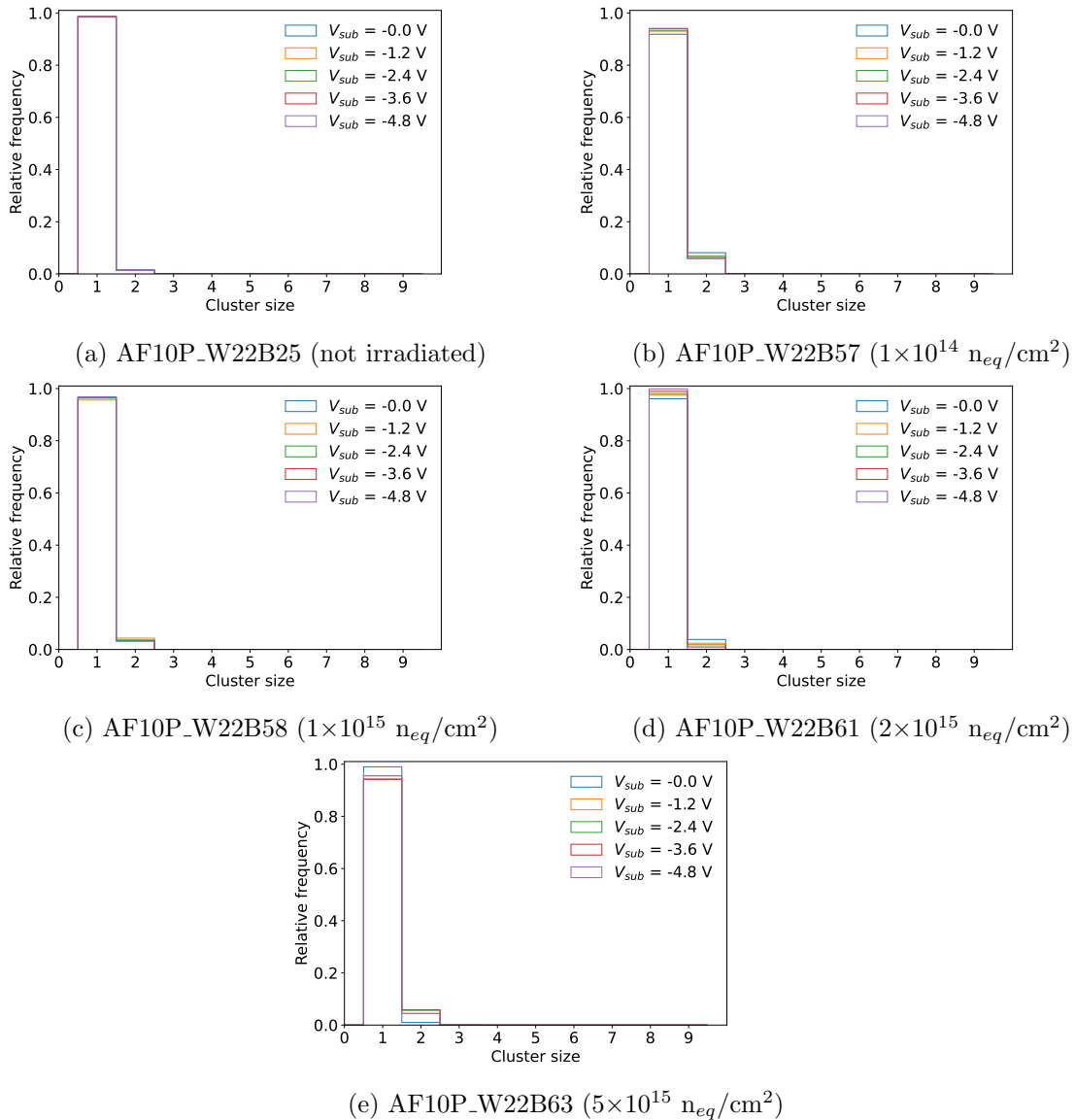
Figure 6.3: Cluster size comparison with the ^{55}Fe source.

---

[1]The pixel that measures a signal above the noise threshold and collects more charges with respect to nearby pixels, for more details see subsection 5.4.1.

6.1.4   Noise and baseline

The noise and the baseline of each pixel are measured individually. To calculate the baseline, 50 consecutive output pixel signals are measured (without any source). The distribution of these signals is Gaussian, and the baseline value is the mean value. The noise is calculated as the RMS of the baseline distribution and, using the charge calibration showed in subsection 6.1.2, the noise in mV is converted in electrons. In Figure 6.4 the noise distributions for each pixel of the chip AF10P_W22B25 (not irradiated) for all V_{bb} values: at 0.0 V, the noise value is $\sim 35\ e^-$, and it decreases as the depleted region increases, until it reaches a value of $\sim 25\ e^-$ with $V_{bb} = $ -4.8 V. In Figure 6.5 are shown the noise distributions for all irradiated chip for $V_{bb} = $ -4.8 V. The noise values for all the irradiated chips are summarised in Table 6.2: at V_{bb}=0.0V the noise increases with the irradiation level; however, for V_{bb}=-4.8V the noise values reach $\sim 25\ e^-$ in all cases, except for the chip exposed to the highest irradiation level, in this case the noise is $\sim 35\ e^-$. It was observed that the noise distribution of the chip exposed to a fluence of $1{\times}10^{14}\ n_{eq}/cm^2$ is similar to the non irradiated chip for all V_{bb} values.

Table 6.2: Noise values for all the irradiated chips, for V_{bb}=0.0V and V_{bb}=-4.8V.

	Noise AF10P_W22B57 ($1{\times}10^{14}\ n_{eq}/cm^2$)	Noise AF10P_W22B58 ($1{\times}10^{15}\ n_{eq}/cm^2$)	Noise AF10P_W22B61 ($2{\times}10^{15}\ n_{eq}/cm^2$)	Noise AF10P_W22B63 ($5{\times}10^{15}\ n_{eq}/cm^2$)
V_{bb}=0.0V	$\sim 35\ e^-$	$\sim 40\ e^-$	$\sim 45\ e^-$	$\sim 70\ e^-$
V_{bb}=-4.8V	$\sim 25\ e^-$	$\sim 25\ e^-$	$\sim 25\ e^-$	$\sim 35\ e^-$

(a) $V_{bb} = 0.0$ V

(b) $V_{bb} = $ -1.2 V

(c) $V_{bb} = $ -2.4 V

(d) $V_{bb} = $ -3.6 V
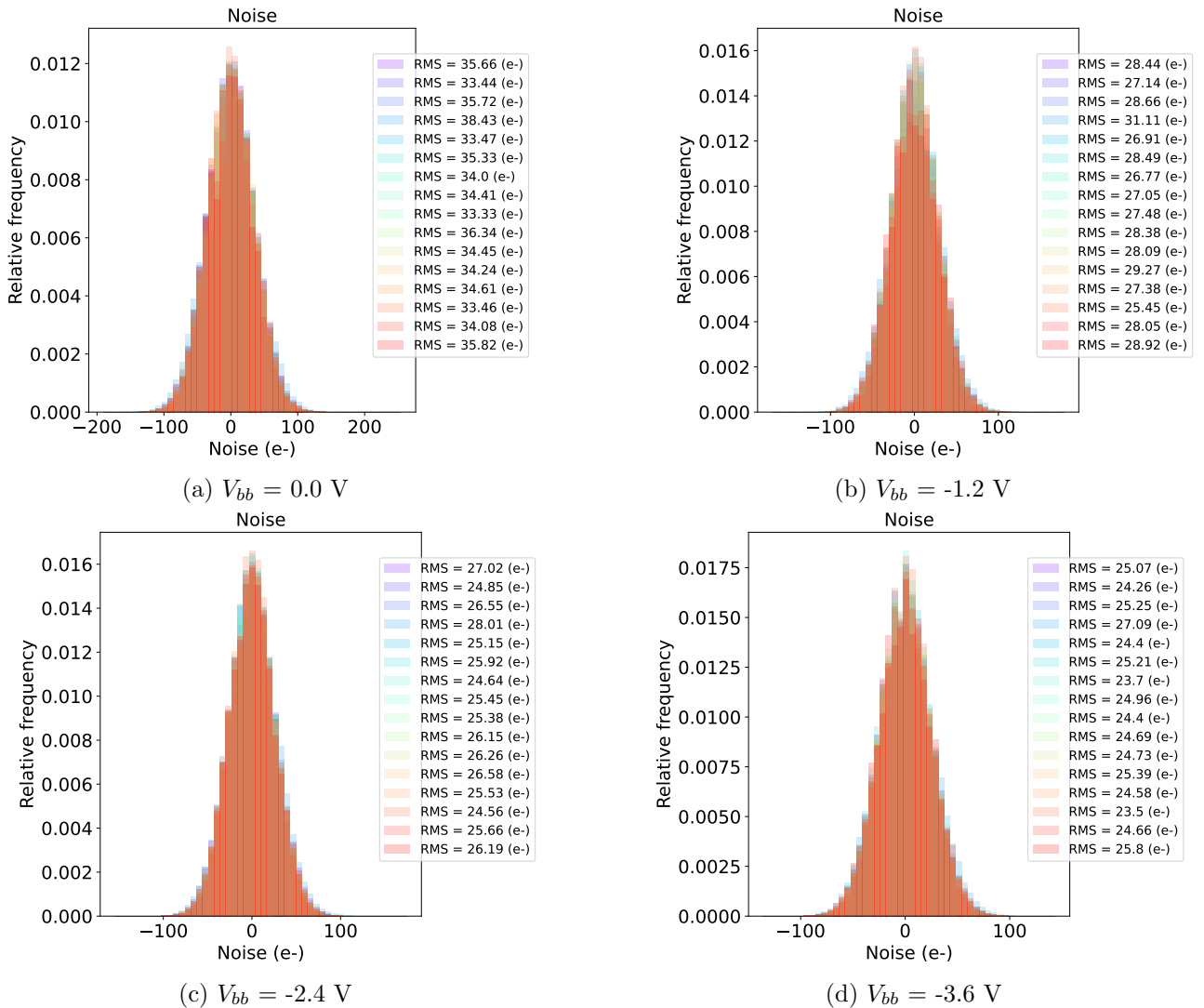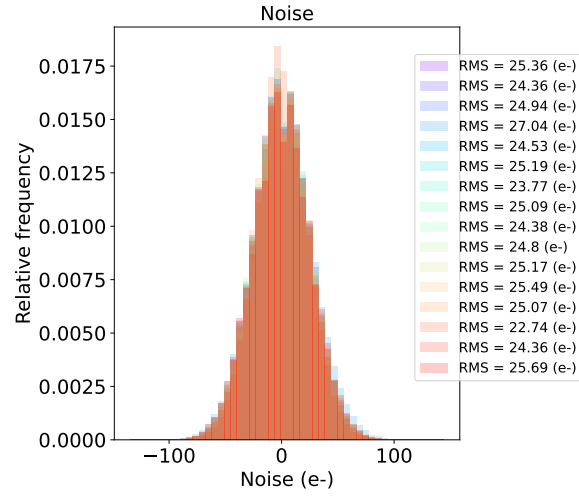
(e) V_{bb} = - 4.8 V

Figure 6.4: Noise distribution, chip AF10P_W22B25 (not irradiated).
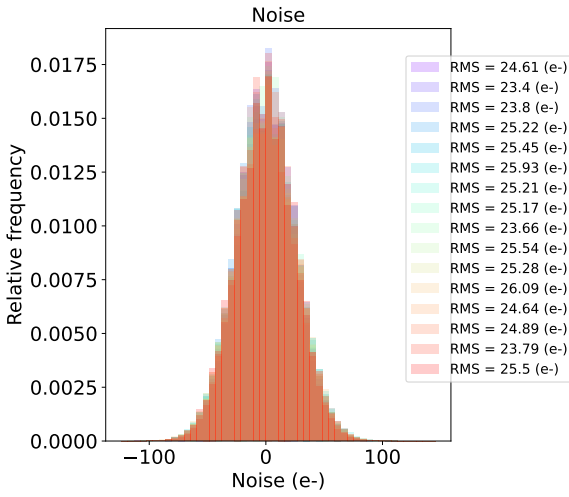
(a) AF10P_W22B57 (1×10^{14} n$_{eq}$/cm^2)
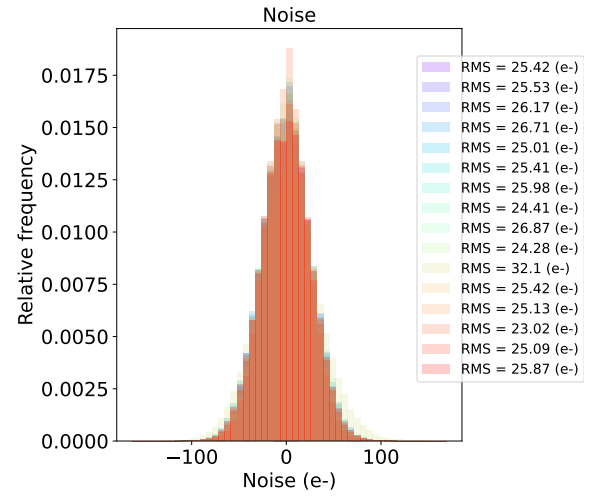
(b) AF10P_W22B58 (1×10^{15} n$_{eq}$/cm^2)
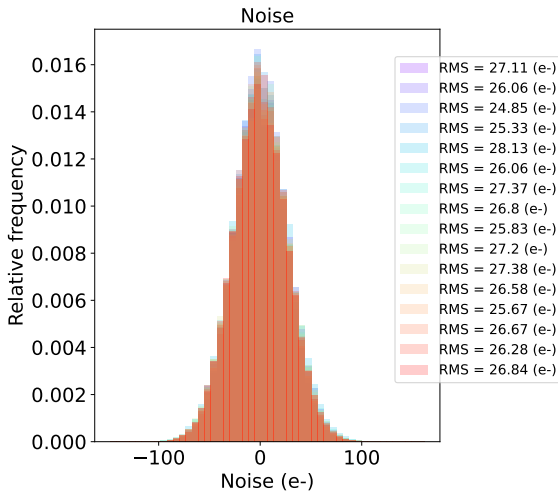
(c) AF10P_W22B61 (2×10^{15} n$_{eq}$/cm^2)
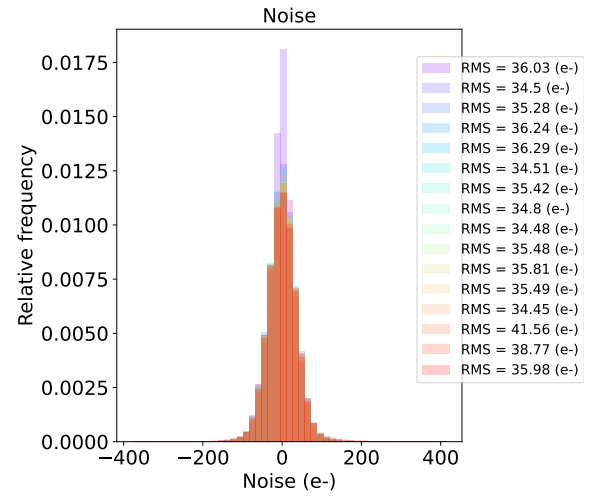
(d) AF10P_W22B63 (5×10^{15} n$_{eq}$/cm^2)

Figure 6.5: Noise distribution for all irradiated chips, V_{bb} = -4.8 V.

6.1.5   Charge sharing

Charge sharing can affect the spatial resolution of the detector. The version of the APTS tested was in fact optimized to reduce charge sharing. For each event, recalling the definition of cluster, a part of the charge is collected by the seed pixel, the remaining is detected by the surrounding pixels (neighbouring). When charge sharing is small, most of the total charge is collected by the seed, and only a small fraction by the neighbouring pixels.

The plots below are 2D histograms showing the amount of charge collected by neighbouring pixels versus the charge collected by the seed pixel. If charge sharing is small, the charge collected by neighbouring pixels is ≈ 0 mV.

Figure 6.6 shows the effect of charge sharing for the non-irradiated chip (10 μm pixel pitch) for all V_{bb} values; Figure 6.7 shows the effect for the chips after irradiation for V_{bb} = -4.8 V. Figure 6.8 shows the effect of charge sharing for the non irradiated chip (15 μm pixel pitch) for V_{bb} = -4.8 V.

As can be seen in Figure 6.6, there is no evident charge sharing in the non-irradiated chip for $|V_{bb}| > 0$: indeed, the charge is collected mainly by the seed pixel, i.e. the cluster size is equal to 1 (this is in line with the cluster size distribution showed in subsection 6.1.3), and in correspondence of the *charge collection peak*, the sum of neighbouring signals does not give a significant contribution, i.e. the values are around 0 V. Therefore, the increased lateral field generated by the gap in the low dose n-type implant actually reduces the charge sharing and concentrates the signal charge on a single pixel.

For irradiation levels of 1×10^{14} n$_{eq}$/cm^2 and 1×10^{15} n$_{eq}$/cm^2, shown in Figure 6.7a and Figure 6.7b, respectively, the charge sharing effect is not visible.

For higher neutron fluences, however, charge sharing is more evident (for all V$_{bb}$ values, here only shown for -4.8V in Figure 6.7c and Figure 6.7d). Two peaks are clearly distinguishable: the *charge collection peak*, visible in the higher part of the spectrum, and the *charge sharing peak*, visible in the lower part of the spectrum. In Figure 6.7d it is possible to see two clearly distinguished regions.

(a) V_{bb} = 0.0 V   (b) V_{bb} = -1.2 V

(c) V_{bb} = -2.4 V

(d) V_{bb} = -3.6 V
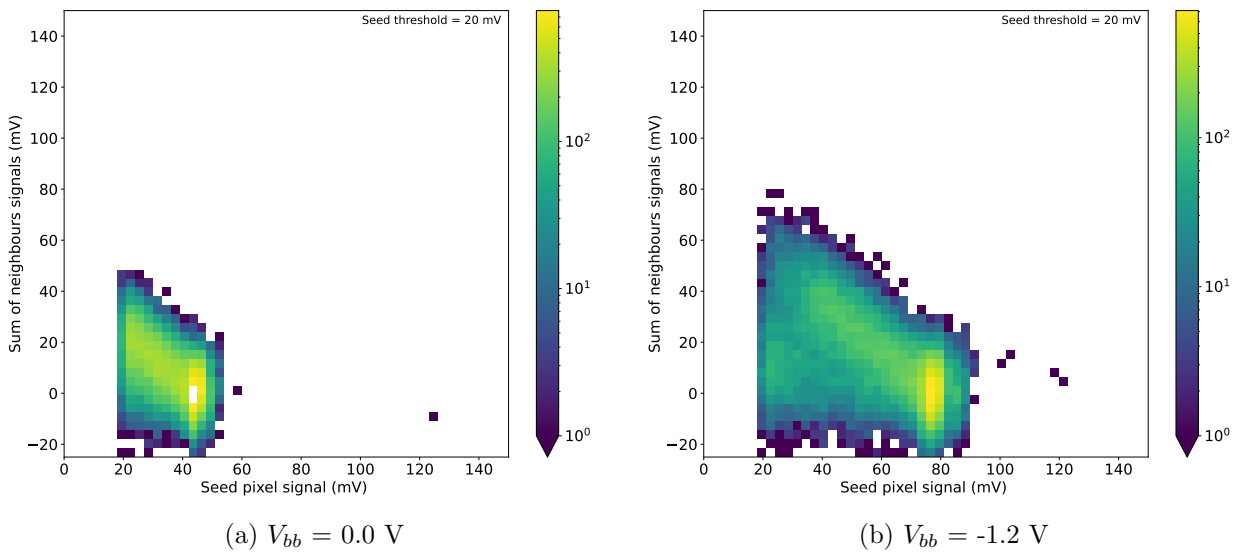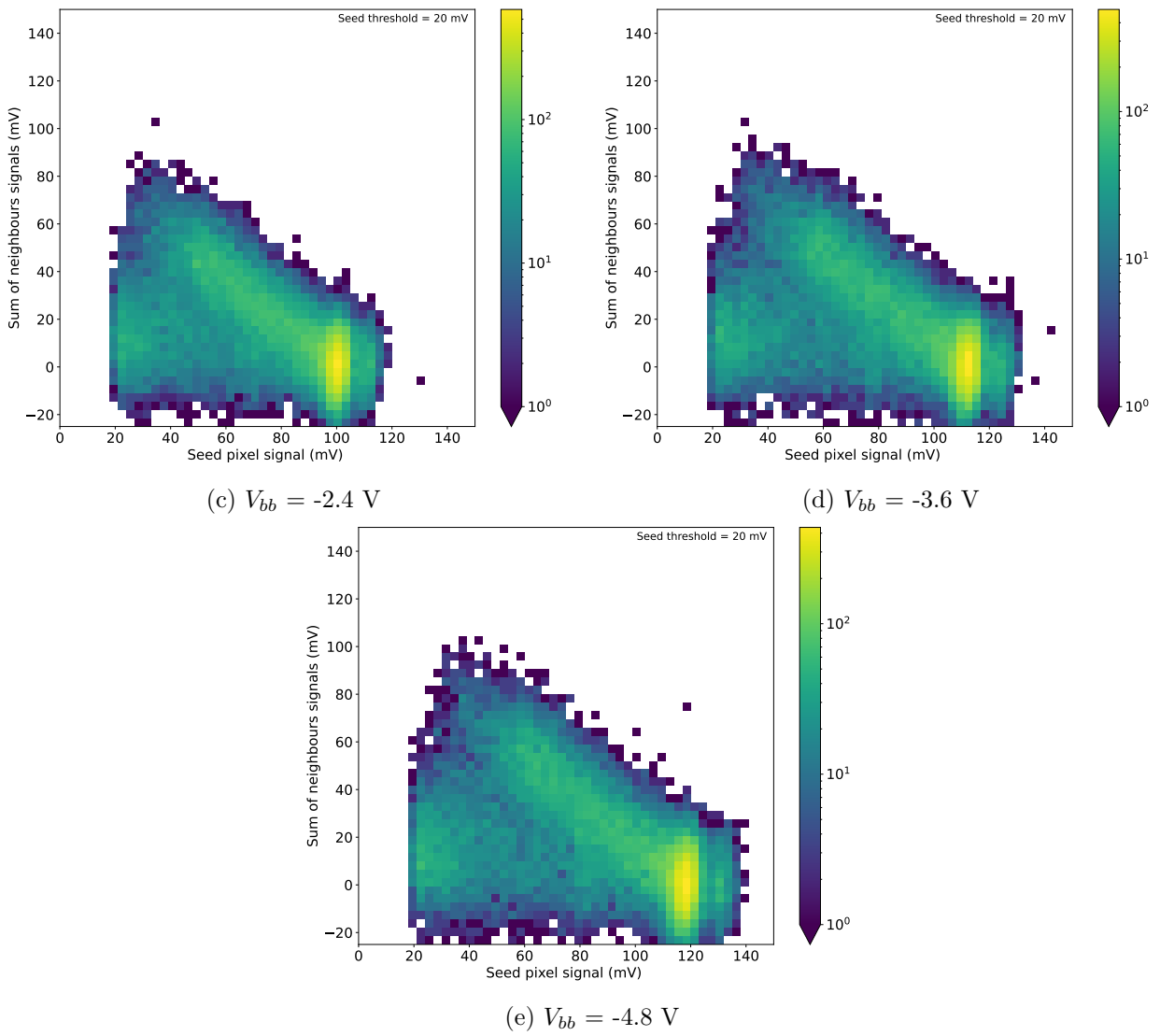
(e) V_{bb} = -4.8 V

Figure 6.6: Sum of neighbouring pixels for chip AF10P_W22B25 (not irradiated) for all V_{bb} values.

(a) AF10P_W22B57 (1×10^{14} n_{eq}/cm^2)

(b) AF10P_W22B58 (1×10^{15} n_{eq}/cm^2)

(c) AF10P_W22B61 (2×10^{15} n_{eq}/cm^2)   (d) AF10P_W22B63 (5×10^{15} n_{eq}/cm^2)
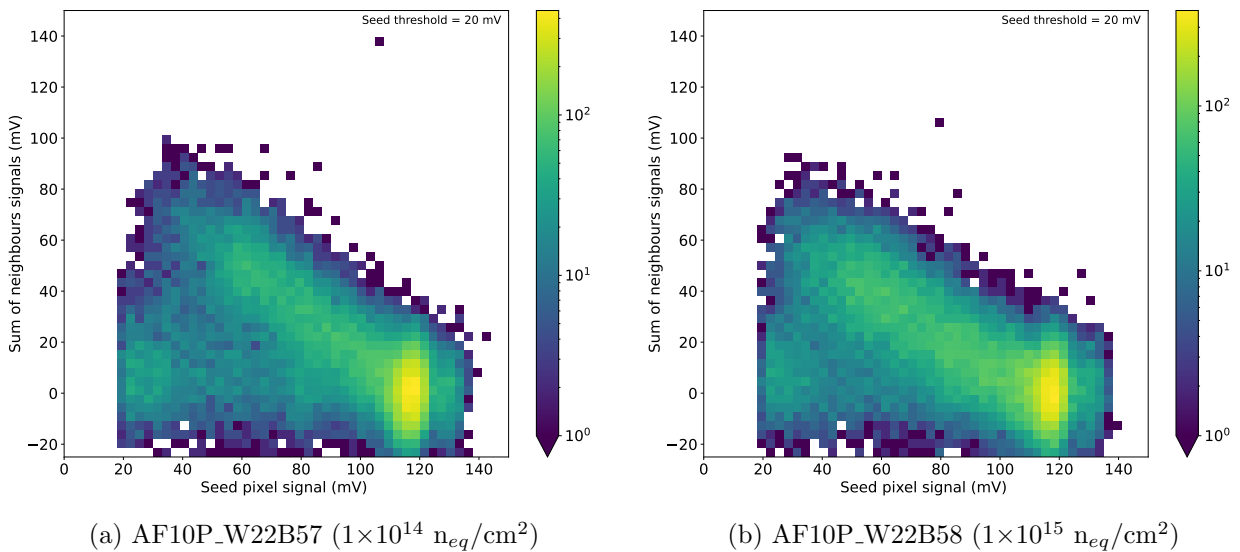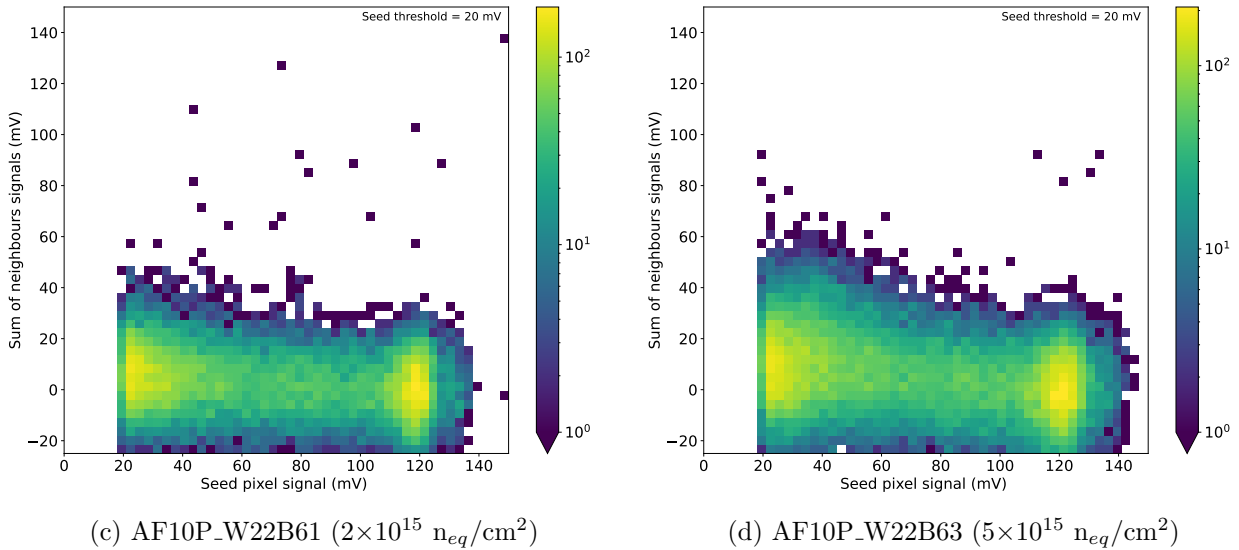
Figure 6.7: Sum of neighbouring pixels at V_{bb} = - 4.8 V.

Figure 6.8 shows that there is no evident charge sharing effect for the chip with a pixel pitch of 15 μm (non irradiated), and comparing this 2D histogram to the one showed in Figure 6.6e that corresponds to the chip with a pixel pitch of 10 μm (non irradiated), it is possible to say that there is no significant difference between the two pixel pitches.
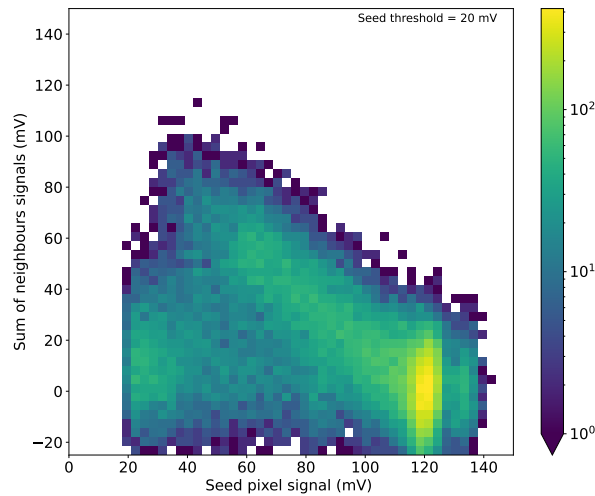
Figure 6.8: Sum of neighbouring pixels for chip AF15P_W22B23 (not irradiated) for all V_{bb} values.

6.1.6 Comparisons: non-irradiated vs irradiated

The following quantities are extracted from the ^{55}Fe measurements: *seed signal, capacitance, noise, charge collection efficiency* and *mean cluster size*. They are all compared before and after irradiation, for all the different neutron fluences.

- **Seed signal:** the seed signal is the output signal of the pixel which collects the largest amount of charge in the cluster. This signal increases as the reverse bias voltage increases. Indeed, when the active area is not depleted ($V_{bb} = 0.0$ V), the capacitance C is higher than when the detector is depleted ($|V_{bb}| > 0.0$ V), and knowing that the charge collected Q by the sensing diode is approximately the same, the voltage seed signal V is higher when the capacitance is smaller ($V = Q/C$). The seed value is therefore expected to increase with increasing $|V_{bb}|$ values.

- **Capacitance:** the pixel capacitance C_p is formed by the junction capacitance of the collection diode C_j and the input capacitance of the in-pixel readout circuit C_r. The pixel capacitance is charged to operational level applying a reset potential V_{reset}, then it discharges when a charge Q is collected, which leads to a voltage drop $V = Q/C_p$. The capacitance is calculated as:

$$\text{C [F]} = \frac{1640 \times 1.6 \times 10^{-19}[\text{C}]}{\mu_{Gauss}\ \text{seed [V]}} \tag{6.2}$$

  where μ_{Gauss} *seed* is the mean of the Gaussian fit performed on the seed signal distribution for the 4 central pixels. In order to have larger voltage signal, it is necessary to reduce the C_p value as low as possible [45], for instance by applying a reverse bias to the junction. The pixel capacitance C_p is therefore expected to decrease with increasing $|V_{bb}|$ values.

- **Noise:** the noise follows a Gaussian distribution and is calculated as the RMS of the baseline (see subsection 6.1.4).

- **CCE:** the charge collection efficiency (CCE) is calculated as:

$$\text{CCE [\%]} = 100 \times \frac{\mu_{Gauss}\ \text{seed}}{\mu_{Gauss}\ \text{matrix}} \tag{6.3}$$

  where μ_{Gauss} *seed* is the mean of the Gaussian fit performed on the seed signal distribution for the 4 central pixels; μ_{Gauss} *matrix* is the mean of the Gaussian fit performed on the matrix signal distribution for events corresponding to a cluster size of 1. For CCE here we mean the ratio between the charge collected by the seed and the total charge (i.e. the charge collected in the matrix) created by the ionizing radiation. Therefore, an increase of the CCE is expected for higher bias voltages for different reasons. Indeed, when the detector is depleted, the charge is collected by drift (and not by diffusion) and in a short period of time, which result in more charge collected by the seed. Moreover, for irradiated chips, the effect of the electric field inside the sensing volume of the detector is even more crucial: in fact, if the charges drift to the collection diode, the probability that they get trapped in radiation-induced trapping centres is lower, with respect to the case when the charges diffuse freely inside the volume.

- **Mean cluster size:** the mean cluster size corresponds to the average number of pixels belonging to a cluster, i.e. the pixels that collected a signal above the threshold.

For the result comparison, the data of the chip AF10P_W22B25 (not irradiated) have been used as reference for the parameters used to characterise the performance of the irradiated chips.

Figure 6.9 shows the results for the non irradiated chip with 15 μm pixel pitch; Figure 6.10 summarizes the results for the chips with 10 μm pixel pitch for all the different irradiation levels.

In Figure 6.9, it is possible to see that increasing the reverse bias voltage (i.e. increasing the depletion region) the seed signal increases from 40 mV to 120 mV and the capacitance decreases from 6 fF to $\sim$2 fF (as a consequence of the relation between charge collected Q, the capacitance C and the voltage V, which is given by $Q = CV$). The CCE is almost 100% for all V_{bb} values. The noise increases slightly from 1 mV to 1.5 mV; the mean cluster size is below 1.5 for all V_{bb} values.
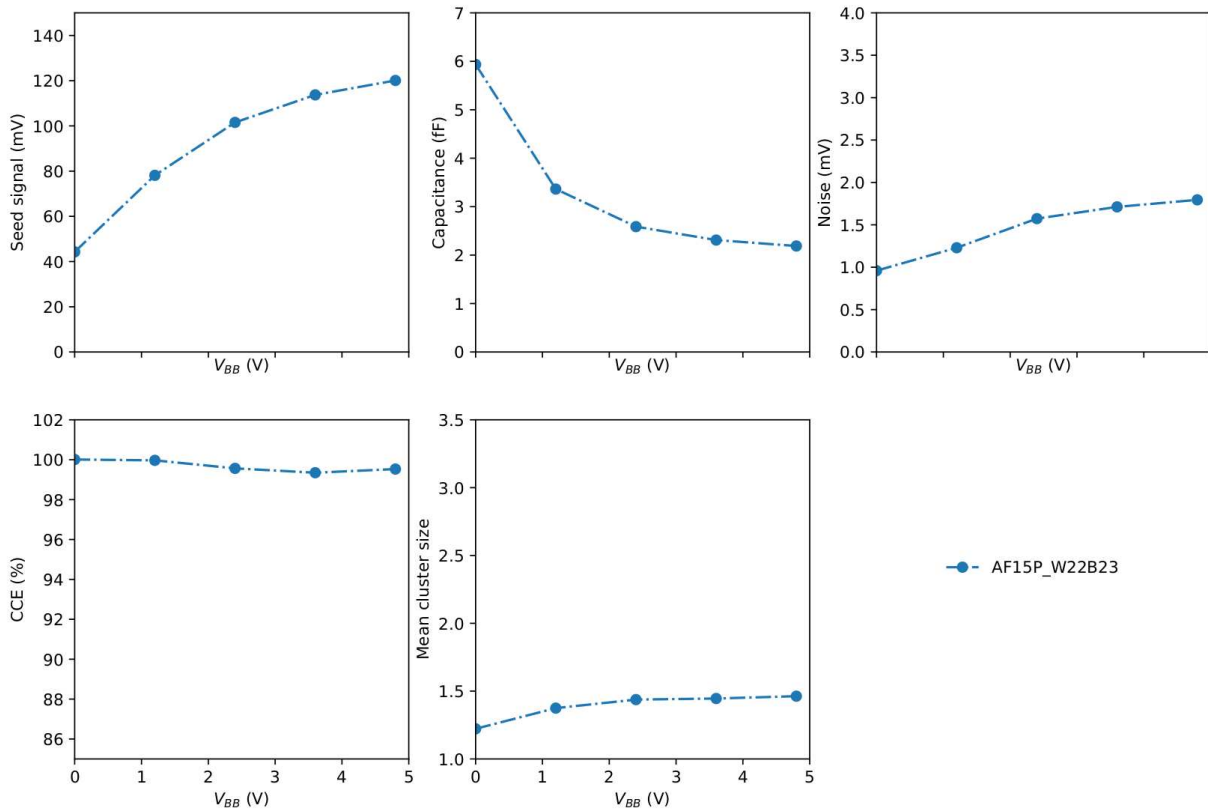
Figure 6.9: Result comparison of seed signal, capacitance, noise, CCE and mean cluster size for AF15P_W22B23 (pitch = 15μm, not irradiated) at different V_{bb} values.

The result comparison between irradiated chips (see Figure 6.10) shows that for the lowest irradiation level (10^{14} 1-MeV n_{eq}/cm^2, an order of magnitude above the ITS3 radiation hardness requirement) the performance of the chip is not degraded, i.e. all the parameters studied are compatible with the non irradiated chip.

For higher irradiation levels, the seed signal distribution and the capacitance values follow the same trend of the non irradiated chip, the difference is only visible for $|V_{bb}| < 3.6$ V, where the seed signal is slightly higher (the difference is of the order of 10 mV), and the capacitance is a bit smaller (the difference is of the order of 1 fF). Regarding the noise, all the irradiated chips have a higher noise with respect to the non irradiated at 0.0 V; as the bias increases, the noise of all chips get to the same value, except for the chip exposed to 5×10^{15} n_{eq}/cm^2, which continues growing up to ~ 2.5 mV. The CCE at 0.0 V is not included in the plot, since it is not possible to extract a reasonable value using Equation 6.3. For the other V_{bb} values, the CCE for the chips exposed to the three highest irradiation levels is $\sim97\%$. The mean cluster size is < 1.4 for all irradiated chips.
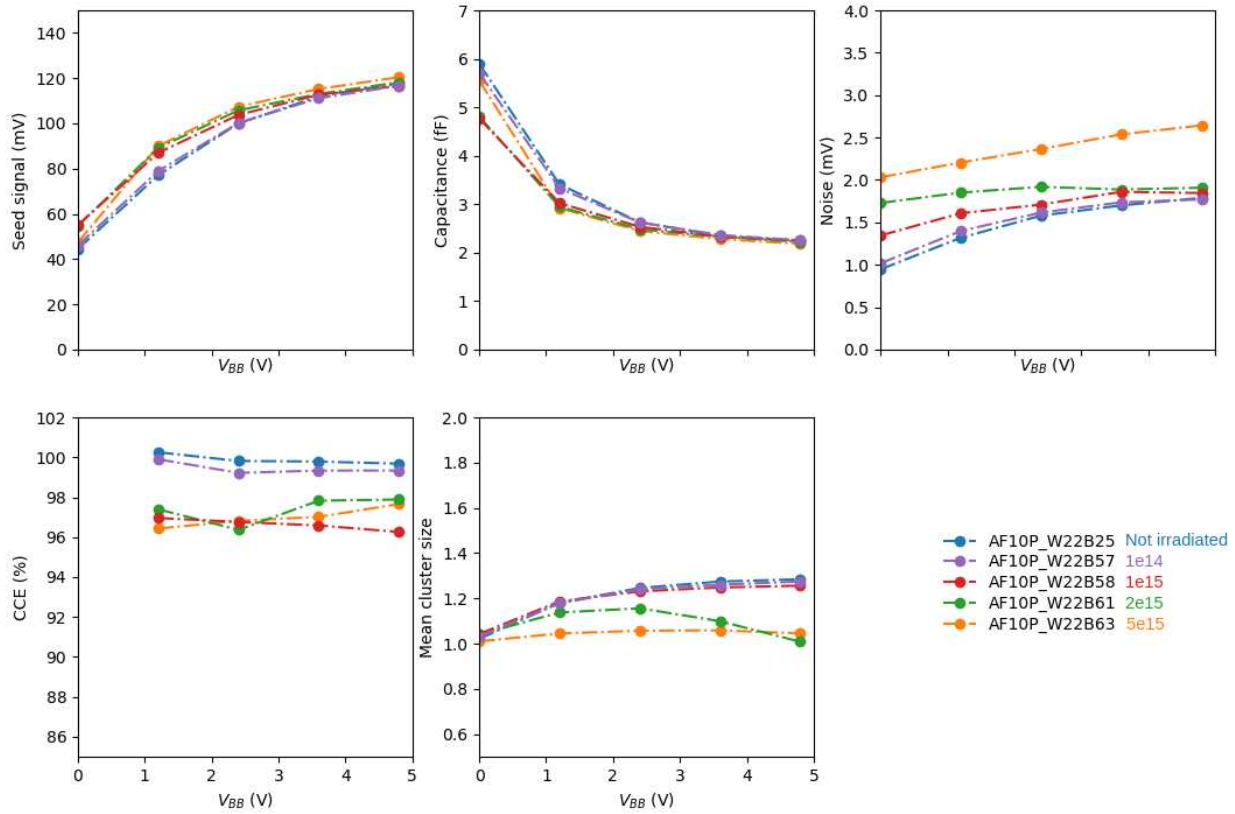
Figure 6.10: Result comparison of seed signal, capacitance, noise, CCE and mean cluster size for AF10P_W22B25 (not irradiated) and all other irradiated chips at different V_{bb} values.

In Figure 6.11, the seed and the matrix signal distributions in mV for chip AF10P_W22B25 (not irradiated) are shown for all V_{bb} values. It is possible to see that the signal amplitude shifts to higher voltage values V as the reverse bias voltage increases, because the capacitance C decreases and the charge collected Q is almost the same ($V = Q/C$). The *charge collection peak* is clearly distinguishable at all V_{bb} values.
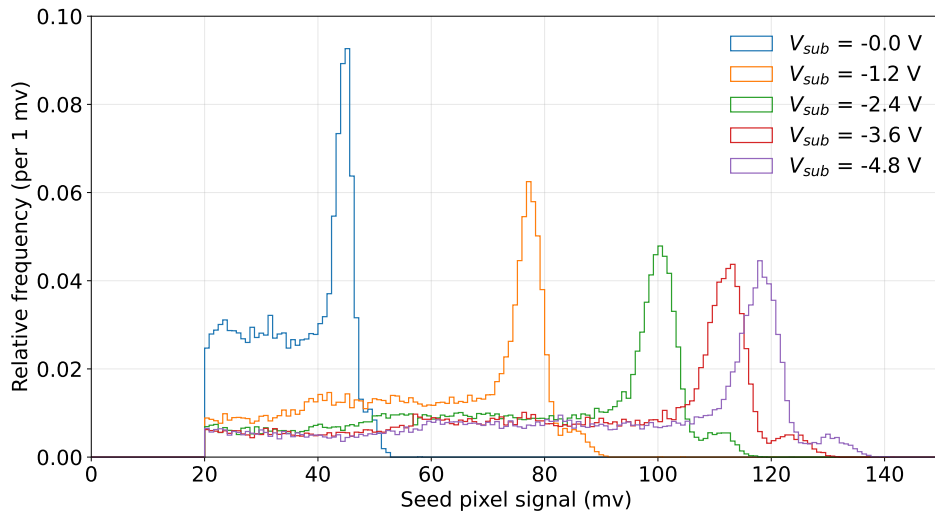
(a) AF10P_W22B25 (not irradiated)
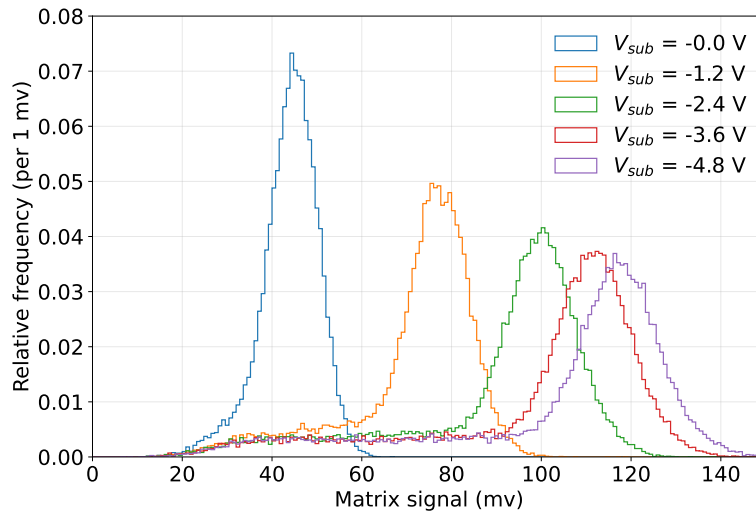
(b) AF10P_W22B25 (not irradiated)

Figure 6.11: Distribution of signal for chip AF10P_W22B25 (not irradiated).

In Figure 6.12, the seed and the matrix signal distributions in mV for chip AF10P_W22B57 (1×10^{14} n_{eq}/cm^2) are shown for all V_{bb} values. It is possible to see that the signal amplitude shifts to higher voltage values V as the reverse bias voltage increases, because the capacitance C decreases and the charge collected Q is almost the same ($V = Q/C$). The *charge collection peak* is clearly distinguishable at all V_{bb} values.
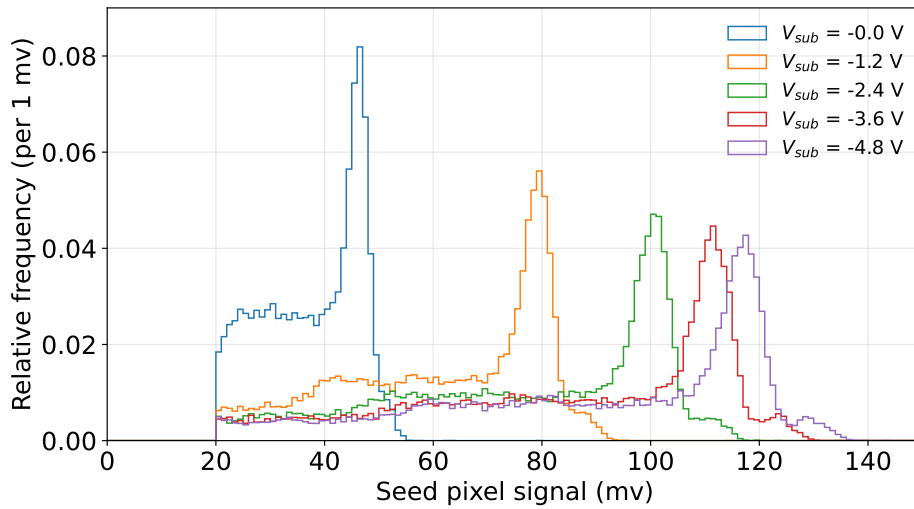
(a) AF10P_W22B57 (1×10^{14} n_{eq}/cm^2)
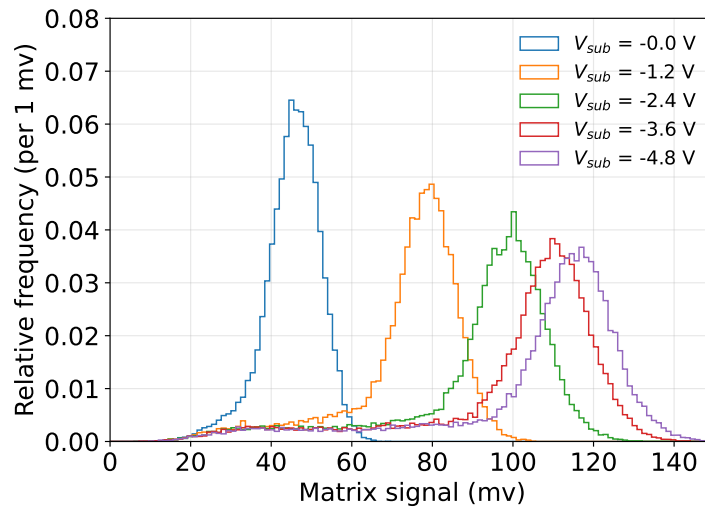
(b) AF10P_W22B57 (1×10^{14} n_{eq}/cm^2)

Figure 6.12: Distribution of signal for chip AF10P_W22B57 (1×10^{14} n_{eq}/cm^2).

In Figure 6.13, the seed and the matrix signal distributions in mV for chip AF10P_W22B58 (1×10^{15} n_{eq}/cm^2) are shown for all V_{bb} values. It is possible to see that the signal amplitude shifts to higher voltage values V as the reverse bias voltage increases, because the capacitance C decreases and the charge collected Q is almost the same ($V = Q/C$). The *charge collection peak* is clearly distinguishable for $|V_{bb}| > 0.0V$; the peaks are wider than the peaks seen in Figure 6.11 for the non irradiated chip: this is a consequence of the radiation-induced bulk damage. At this irradiation level, we see in the matrix signal distribution the *charge sharing peak* mentioned before in subsection 6.1.5.

(a) AF10P_W22B58 (1×10^{15} n_{eq}/cm^2)

(b) AF10P_W22B58 (1×10^{15} n_{eq}/cm^2)

Figure 6.13: Distribution of signal for chip AF10P_W22B58 (1×10^{15} n_{eq}/cm^2).

In Figure 6.14, the seed and the matrix signal distributions in mV for chip AF10P_W22B61 (2×10^{15} n_{eq}/cm^2) are shown for all V_{bb} values. It is possible to see that the signal amplitude shifts to higher voltage values V as the reverse bias voltage increases, because the capacitance C decreases and the charge collected Q is almost the same ($V = Q/C$). The *charge collection peak* is clearly distinguishable for $|V_{bb}| >0.0$V; the peaks are wider than the peaks seen in Figure 6.11 for the non irradiated chip: this is a consequence of the radiation-induced bulk damage.
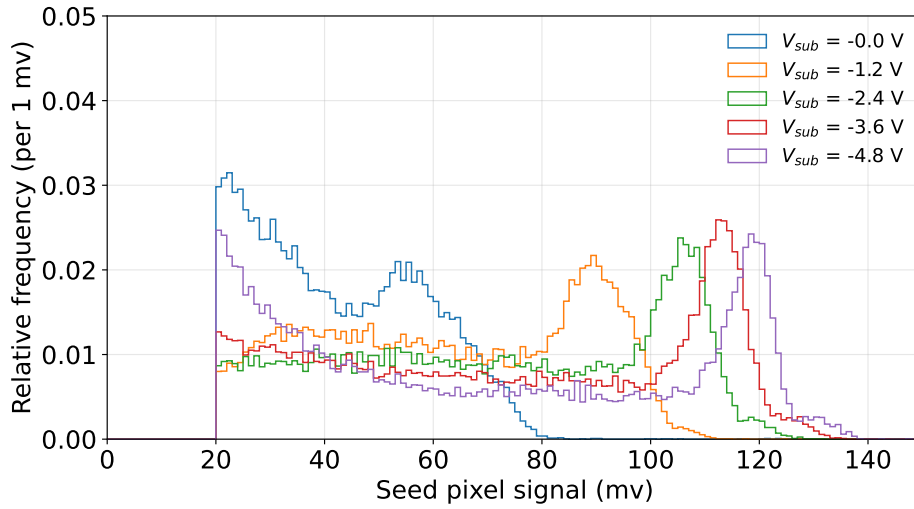
(a) AF10P_W22B61 (2×10^{15} n_{eq}/cm^2)
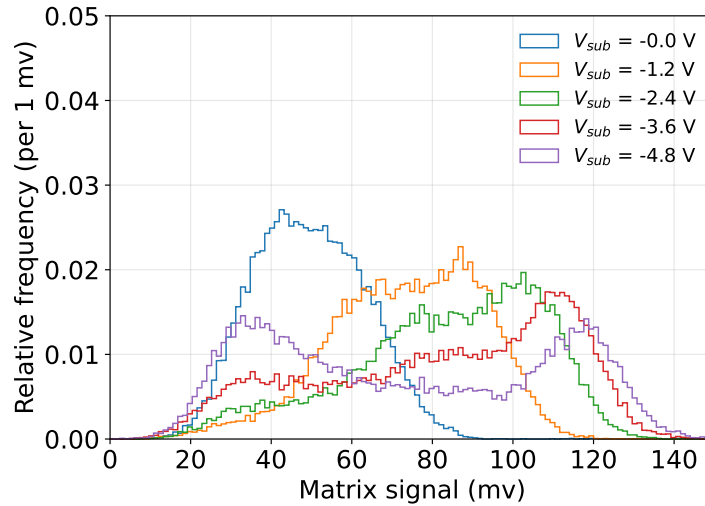
(b) AF10P_W22B61 (2×10^{15} n_{eq}/cm^2)

Figure 6.14: Distribution of signal for chip AF10P_W22B61 (2×10^{15} n_{eq}/cm^2).

In Figure 6.15, the seed and the matrix signal distributions in mV for chip AF10P_W22B63 (5×10^{15} n_{eq}/cm^2) are shown for all V_{bb} values. It is possible to see that the signal amplitude shifts to higher voltage values V as the reverse bias voltage increases, because the capacitance C decreases and the charge collected Q is almost the same ($V = Q/C$). The *charge collection peak* is clearly distinguishable for $|V_{bb}|$ >0.0V; the peaks are wider than the peaks seen in Figure 6.11 for the non irradiated chip: this is a consequence of the radiation-induced bulk damage. At this irradiation level, we see in the matrix signal distribution the *charge sharing peak* mentioned before in subsection 6.1.5.

(a) AF10P_W22B63 (5×10^{15} n_{eq}/cm^2)

(b) AF10P_W22B63 (5×10^{15} n_{eq}/cm^2)

Figure 6.15: Distribution of signal for chip AF10P_W22B63 (5×10^{15} n_{eq}/cm^2).

6.1.6.1 $\mathbf{V}_{bb}$ comparison

The calibration shown in subsection 6.1.2 is used to convert the signal from mV to electrons. Comparing the spectra, expressed in electrons and acquired at different bias voltage values, it is possible to understand whether the chip is collecting the same amount of charge and if charge is spreading across the matrix. In Figure 6.16, Figure 6.17, Figure 6.18, Figure 6.19 and Figure 6.20 the seed and the matrix spectra are shown, after the conversion of the signal in charge, for different irradiation levels.

Figure 6.16 shows the spectra acquired with chip AF10P_W22B25 (not irradiated): the *calibration peak* is well distinguishable from the rest of the spectrum at all reverse bias voltage values, therefore it is possible to say that the electric field spatially extends inside the whole sensor and the charge collection is successful.
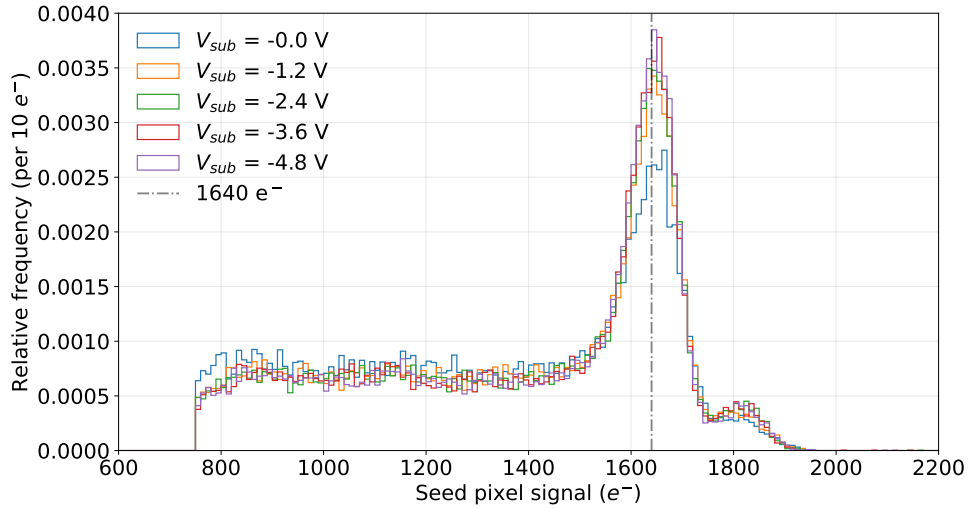
(a) AF10P_W22B25 (not irradiated)
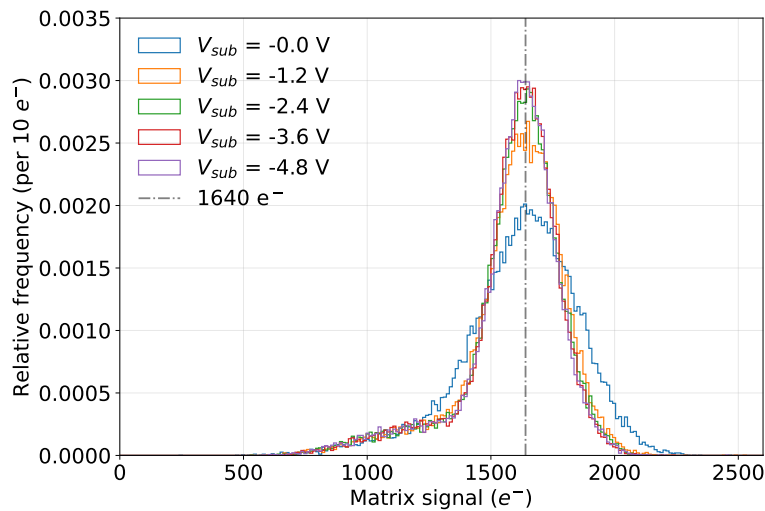
(b) AF10P_W22B25 (not irradiated)

Figure 6.16: Distribution of signal for chip AF10P_W22B25 (not irradiated).

Figure 6.17 shows the spectra acquired with chip AF10P_W22B57 (1×10^{14} n_{eq}/cm^2): the *calibration peak* is well distinguishable from the rest of the spectrum at all reverse bias voltage values, therefore it is possible to say that the electric field spatially extends inside the whole sensor and the charge collection is successful.
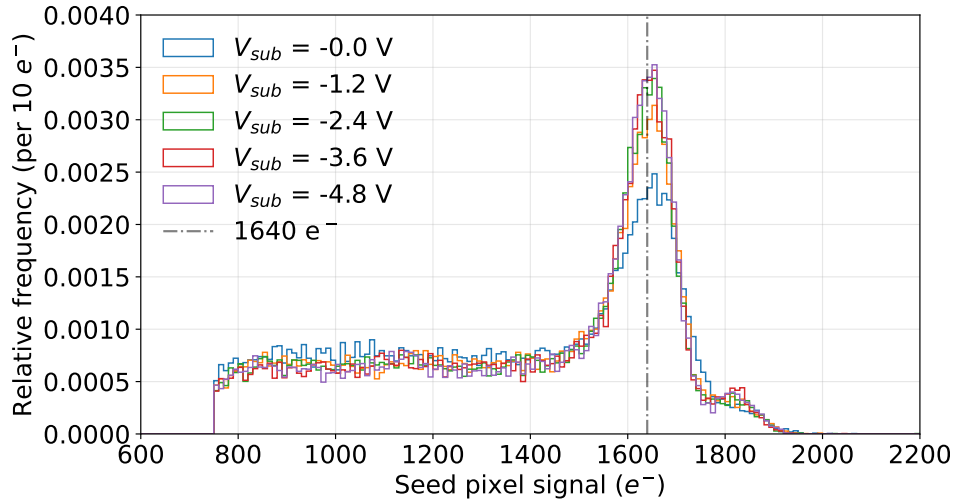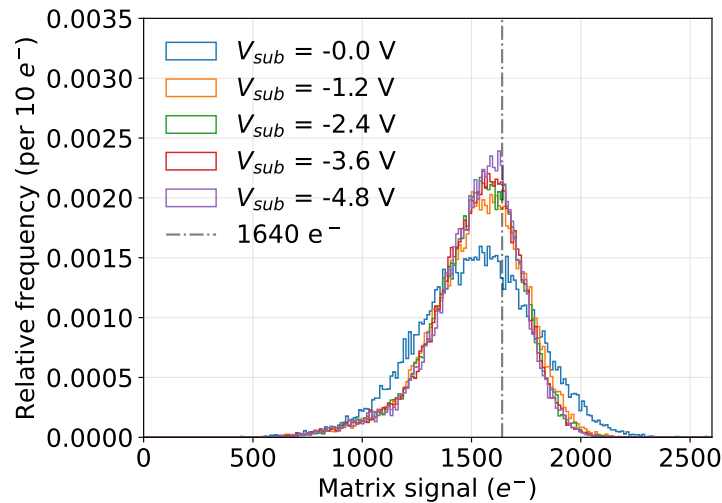

(a) AF10P_W22B57 (1×10^{14} n_{eq}/cm^2)
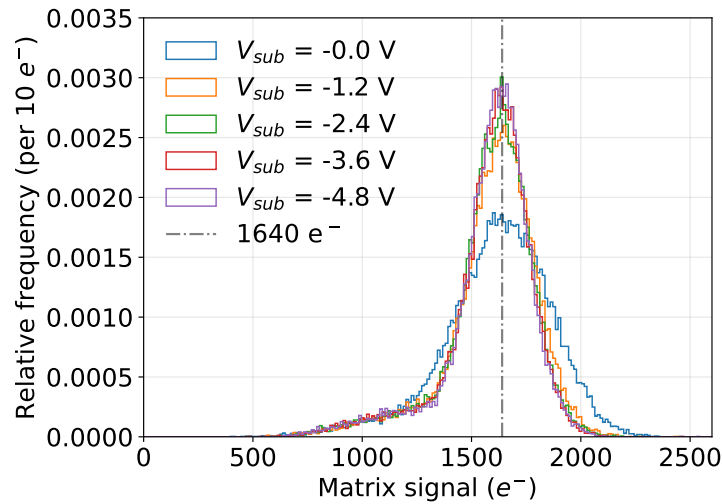
(b) AF10P_W22B57 (1×10^{14} n_{eq}/cm^2)

Figure 6.17: Distribution of signal for chip AF10P_W22B57 (1×10^{14} n_{eq}/cm^2).

In Figure 6.18 are shown the spectra acquired with chip AF10P_W22B58 (1×10^{15} n$_{eq}$/cm^2): the *calibration peak* is well distinguishable from the rest of the spectrum for $|V_{bb}|$ >0.0V.
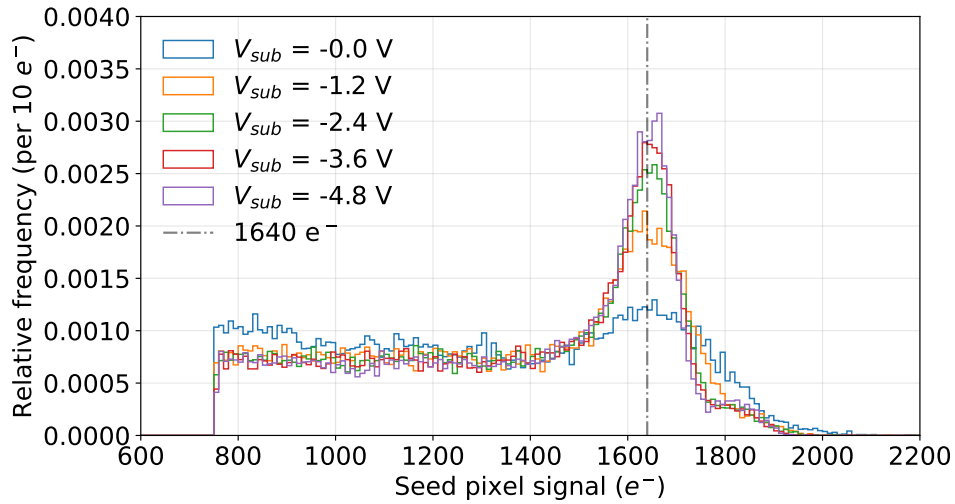
(a) AF10P_W22B58 (1×10^{15} n$_{eq}$/cm^2)

(b) AF10P_W22B58 (1×10^{15} n$_{eq}$/cm^2)

Figure 6.18: Distribution of signal for chip AF10P_W22B58 (1×10^{15} n$_{eq}$/cm^2).

Figure 6.19 shows the spectra acquired with chip AF10P_W22B61 (2×10^{15} n_{eq}/cm^2): the *calibration peak* is well distinguishable from the rest of the spectrum for $|V_{bb}| >0.0V$. The matrix signal distribution is wider because the noise of each pixel adds in quadrature; moreover, the main peak shows a shoulder towards lower values which is attributed to charge sharing between neighbouring pixels.
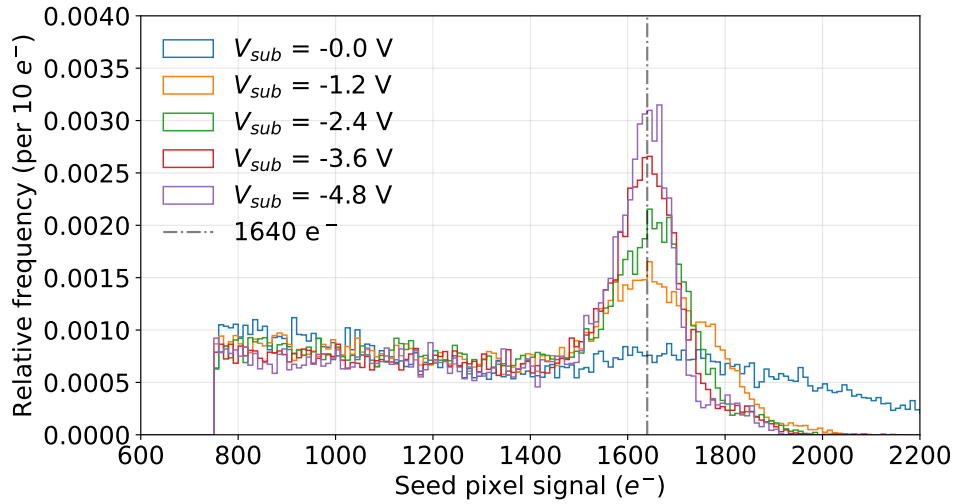

(a) AF10P_W22B61 (2×10^{15} n_{eq}/cm^2)
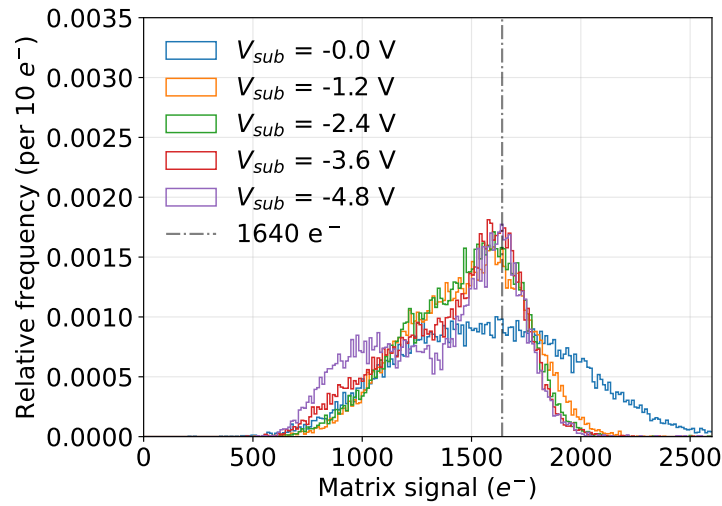
(b) AF10P_W22B61 (2×10^{15} n_{eq}/cm^2)

Figure 6.19: Distribution of signal for chip AF10P_W22B61 (2×10^{15} n_{eq}/cm^2).

In Figure 6.20 are shown the spectra acquired with chip AF10P_W22B63 (5×10^{15} n$_{eq}$/cm^2): the *calibration peak* is well distinguishable from the rest of the spectrum for $|V_{bb}| >0.0$V. The matrix signal distribution is wider because the noise of each pixel adds in quadrature; moreover, the main peak shows a shoulder towards lower values which is attributed to charge sharing between neighbouring pixels.
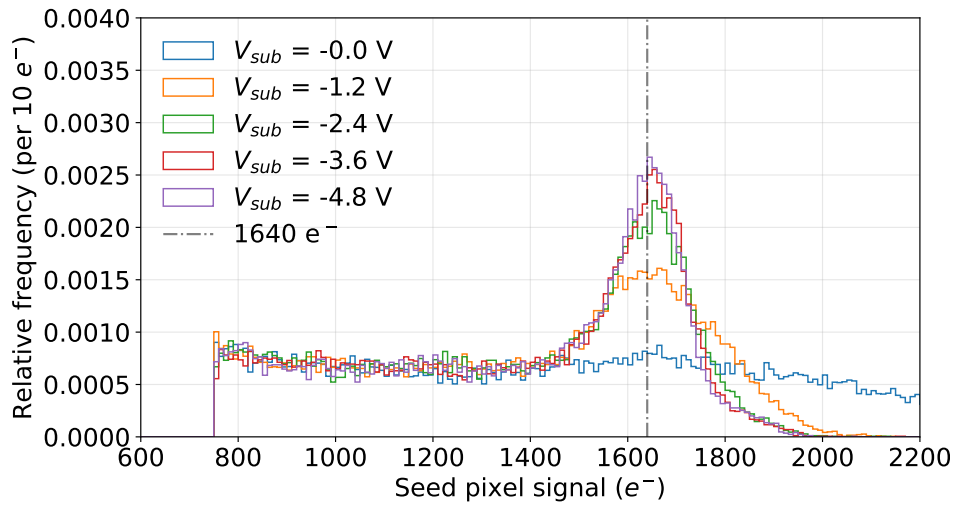
(a) AF10P_W22B63 (5×10^{15} n$_{eq}$/cm^2)
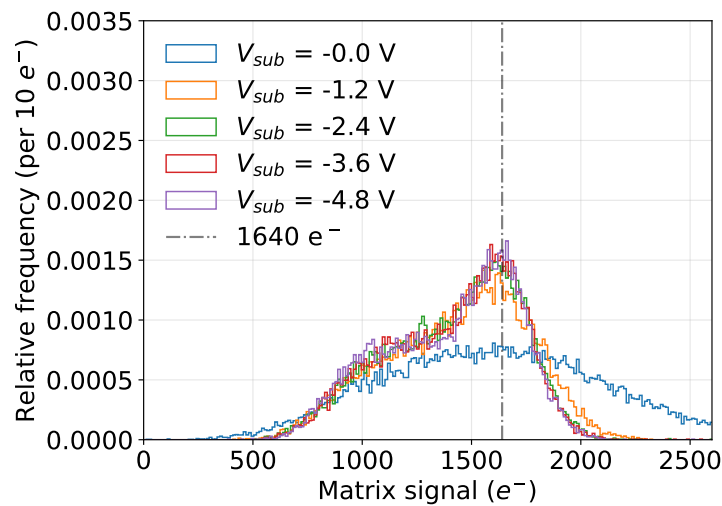
(b) AF10P_W22B63 (5×10^{15} n$_{eq}$/cm^2)

Figure 6.20: Distribution of signal for chip AF10P_W22B63 (5×10^{15} n$_{eq}$/cm^2).
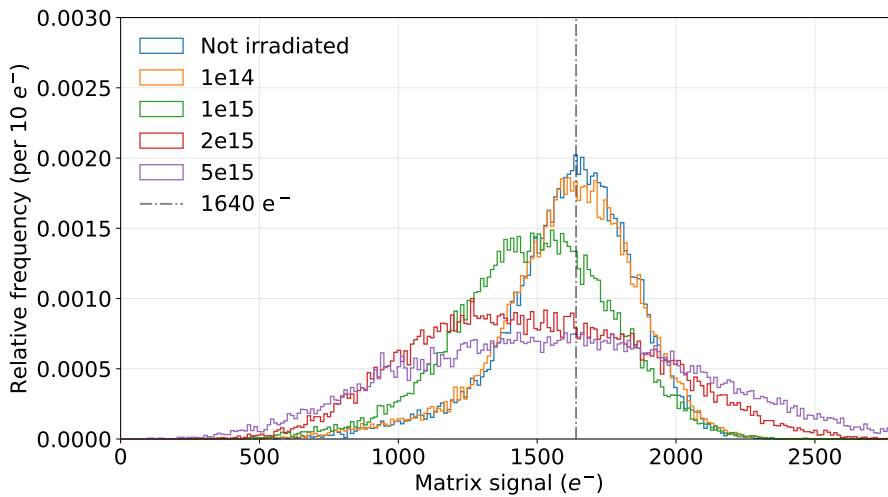
6.1.6.2   Irradiation comparison

Figure 6.21 and Figure 6.22 show the seed and matrix spectra acquired at $V_{bb} = 0.0$ V and $V_{bb} = -4.8$ V for all chips with same pixel pitch, comparing chips exposed to different irradiation levels.

When the detector is not depleted, i.e. $V_{bb} = 0.0$ V (Figure 6.21), only the spectra acquired with the chip with irradiation level 1×10^{14} n_{eq}/cm^2 is compatible with the non irradiated chip. In Figure 6.21b it is possible to see the matrix signal shifting to lower values as the irradiation level increases, which is compatible with the radiation induced effects mechanism explained in section 3.4. It represents an evidence of the increased number of trapping centres as well as of the changes in the electric field configuration, due to changes in the effective doping level in the epitaxial layer. Since the charge is collected mainly by diffusion when $V_{bb} = 0.0$V, the charge created as a particle crosses the detector can be trapped, hence a lower signal is measured. The charge lost is roughly estimated to be $\sim 50\%$ for the highest irradiation level.
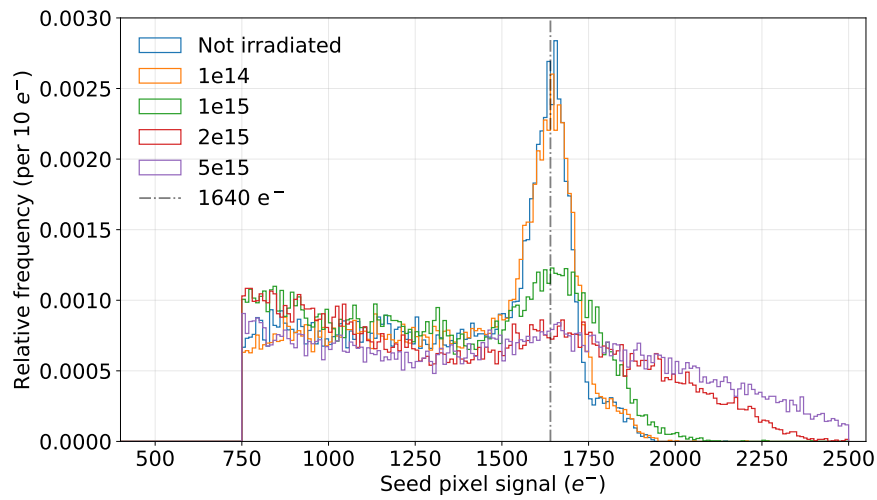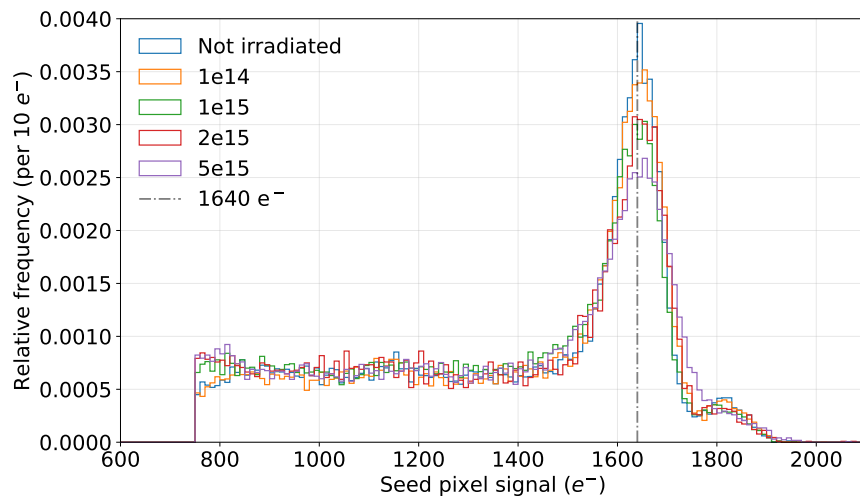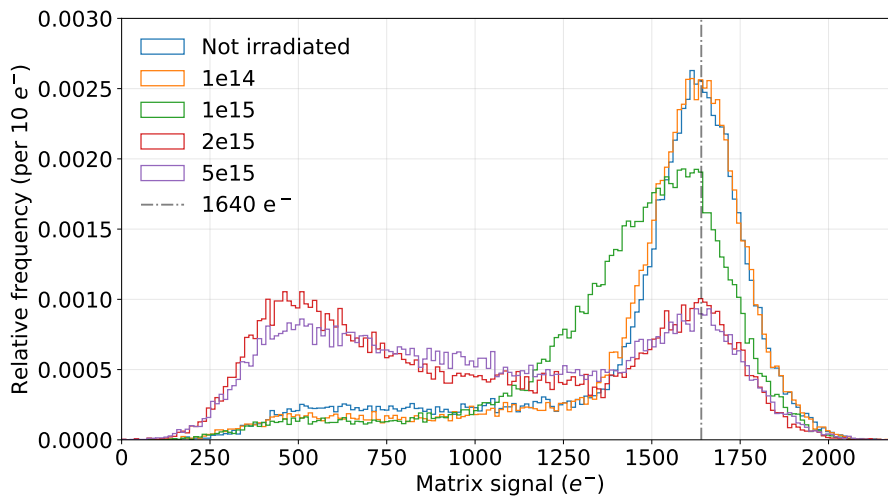

(a)

(b)

Figure 6.21: Irradiation comparison at $V_{bb} = 0.0$ V. The threshold value of 750 e$^-$ is set by software.

When the sensitive volume is depleted, i.e. $|V_{bb}| > 0.0$ V (Figure 6.22), the seed spectra better overlap (Figure 6.22a, even though in this plot it is possible to see that, as the irradiation level increases, the calibration peak height decreases; however the charge collection performance of chips exposed to high irradiation level is still compatible with the non-irradiated one. In Figure 6.22b, which shows the matrix signal, it is evident that for higher irradiation levels a secondary peak emerges due to a larger charge sharing between neighbouring pixels. The main peak is still centred around 1640 electrons, for all the irradiation levels.


(a)

(b)

Figure 6.22: Irradiation comparison at V_{bb} = -4.8 V. The threshold value of 750 e$^-$ is set by software.

6.1.6.3 Pitch comparison

The APTS chips tested were optimised to reduce charge sharing; evidence of the successful optimisation is in the comparison of chips with different pixel pitches. If the electric field is not distributed uniformly inside the whole pixel, then charges can diffuse to different collection diodes, leading to charge sharing between neighbouring pixels. This effect is expected to be more evident for large pixel pitches, as it is more difficult to have a uniform extended electric field inside the sensitive volume. As can be seen in Figure 6.23, for pitches 10 μm and 15 μm, the seed signal calibration peaks (1640 e$^-$ and 1800 e$^-$) are well distinguishable and the charge sharing peak is not visible in the spectra.
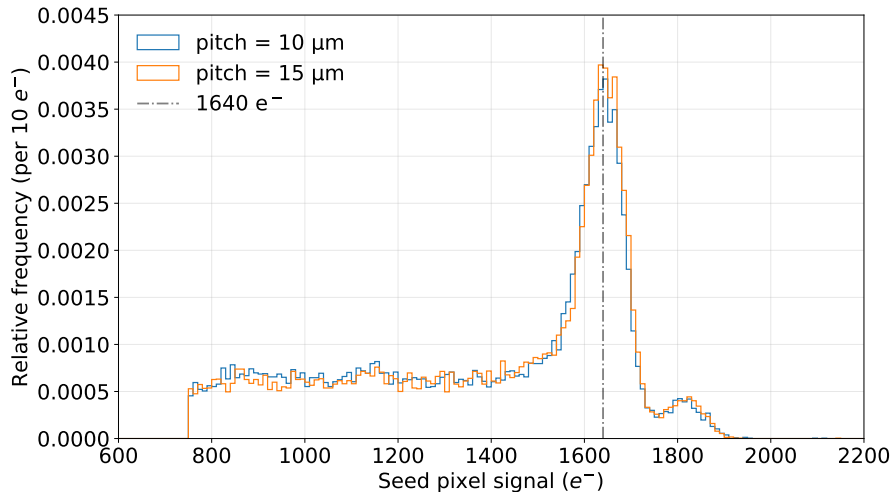

(a)
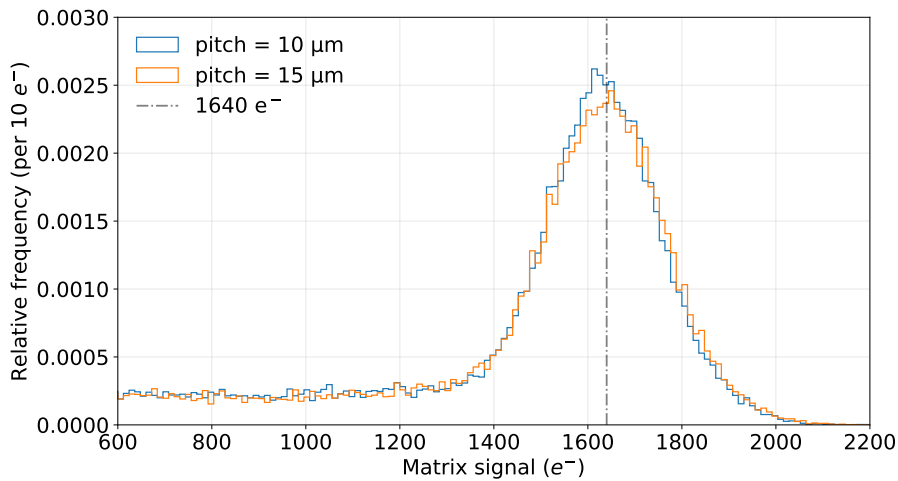
(b)

Figure 6.23: Pitch comparison at V$_{bb}$ = -4.8 V. The chips compared are the following: AF10P_W22B25 (pitch = 10 μm, not irradiated) and AF15P_W222B23 (pitch = 15 μm, not irradiated).

6.2 ^{90}Sr results

In this section we present the results of the analysis of the data acquired with the ^{90}Sr source for the following chips: AF15P_W22B23 (not irradiated) and AF10P_W22B57 (1×10^{14} n_{eq}/cm^2). AF10P_W22B58 (1×10^{15} n_{eq}/cm^2) and AF10P_W22B61 (2×10^{15} n_{eq}/cm^2). At the moment of writing, the ^{90}Sr source measurement was not performed with a non irradiated chip with pixel pitch 10 μm (see Table 5.1), therefore there is no reference for the evaluation of the performance of irradiated chips.

6.2.1 Signal distribution

The spectra emitted by the ^{90}Sr source contains a large fraction of low energy electrons that cause a larger signal than that of a MIP and a particle stopped inside the sensor can result in larger clusters (see subsection 6.2.3). A scintillator trigger could be used to select only higher energy electrons that are not stopped inside the sensing volume and reach the scintillator. Unfortunately this setup was not yet implemented at the time of writing. Therefore, for the scope of this thesis, the contamination due to low energy electrons was reduced by selecting only events higher than a certain threshold set by software during the analysis. Figure 6.24 shows the the β-spectra, obtained with the ^{90}Sr source, at V_{bb}=-4.8 V, of the non-irradiated chip (AF15P_W22B23) and chip AF10P_W22B57 (1×10^{14} n_{eq}/cm^2). The signal amplitude is expressed in mV. The fits of the spectra are performed with a Landau function (Equation 2.4).
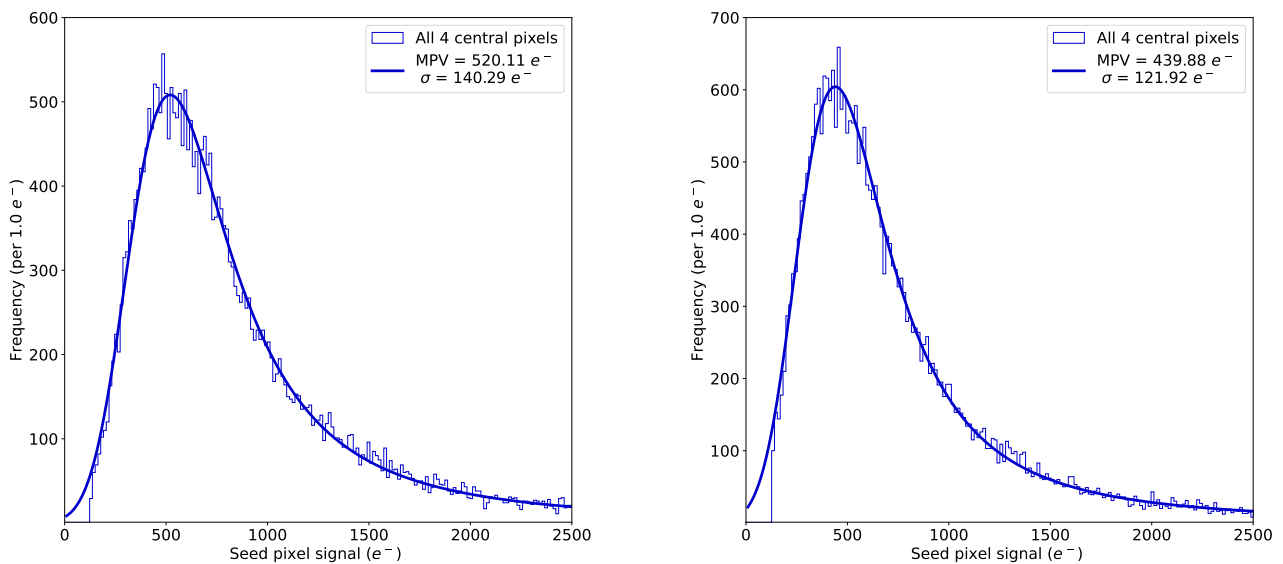
(a) AF15P_W22B23 (not irradiated)   (b) AF10P_W22B57 (1×10^{14} n_{eq}/cm^2)

Figure 6.24: Distribution of the signal amplitude from 4 central pixels (2×2 matrix) at V_{bb} = -4.8 V

6.2.2 Calibration

For the conversion of the signal measured in milliVolts to a number of electrons, the same calibration performed with the ^{55}Fe source is used (see subsection 6.1.2).

6.2.3 Cluster size

The cluster size due to electrons from β decays of the ^{90}Sr is larger than the cluster size due to X-rays showed in subsection 6.1.3: low energy electrons deposit more energy in the sensor as numerous electron/hole pairs are created along the particle track as it crosses the sensitive volume. And this, together with a small pixel pitch, leads to relatively large clusters.

Figure 6.25 shows the cluster size for all the tested chips, at different V_{bb} values. Increasing the exposure to neutrons causes an increase of charge trapping, which leads to smaller cluster sizes and reduced charge sharing: indeed, as shown in Figure 6.25c and Figure 6.25d, the relative frequency of cluster size 1 for irradiation levels 1×10^{15} n_{eq}/cm^2 and 2×10^{15} n_{eq}/cm^2 is higher with respect to the other cases.

(a) AF15P_W22B23 (not irradiated)

(b) AF10P_W22B57 (1×10^{14} n_{eq}/cm^2)

(c) AF10P_W22B58 (1×10^{15} n_{eq}/cm^2)
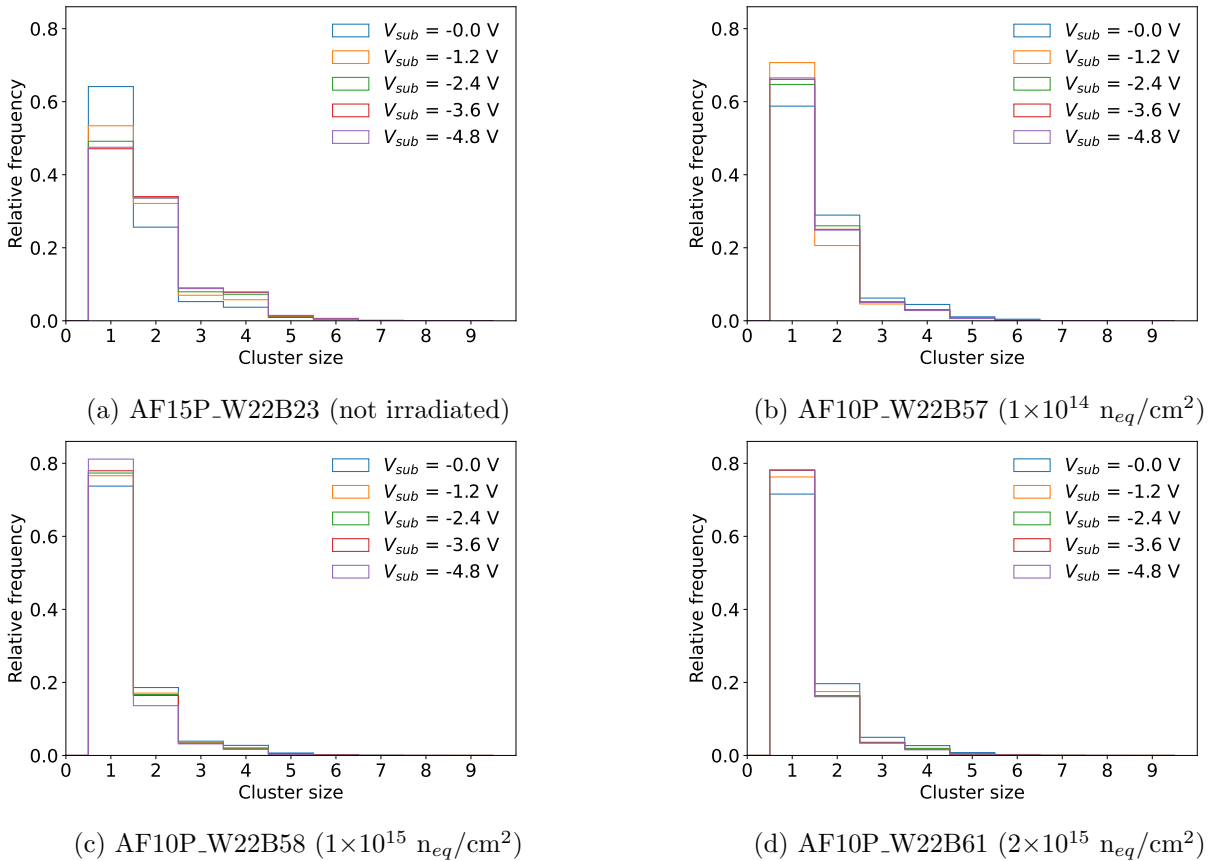
(d) AF10P_W22B61 (2×10^{15} n_{eq}/cm^2)

Figure 6.25: Cluster size comparison with the ^{90}Sr source.

6.2.4 Charge sharing

Figure 6.26 and Figure 6.27 show that the effects of irradiation with regards to charge sharing are far less evident using ^{90}Sr electrons compared to using ^{55}Fe X-rays. The different sensitivity to charge sharing is attributed to the intrinsic way electrons deposit charge along their tracks with larger cluster sizes.
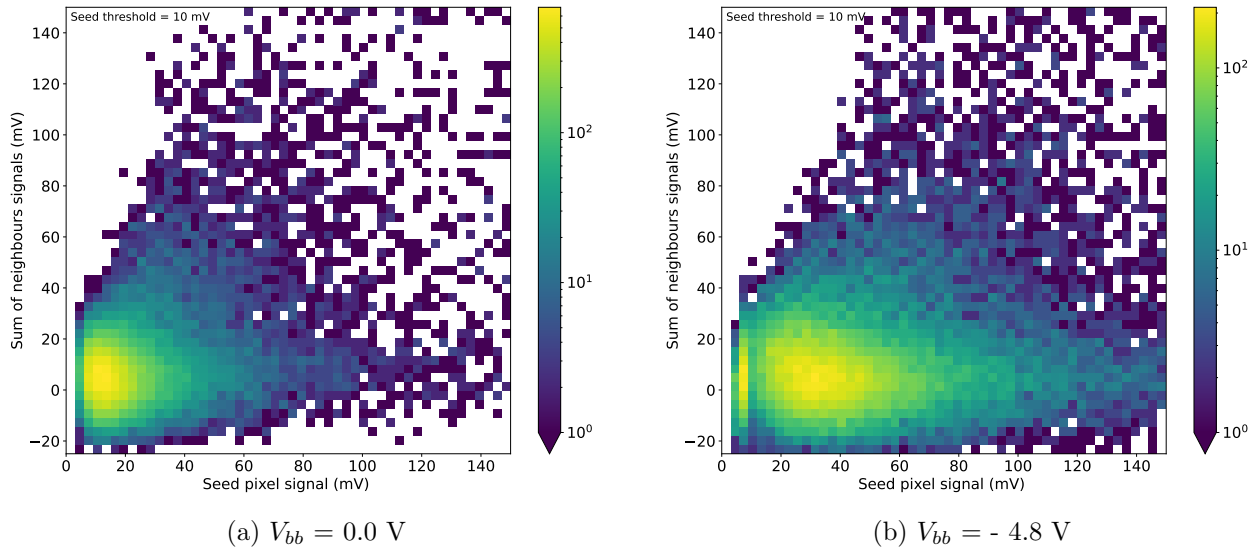

(a) $V_{bb} = 0.0$ V

(b) $V_{bb} = - 4.8$ V

Figure 6.26: Charge sharing, chip AF10P_W22B57 (1×10^{14} n$_{eq}$/cm^2).
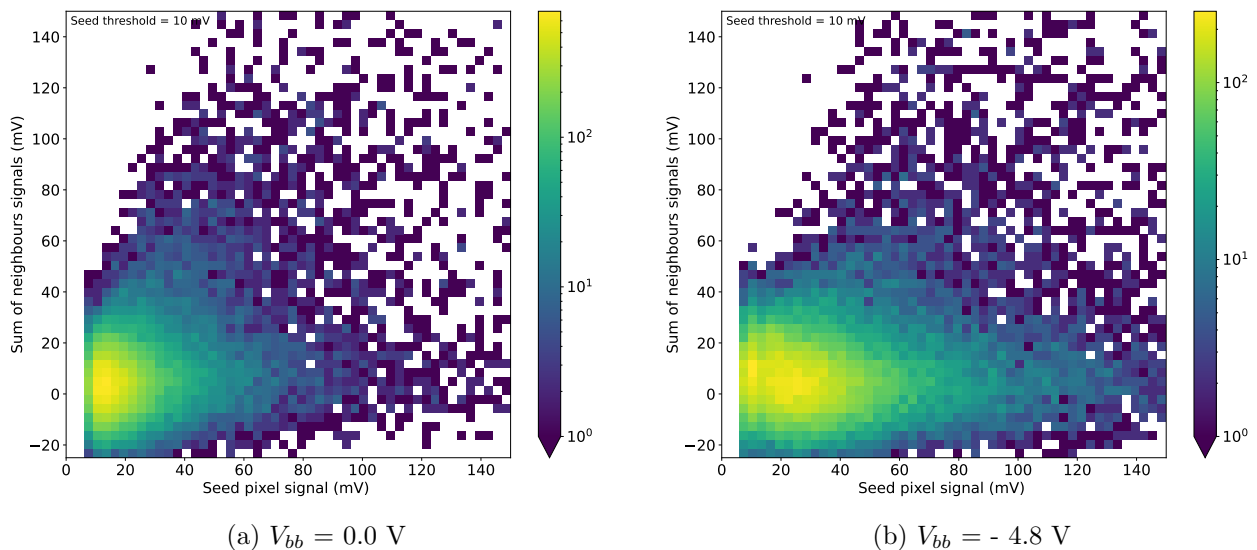

(a) $V_{bb} = 0.0$ V

(b) $V_{bb} = - 4.8$ V

Figure 6.27: Charge sharing, chip AF10P_W22B61 (2×10^{15} n$_{eq}$/cm^2).

6.2.5 Result comparison

This section presents and discusses the results about the amount of charge collected by the non irradiated chip (AF15P_W22B23) and the comparison between the chips exposed to different irradiation level.

As mentioned before in section 2.2, ~80 electron-hole pairs per micron of path are generated by a traversing MIP in silicon, therefore, for thicknesses of 300 μm, the expected number of pairs generated is ~22000-24000. However, for thinner pieces of silicon, ~60-70 pairs are expected to be created. Hence, since the sensitive layer in the tested structures is ~10μm thick, we expect to see a signal of ~600-700 electrons when the detector is depleted (for the non irradiated chip) and an even smaller number in the case of irradiated sensors.

6.2.5.1 V_{bb} comparison

From the fit of the matrix signal it is possible to extract the MPV of the Landau distribution, which corresponds to the most probable value of charge released by a traversing particle. The fit is performed on the data measured by the matrix, because, as shown in subsection 6.2.3, the charge is collected not just by the seed pixel, but also by neighbouring pixels.

Figure 6.28 shows the matrix signal distribution for the chip AF15P_W22B23 (not irradiated, pixel pitch = 15 μm) at V_{bb} = -2.4 V, -3.6 V and -4.8 V. The results obtained from the fit of the matrix signal distribution at $|V_{bb}|$ >2.4 V show that, for these bias voltages, the MPV is stable at ~630 electrons, which is in line with the expected number of pairs generated in silicon volume 10 μm thick.
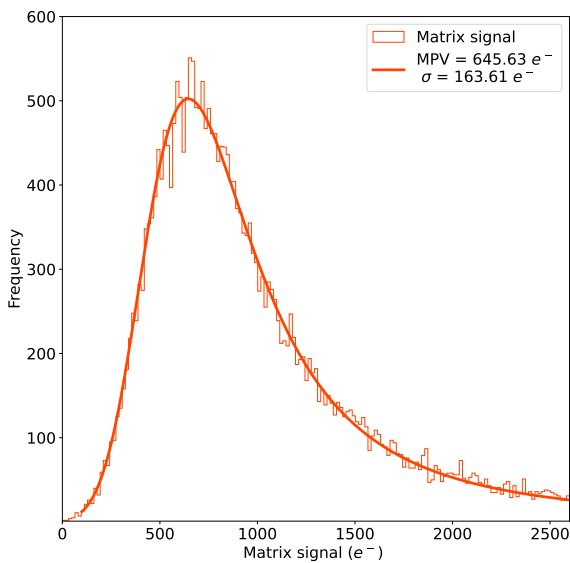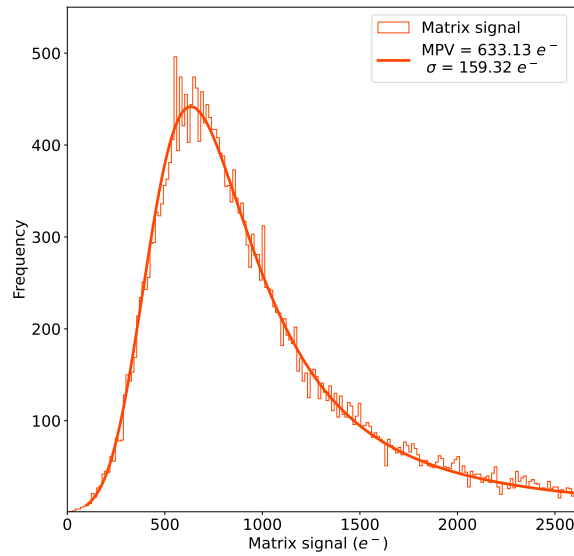

(a) V_{bb}=-2.4V.
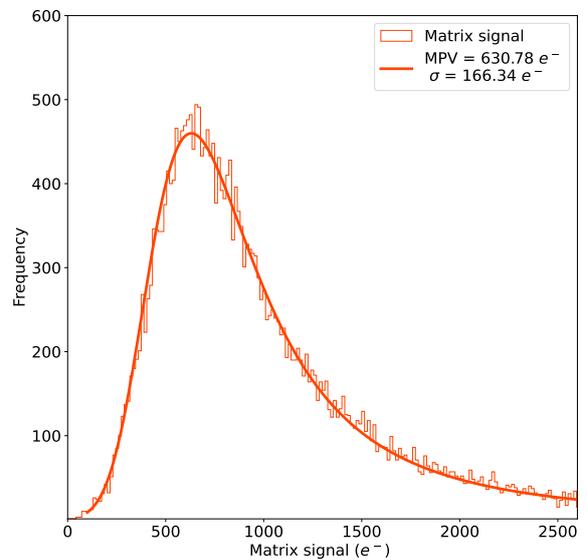
(b) V_{bb}=-3.6V.

(c) V$_{bb}$=-4.8V.

Figure 6.28: Distribution of the matrix signal for chip AF15P_W22B23 (not irradiated).

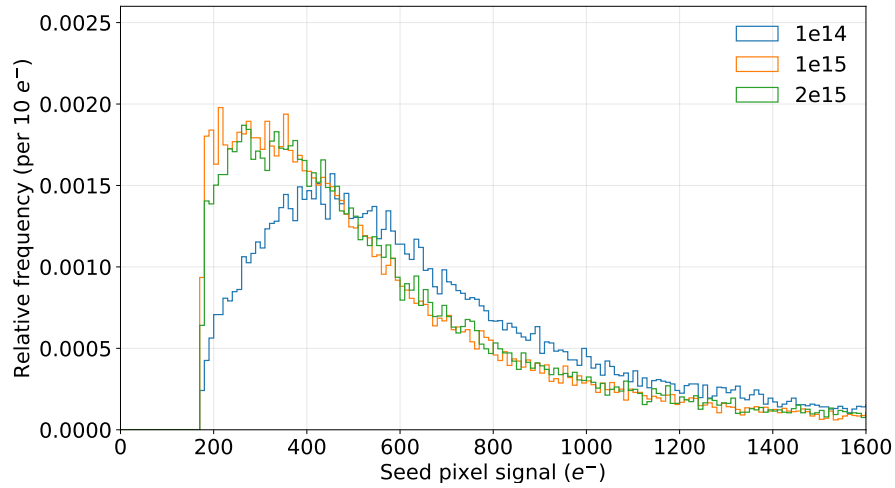#### 6.2.5.2 Irradiation comparison

Figure 6.29 shows the seed and the matrix spectra, after the conversion in charge, at V$_{bb}$=-4.8V, for all the irradiated chips with the same pixel pitch (10 μm).
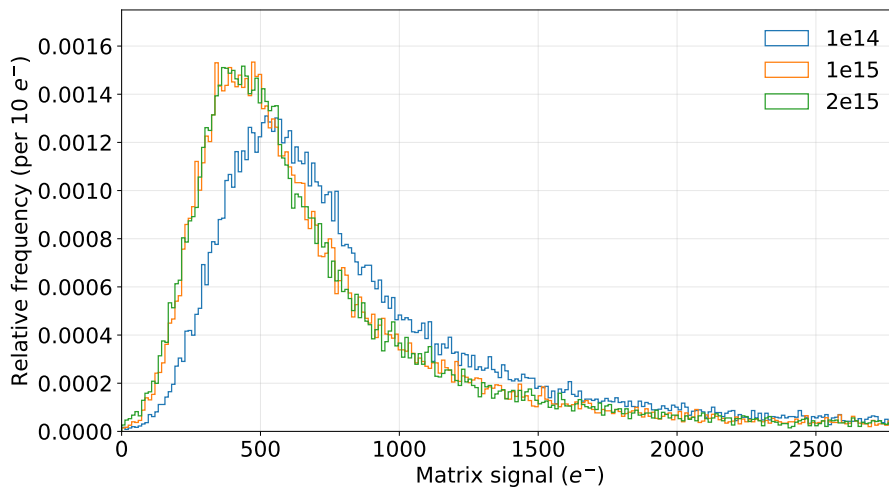
When the sensitive volume is depleted, i.e. $|V_{bb}| > 0.0$ V (Figure 6.29), the signal measured by the chip exposed to the lowest irradiation level is higher than the signal measured with the other chips: this means that for higher neutron fluences, less charge is collected, as a consequence of charges being trapped in trapping centres induced by radiation. In Table 6.3 are summarised the MPV obtained from the fit at V_{bb}=-4.8V: the chip exposed to the lowest irradiation level collects more charge as expected, the other two chips collect ~ 20% less charge.

Table 6.3: MPV obtained from the Landau fit for V_{bb}=-4.8V.

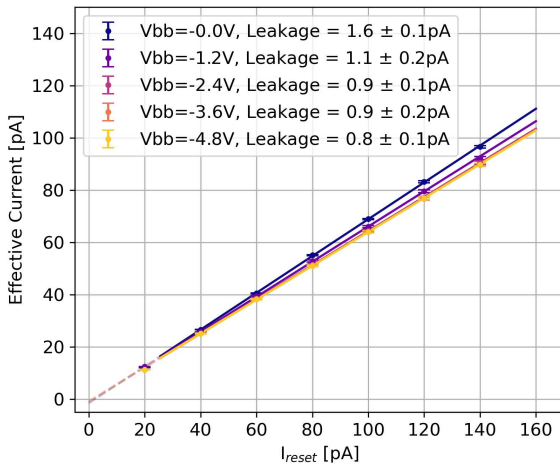|	AF10P_W22B57 $(1\times10^{14}$ n$_{eq}$/cm$^2)$	AF10P_W22B58 $(1\times10^{15}$ n$_{eq}$/cm$^2)$	AF10P_W22B61 $(2\times10^{15}$ n$_{eq}$/cm$^2)$
MPV seed	439.88 e^-	301.44 e^-	328.53 e^-
MPV matrix	523.40 e^-	413.77 e^-	411.08 e^-

(a)

(b)

Figure 6.29: Irradiation comparison at V_{bb} = -4.8 V. The threshold value of 175 e$^-$ is set by software.

6.3   Leakage current

In this section we report on the leakage test performed with the following chips: AF15P_W22B23 (not irradiated), AF10P_W22B57 (1×10^{14} n_{eq}/cm^2), AF10P_W22B58 (1×10^{15} n_{eq}/cm^2), AF10P_W22B61 (2×10^{15} n_{eq}/cm^2). The leakage current is determined for each pixel in the matrix, using the following fit function already discussed in section 5.5:

$$I_{eff} = m \cdot I_{reset} - I_{leak} \qquad (6.4)$$

During the testing procedure, the chip AF10P_W22B58 stopped working as usual (the current that was being supplied to the substrate was above the current limit set on the power supply to operate in safe conditions), and it was possible to conclude the measurements only for V_{bb} = 0.0, -1.2, -2.4 V (Figure 6.30c). For the chip AF10P_W22B61, the fit at V_{bb} = 0.0 V was not successful, therefore it was not possible to give an estimate of the leakage current. The results are summarized in Table 6.4.

(a) AF15P_W22B23 (not irradiated)
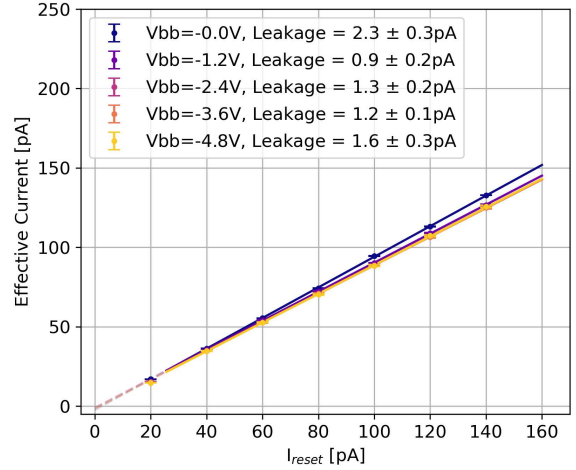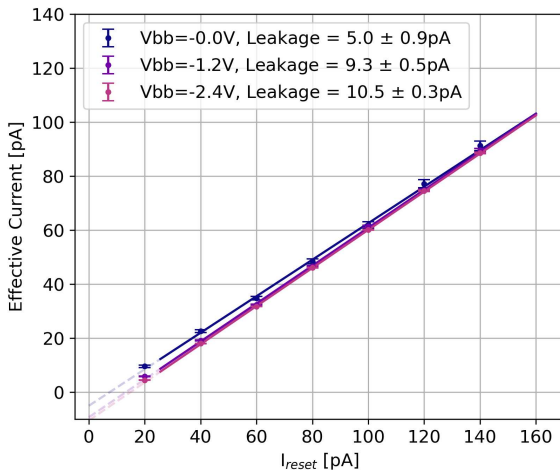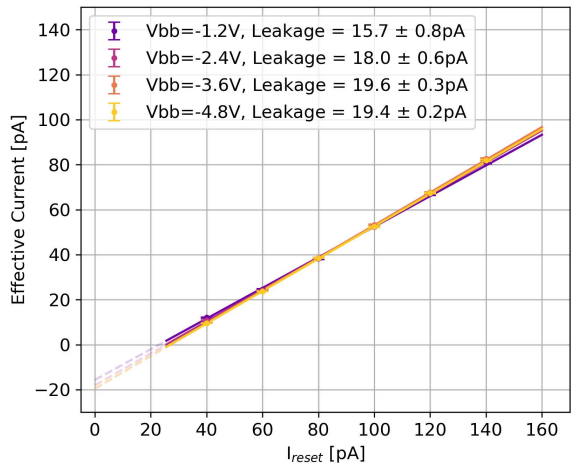
(b) AF10P_W22B57 (1×10^{14} n_{eq}/cm^2)

(c) AF10P_W22B58 (1×10^{15} n_{eq}/cm^2)

(d) AF10P_W22B61 (2×10^{15} n_{eq}/cm^2)

Figure 6.30: Linear fit of the effective current for pixel [1][1].

Table 6.4: Leakage current values obtained from linear fits for different chips at all reverse bias voltage values, for pixel [1][1].

V_{bb}	I_{leak} [pA] AF15P_W22B23 (not irradiated)	I_{leak} [pA] AF10P_W22B57 (1×10^{14} n_{eq}/cm^2)	I_{leak} [pA] AF10P_W22B58 (1×10^{15} n_{eq}/cm^2)	I_{leak} [pA] AF10P_W22B61 (2×10^{15} n_{eq}/cm^2)
0.0 V	1.6 ± 0.1	2.3 ± 0.3	5.0 ± 0.9	-
- 1.2 V	1.1 ± 0.2	0.9 ± 0.2	9.3 ± 0.5	15.7 ± 0.8
- 2.4 V	0.9 ± 0.1	1.3 ± 0.2	10.5 ± 0.3	18.0 ± 0.6
- 3.6 V	0.9 ± 0.2	1.2 ± 0.1	-	19.6 ± 0.3
- 4.8 V	0.8 ± 0.1	1.6 ± 0.3	-	19.4 ± 0.2

Comparing all the pixels in the matrix, uniformity is good: there is no significant difference between the leakage current measured in each pixel as expected (the values vary at most 15% from the mean current value). An example of the leakage current variation in the matrix can be seen in Figure 6.31.
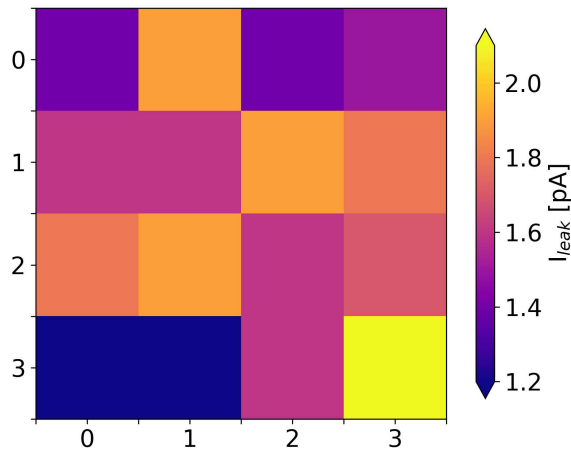
Figure 6.31: Leakage current values of each pixel in the matrix of chip AF10P_W22B57 (1×10^{14} n_{eq}/cm^2), at V_{bb}=-4.8 V.

Figure 6.32 shows the leakage current values at all V_{bb} values, for all the irradiated chips. The leakage current increases of one order of magnitude: for the lowest irradiation level (1×10^{14} n_{eq}/cm^2) I_{leak} <2.5pA, for the highest irradiation level (2×10^{15} n_{eq}/cm^2) I_{leak} <20pA.
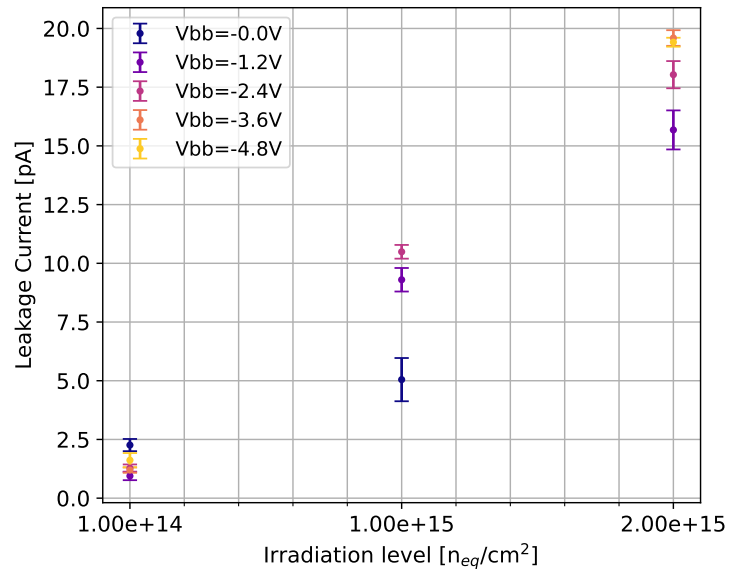
Figure 6.32: Leakage current values of pixel [1][1], for all irradiated chips, for all V_{bb} values.

Conclusions

This thesis work presents the performance study of irradiated Monolithic Active Pixel Sensors (MAPS) test structures, designed and fabricated for the future upgrade of the Inner Tracking System (ITS3) of the ALICE experiment at CERN. The final ITS3 sensor will feature a thickness ≤ 50 μm, a pixel pitch about 20×25 μm^2, as well as the capability to withstand radiation loads of 10^{13} 1 MeV n_{eq}/cm^2 of Non Ionizing Energy Loss (NIEL) and 10 kGy of Total Ionising Dose (TID).

My work focused on the Analog Pixel Test structures (APTS) chips, arrays of 4×4 active pixels, coming in various combinations of pixel size, pixel design, process types, reverse biasing scheme and peripheral analog output buffer, which proved to be an effective vehicle to study the charge collection properties of the different variants.

For my thesis, I studied APTS-SF chips: they are DC-coupled chips, with 10 μm and 15 μm of pitch, a simple front-end electronics base on a source follower, analog output, with a substrate modification (modified-with-gap) to ease charge collection by drift.

One non-irradiated chip, with 15 μm pixel pitch, was used as a reference; in view of future HL-LHC upgrades, four other chips, all with 10 μm pixel pitch, were exposed to different very high neutron fluences, one to two orders of magnitude greater than the expected fluences for the ITS3 upgrade: 1×10^{14} n_{eq}/cm^2, 1×10^{15} n_{eq}/cm^2, 2×10^{15} n_{eq}/cm^2 and 5×10^{15} n_{eq}/cm^2.

To compare and characterise the behaviour of the irradiated chips with respect to the reference one, I used ^{55}Fe and ^{90}Sr sources. All measurements were taken in a cleanroom, in a cold box at a controlled temperature $T \leq 14$ °C, to keep the leakage current under control. Parameters like noise, gain, cluster size and charge collection efficiency have been quantified for all the radiation loads and for different bias conditions.

The results prove that the tested APTS-SF maintain good charge collection efficiency and low noise even when irradiated to very high neutron fluence values. The results obtained provide encouraging evidence that the modified-with-gap process is well suited to have the radiation tolerance for the next ITS3 upgrade and future ones.

Bibliography

[1] JR Srour, , and JW Palko. Displacement damage effects in irradiated semiconductor devices. *IEEE Transactions on Nuclear Science*, 60(3):1740–1766, 2013.

[2] Ivan Perić, Mridula Prathapan, Heiko Augustin, Mathieu Benoit, Raimon Casanova Mohr, Dominik Dannheim, Felix Ehrler, Fadoua Guezzi Messaoud, Moritz Kiehn, Andreas Nürnberg, et al. A high-voltage pixel sensor for the atlas upgrade. *Nuclear Instruments and Methods in Physics Research Section A: Accelerators, Spectrometers, Detectors and Associated Equipment*, 924:99–103, 2019.

[3] Stella Orfanelli, CMS collaboration, et al. The phase 2 upgrade of the cms inner tracker. *Nuclear Instruments and Methods in Physics Research Section A: Accelerators, Spectrometers, Detectors and Associated Equipment*, 980:164396, 2020.

[4] P Delpierre. A history of hybrid pixel detectors, from high energy physics to medical imaging. *Journal of Instrumentation*, 9(05):C05059, 2014.

[5] Sinuo Zhang, David-Leon Pohl, Tomasz Hemperek, and Jochen Dingfelder. Improving the spatial resolution of silicon pixel detectors through sub-pixel cross-coupling. *Nuclear Instruments and Methods in Physics Research Section A: Accelerators, Spectrometers, Detectors and Associated Equipment*, 981:164524, 2020.

[6] Maurice Garcia-Sciveres and Norbert Wermes. A review of advances in pixel detectors for experiments with high rate and radiation. *Reports on Progress in Physics*, 81(6):066101, 2018.

[7] Nicole Apadula, Whitney Armstrong, James Brau, Martin Breidenbach, R Caputo, Gabriella Carinii, Alberto Collu, Marcel Demarteau, Grzegorz Deptuch, Angelo Dragone, et al. Monolithic active pixel sensors on cmos technologies. *arXiv preprint arXiv:2203.07626*, 2022.

[8] M. Buckland. First measurements with monolithic active pixel test structures produced in a 65 nm cmos process, 2023. `arXiv:2309.14814`.

[9] Kenneth Aamodt, A Abrahantes Quintana, R Achenbach, S Acounis, D Adamová, C Adler, M Aggarwal, F Agnese, G Aglieri Rinella, Z Ahammed, et al. The alice experiment at the cern lhc. *Journal of Instrumentation*, 3(08):S08002, 2008.

[10] Shreyasi Acharya, Dagmar Adamová, Jonatan Adolfsson, Madan M Aggarwal, Gianluca Aglieri Rinella, Michelangelo Agnello, Nikita Agrawal, Zubayer Ahammed, Nazeer Ahmad, Sang Un Ahn, et al. Searches for transverse momentum dependent flow vector fluctuations in pb-pb and p-pb collisions at the lhc. *Journal of high energy physics*, 2017(9):1–33, 2017.

[11] ALICE Collaboration. $\psi(2s)$ suppression in pb-pb collisions at the lhc, 2022. `arXiv:2210.08893`.

[12] Alice Collaboration et al. Technical design report of the inner tracking system. *CERN/LHCC*, 12:1999, 1999.

[13] Betty Abelev, J Adam, D Adamová, MM Aggarwal, G Aglieri Rinella, M Agnello, A Agostinelli, N Agrawal, Z Ahammed, N Ahmad, et al. Technical design report for the upgrade of the alice inner tracking system. *Journal of Physics G: Nuclear and Particle Physics*, 41(8), 2014.

[14] Felix Reidt, Alice Collaboration, et al. Upgrade of the alice its detector. *Nuclear Instruments and Methods in Physics Research Section A: Accelerators, Spectrometers, Detectors and Associated Equipment*, 1032:166632, 2022.

[15] David Cohen, Ephie Koltin, Margalit Ilovich Ayelet, and Amit Shacham. Stitching design rules for forming interconnect layers, May 1 2001. US Patent 6,225,013.

[16] G Aglieri Rinella, Alice Collaboration, et al. Developments of stitched monolithic pixel sensors towards the alice its3. *Nuclear Instruments and Methods in Physics Research Section A: Accelerators, Spectrometers, Detectors and Associated Equipment*, 1049:168018, 2023.

[17] Fuyue Wang, Benjamin Nachman, and Maurice Garcia-Sciveres. Ultimate position resolution of pixel clusters with binary readout for particle tracking. *Nuclear Instruments and Methods in Physics Research Section A: Accelerators, Spectrometers, Detectors and Associated Equipment*, 899:10–15, 2018.

[18] ITS ALICE. Expression of interest for an alice its upgrade in ls3, 2019.

[19] PN junction. General Photo. URL: https://www.mks.com/n/diode-physics.

[20] Leonardo Rossi. *Pixel detectors: From fundamentals to applications*. Springer Science & Business Media, 2006.

[21] M Lozano, E Cabruja, A Collado, J Santander, and M Ullán. Bump bonding of pixel systems. *Nuclear Instruments and Methods in Physics Research Section A: Accelerators, Spectrometers, Detectors and Associated Equipment*, 473(1-2):95–101, 2001.

[22] G Deptuch, M Winter, W Dulinski, D Husson, R Turchetta, and JL Riester. Simulation and measurements of charge collection in monolithic active pixel sensors. *Nuclear Instruments and Methods in Physics Research Section A: Accelerators, Spectrometers, Detectors and Associated Equipment*, 465(1):92–100, 2001.

[23] Walter Snoeys, G Aglieri Rinella, H Hillemanns, T Kugathasan, M Mager, L Musa, P Riedler, F Reidt, J Van Hoorne, A Fenigstein, et al. A process modification for cmos monolithic active pixel sensors for enhanced depletion, timing performance and radiation tolerance. *Nuclear Instruments and Methods in Physics Research Section A: Accelerators, Spectrometers, Detectors and Associated Equipment*, 871:90–96, 2017.

[24] W Snoeys. Monolithic pixel detectors for high energy physics. *Nuclear Instruments and Methods in Physics Research Section A: Accelerators, Spectrometers, Detectors and Associated Equipment*, 731:125–130, 2013.

[25] M Dyndal, V Dao, P Allport, I Asensi Tortajada, M Barbero, S Bhat, D Bortoletto, I Berdalovic, C Bespin, C Buttar, et al. Mini-malta: radiation hard pixel designs for small-electrode monolithic cmos sensors for the high luminosity lhc. *Journal of Instrumentation*, 15(02):P02005, 2020.

[26] Ivan Caicedo, Marlon Barbero, Pierre Barrillon, Ivan Berdalovic, Siddharth Bhat, Christian Bespin, Patrick Breugnon, Roberto Cardella, Zongde Chen, Yavuz Degerli, et al. The monopix chips: Depleted monolithic active pixel sensors with a column-drain read-out architecture for the atlas inner tracker upgrade. *Journal of Instrumentation*, 14(06):C06006, 2019.

[27] Christian Bespin, Marlon Barbero, Pierre Barrillon, Ivan Berdalovic, Siddharth Bhat, Patrick Breugnon, Ivan Caicedo, Roberto Cardella, Zongde Chen, Yavuz Degerli, et al. Dmaps monopix developments in large and small electrode designs. *Nuclear Instruments and Methods in Physics Research Section A: Accelerators, Spectrometers, Detectors and Associated Equipment*, 978:164460, 2020.

[28] Magdalena Munker, Mathieu Benoit, Dominik Dannheim, Amos Fenigstein, Thanushan Kugathasan, Tomer Leitner, Heinz Pernegger, Petra Riedler, and Walter Snoeys. Simulations of cmos pixel sensors with a small collection electrode, improved for a faster charge collection and increased radiation tolerance. *Journal of Instrumentation*, 14(05):C05013, 2019.

[29] William Shockley. Currents to conductors induced by a moving point charge. *Journal of applied physics*, 9(10):635–636, 1938.

[30] Simon Ramo. Currents induced by electron motion. *Proceedings of the IRE*, 27(9):584–585, 1939.

[31] Michael Moll. Displacement damage in silicon detectors for high energy physics. *IEEE Transactions on Nuclear Science*, 65(8):1561–1582, 2018.

[32] Michael Wirthlin. High-reliability fpga-based systems: Space, high-energy physics, and beyond. *Proceedings of the IEEE*, 103(3):379–389, 2015.

[33] Yuanfu Zhao, Suge Yue, Xinyuan Zhao, Shijin Lu, Qiang Bian, Liang Wang, and Yongshu Sun. Single event soft error in advanced integrated circuit. *Journal of Semiconductors*, 36(11):111001, 2015.

[34] Fred W Sexton. Destructive single-event effects in semiconductor devices and ics. *IEEE Transactions on Nuclear Science*, 50(3):603–621, 2003.

[35] Timothy R Oldham and FB McLean. Total ionizing dose effects in mos oxides and devices. *IEEE transactions on nuclear science*, 50(3):483–499, 2003.

[36] JT Devreese. Polarons. In *AIP Conference Proceedings*, volume 678, pages 3–56. American Institute of Physics, 2003.

[37] H Edwin Boesch and F Barry McLean. Hole transport and trapping in field oxides. *IEEE Transactions on Nuclear Science*, 32(6):3940–3945, 1985.

[38] Marcel Zeiler. *Radiation-hard silicon photonics for future high energy physics experiments*. PhD thesis, Dublin City University, 2017.

[39] Wim De Boer, Johannes Bol, Alex Furgeri, Steffen Müller, Christian Sander, Eleni Berdermann, Michal Pomorski, and Mika Huhtinen. Radiation hardness of diamond and silicon sensors compared. *physica status solidi (a)*, 204(9):3004–3010, 2007.

[40] Simon M Sze, Yiming Li, and Kwok K Ng. *Physics of semiconductor devices*. John wiley & sons, 2021.

[41] Michael Moll, E Fretwurst, G Lindström, et al. Leakage current of hadron irradiated silicon detectors–material dependence. *Nuclear Instruments and Methods in Physics Research Section A: Accelerators, Spectrometers, Detectors and Associated Equipment*, 426(1):87–93, 1999.

[42] G. Aglieri Rinella et al. Optimization of a 65 nm CMOS imaging process for monolithic CMOS sensors for high energy physics. *PoS*, Pixel2022:083, 2023. doi:10.22323/1.420.0083.

[43] L Snoj, K Ambrožič, A Čufar, T Goričanec, A Jazbec, I Lengar, A Pungerčič, V Radulović, S Rupnik, Ž Štancar, et al. Radiation hardness studies and detector characterisation at the jsi triga reactor. In *EPJ Web of Conferences*, volume 225, page 04031. EDP Sciences, 2020.

[44] Stefaan Pommé, Heiko Stroh, and R Van Ammel. The 55fe half-life measured with a pressurised proportional counter. *Applied Radiation and Isotopes*, 148:27–34, 2019.

[45] Miljenko Šuljić et al. Study of monolithic active pixel sensors for the upgrade of the alice inner tracking system, 2018.